DOE/ET-0065/8

Damage Analysis and Fundamental Studies

Quarterly Progress Report
October - December 1979

February 1980

U.S. Department of Energy
Assistant Secretary for Energy Technology
Office of Fusion Energy

NOTICE

Printed in the United States of America
Available from
National Technical Information Service
U.S. Department of Commerce
5285 Port Royal Road
Springfield, Virginia 22161
Price: Printed Copy $9.00; Microfiche $2.25

DOE/ET-0065/8
UC-20,20c

Damage Analysis and Fundamental Studies

Quarterly Progress Report
October - December *1979*

February 1980

U.S. Department of Energy
Assistant Secretary for Energy Technology
Office of Fusion Energy
Washington, D.C. 20545

FOREWORD

This report is the eighth in a series of Quarterly Technical Progress Reports on *"Damage Analysis and Fundamental Studies"* (DAFS) which is one element of the Fusion Reactor Materials Program, conducted in support of the Magnetic Fusion Energy Program of the U. S. Department of Energy. Other elements of the Materials Program are:

- Alloy Development for Irradiation Performance (AOIP)
- Plasma-Materials Interaction (PMI)
- Special Purpose Materials (SPM).

The DAFS program element is a national effort composed of contributions from a number of National Laboratories and other government laboratories, universities, and industrial laboratories. It was organized by the Materials and Radiation Effects Branch, Office of Fusion Energy, DOE, and a Task Group on *Damage Analysis and Fundamental Studies* which operates under the auspices of that Branch. The purpose of this series of reports is to provide a working technical record of that effort for the use of the program participants, for the fusion energy program in general, and for the Department of Energy.

This report is organized along topical lines in parallel to a Program Plan of the same title (to be published) so that activities and accomplishments may be followed readily, relative to that Program Plan. Thus, the work of a given laboratory may appear throughout the report. Chapters 1 and 2 report topics which are generic to all of the OAFS Program: DAFS Task Group Activities and Irradiation Test Facilities, respectively. Chapters 3, 4, and 5 report the work that is specific to each of the subtasks around which the program is structured: A. Environmental Characterization, B. Damage Production, and C. Damage Microstructure Evolution and Mechanical Behavior. The Table of Contents is annotated For the convenience of the reader.

This report has been compiled and edited under the guidance of the Chairman of the Task Group on *Damage Analysis and Fundamental Studies*, D. G. Ooran, Hanford Engineering Development Laboratory. His efforts and those of the supporting staff of HEOL and the many persons who made technical contributions are gratefully acknowledged. M. M. Cohen, Materials and Radiation Effects Branch, is the Department of Energy counterpart to the Task Group Chairman and has responsibility for the DAFS Program within DOE.

Klaus M. Zwilsky, Chief
Materials and Radiation
Effects Branch
Office of Fusion Energy

CONTENTS

CONTENTS (Cont'd)

CONTENTS (Cont'd)

CONTENTS (Cont'd)

CONTENTS (Cont'd)

FIGURES

FIGURES (Cont'd)

Page

CHAPTER 5

FIGURES (Cont'd)

FIGURES (Cont'd)

TABLES

TABLES (Cont'd)

TABLES (Cont'd)

CHAPTER 1

DAFS TASK GROUP ACTIVITIES

DAFS TASK GROUP ACTIVITIES

I. DAFS Task Group - (D. G. Doran, Chairman)

The DAFS Task Group structure was modified in December to aid in implementing the DAFS Program Plan.[1] The Task Group itself is a small body comprised *of* Subtask Groupchairmen and consultants which serves as a steering committee and advisor to the Office of Fusion Energy. Its current membership is

Chairman:	D. G. Doran
DOE Counterpart:	M. M. Cohen
Chairman, Dosimetry and Damage Parameters:	L. R. Greenwood
Chairman, Fundamental Mechanical Behavior:	R. H. Jones
Chairman, Correlation Methodology:	G. R. Odette
Consultant:	W. G. Wolfer

You will note that, in order to achieve increased emphasis in the area of mechanical behavior, a separate subtask group was established. Concurrently, the subtask groups on Environmental Characterization and Damage Production were combined.

The subtask groups are, as before, the working groups responsible for effecting program coordination. All DAFS programs will be represented on the appropriate subtask groups. Liberal use will be made *of* outside consultants.

(1) The Fusion Reactor Materials Program Plan-Section II - Damage Analysis and Fundamental Studies, DOE/ET-0032/2, July 1978.

II. Subtask Group A - Environmental Characterization

(L. R. Greenwood, Chairman)

The status of current OAFS dosimetry programs for fusion materials irradiations was presented recently at meetings in Ispra, Italy[1] and Knoxville, Tennessee.[2] Emphasis was placed on nuclear data needs, especially for high energy (>20 MeV) neutron sources, such as FMIT. There was also considerable interest in improving the $^{93}Nb(n,n')^{93m}Nb(13.6\ y)$ reaction cross section, especially for long reactor irradiations, to improve flux measurements in the 1-500 keV energy region.

A new international effort to compare spectral unfolding data and codes was proposed at Ispra. Particular emphasis would be placed on uncertainties in derived integral parameters (such as DPA). The project, called REAL-80, will be directed by W. L. Zijp (ECN, Petten) and C. Ertek (IAEA, Vienna) and should be completed in time for the Fourth ASTM-EURATOM Symposium in October 1981. Data from ANL spectral measurements in ORR have already been transmitted for use as a possible test case. Other U.S. participants identified at Ispra are HEDL, ORNL, and GE (Vallecitos)

(1) L. R. Greenwood, "The Status of Current, Routine Dosimetry at Existing Irradiation Facilities: Flux-Spectrum Mapping at DRR, RTNS-II, and U. C. Davis," Proceedings of the Third ASTM-EURATOM Symposium, Ispra, Italy, October 1979. (To be published)

(2) L. R. Greenwood, "The Status of Neutron Dosimetry and Damage Analysis for the Fusion Materials Program," Proceedings of the International Conference on Nuclear Cross Sections for Technology, Knoxville, Tennessee, October 1979. (To be published)

CHAPTER 2

IRRADIATION TEST FACILITIES

I. PROGRAM

Title: RTNS-II Operations (WZJ-16)
Principal Investigator: C. M. Logan
Affiliation: Lawrence Livermore Laboratory

II. OBJECTIVE

The objectives of this work are operation of OFE's RTNS-II (al4-MeV neutron source facility), machine development, and support of the experimental program that utilizes this facility. Experimenter services include dosimetry, handling, scheduling, coordination, and reporting.

III. RELEVANT DAFS PROGRAM TASK / SUBTASK

TASK II.A.2,3,4.
TASK II.B.3,4,
TASK II.C.1,2,6,11,18.

IV. SUMMARY

Machine reliability is good and improving. One lot of targets was found to delaminate in service, causing a temporary target shortage.

V. ACCOMPLISHMENTS AND STATUS

A. Irradiations. - N. E. Ragaini, M. W. Guinan and C. M. Logan. (LLL)

Irradiation of some MACOR ceramic samples has been completed for Frank Clinard of LASL. Additional irradiations of MACOR and glass-bonded mica are planned. The HEDL3 capsule was completed. This

capsule included Ni-Al and Ni-Si TEM disks for a joint ANL/LLL investigation of precipitate dissolution. Dosimetry for this capsule has not been completed.

B. RTNS-II Status - C. M. Logan and D. W. Heikkinen (LLL)

Machine reliability is good and getting better. During October and November we were on and making neutrons 70% of the available hours. The installation of copper beam pipe seems to have eliminated vacuum problems from thermally-induced cracking. An optical micrometer is in and working which gives beam spot size information.

Late in November a target delaminated while in use on the machine. Considerable damage was sustained by the sealing assembly. All targets on hand proved defective. The cause is now known but a target shortage exists. No neutrons were produced in December.

VI. REFERENCES

None

VII. FUTURE WORK

During the next quarter irradiations are scheduled for Jones (PNL), Clinard (LASL), Guinan (LLL), Barmore (LLL), VanKonynenberg (LLL) and Panayotou (HEDL4).

VIII. PUBLICATIONS

None

I. PROGRAM

Title: Nuclear Data for Damage Studies and FMIT (WH025/EDK)
Principal Investigator: R.E.Schenter
Affiliation: Hanford Engineering Development Laboratory (HEDL)

11. OBJECTIVE:

The objective of this work is to supply nuclear data needed for damage studies and in the design and operation of the Fusion Material Irradiation Testing (FMIT) facility.

III. RELEVANT DAFS PROGRAM PLAN TASK/SUBTASK

All tasks that are relevant to FMIT use, with emphasis upon:

SUBTASK	II.A.2.3	Flux-spectra definition in FMIT
TASK	II.A.4	Gas Generation Rates
SUBTASK	II.A.5.1	Helium Accumulation Monitor Development
SUBTASK	II.B.1.2	Acquisition of Nuclear Data

IV. SUMMARY

Measurements and analysis of deuteron induced activation of FMIT accelerator, beam transport, and target materials were continued in order to provide data to optimize design from the standpoint of maintenance.

Planning continues for measurements of the transmission of FMIT neutrons through thick iron in order to verify calculations of radiation heating on the FMIT test cell walls.

The NJOY system for processing nuclear cross sections has been transferred to the MFECC.

The study of the microscopic Li(d,n) yields is continuing with the inclusion of backward angle data and the use of spectral correction factors.

An FMIT Activation Library is being created to cover neutron activation to 40 MeV.

V. ACCOMPLISHMENTS AND STATUS

A. Deuteron and Neutron Induced Activation of FMIT Materials -- D. L. Johnson (HEDL), C. M. Castaneda and M. L. Johnson (U.C. Davis).

A principal goal of the FMIT project is to be able to perform hands-on maintenance as much as possible. Activation of various materials will provide limitations to the ability to do hands-on maintenance, particularly in the vicinity of the test cells where the beam is deposited. In the vicinity of the accelerator and beam transport system the amount of activation will be directly related to the amount and location of losses of the deuteron beam rather than the amount transmitted. Although such beam losses are expected to be very small compared to the total beam current, large activations can result from nuclear reactions induced directly by the deuterons and also by the secondary neutrons that are prolifically produced when deuterons are incident upon any material.

A program to provide data for evaluation of activation of FMIT materials is underway. As part of this program, measurements of deuteron induced activation were performed by observation of decay gamma rays with a high resolution Ge(Li) detector after bombardment with 35 MeV deuterons at the University of California at Davis. The objective was to measure the production rate of all significant gamma emitting isotopes in important materials with half lives longer than about an hour. The production rates coupled with known decay properties will allow calculations of radiation dose from irradiated material for any combination of incident current, irradiation time, and decay time.

Initial measurements were performed in September 1979 on targets of

lithium, the FMIT target material, on copper and gold, for the accelerator system, and on carbon, aluminum, tantalum, and lead for possible use in the high energy beam transport system. For some targets, there are many significant radio-isotopes produced, each of which may have more than one gamma ray associated with its decay.

Analysis of the experimental gamma ray spectral measurements has been initiated. To handle the large number of gamma rays observed for some targets, the gamma ray analysis program HYPERMET has been implemented. This program provides for rapid location and fitting of gamma ray peaks and background to observed pulse height distributions.

Preliminary analysis of measurements of the production of ^{7}Be by deuterons incident on natural lithium has been completed. As is well known, ^{7}Be is one of the most important radio-isotopes to be produced in the FMIT lithium system because of its large production rate, its 53.3 day half-life, its emission of gamma rays of about 0.48 MeV, and its tendency to plate out on the inside walls of the piping. This isotope is produced mainly via the ^{7}Li(d,2n)^{7}Be reaction.

The production rate had not been established at 35 MeV although there were some data at lower energies. Figure 1 shows the previous data as taken from Dmitriev et al., (Ref. 1). The units shown correspond to (μCi/μA-hr) which can be converted to (atoms/s - A) by multiplying by $6.826(10^{13})$. Extrapolation to 35 MeV is very uncertain using these older data, especially when one considers the large discrepancies between different experimenters.

Preliminary results of the current measurement indicate a production rate of $1.68(10^{16})$ (atoms/s - A) or 246 (μCi/μA-hr) for 35 MeV deuterons. An uncertainty of about 20% (1σ) is estimated. With a beam current of 0.1A, the saturated activity for this rate would correspond to 4.54 (10^{4}) curies. This value is a factor of about 4 less than a previous measure-

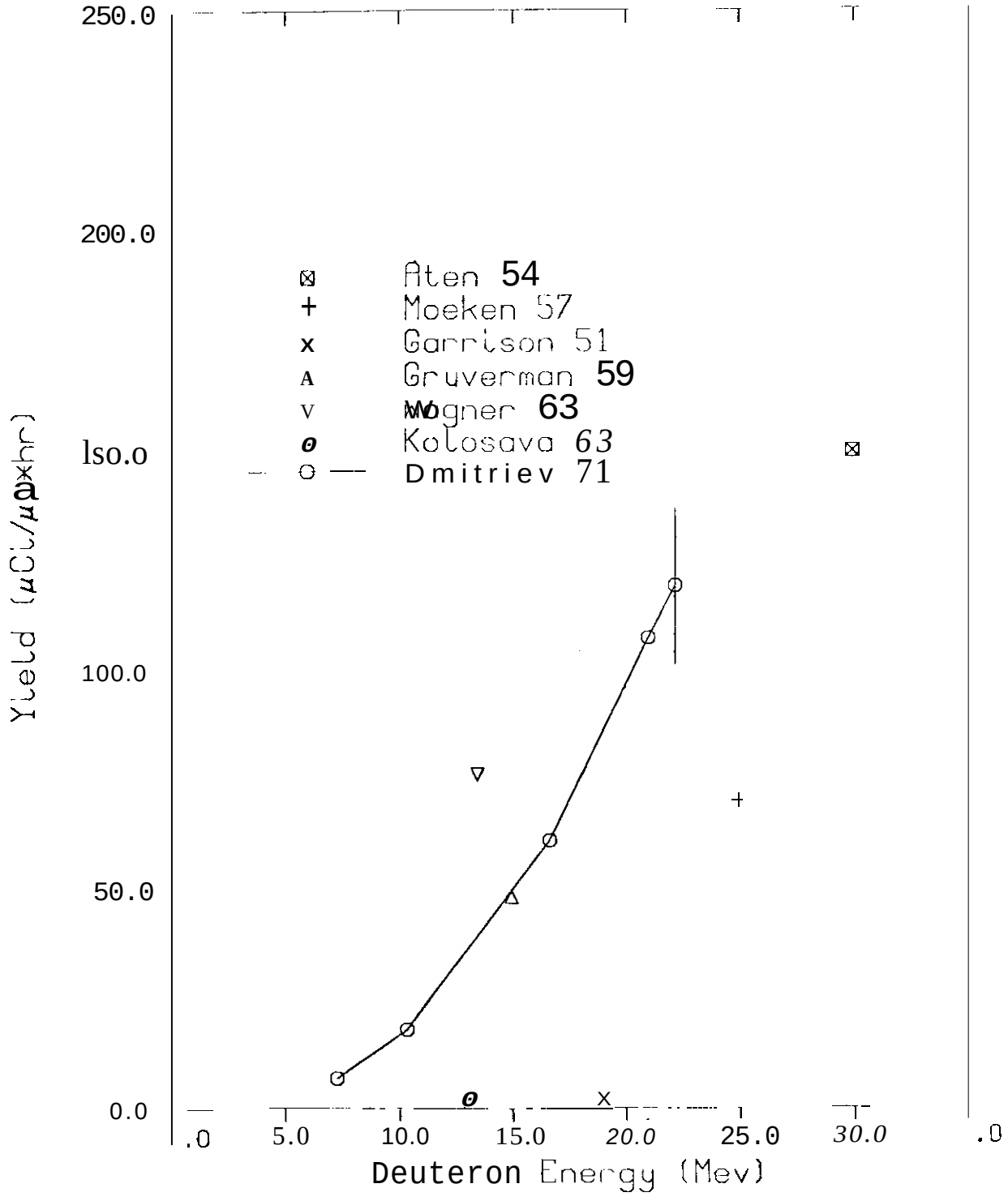

FIGURE 1. Production Rate of ^{7}Be From Deuterons on Thick Natural Lithium. (Older data)

ment at U.C.Davis; however, it is expected to be significantly more accurate because of improvements in the beam current integration system and in knowledge of the detector efficiency.

Further evidence of the reliability of the data is provided by measurement of the energy dependence of the production rate (shown in Figure 2) which overlaps the energy range of the previous data shown in Figure 1. These new data were obtained by activation of a stack of lithium metal foils, each about 1.5 mm thick, whose total thickness was more than enough to stop deuterons of 35 MeV (range ~15 mm). The energy dependence of the thick target production rate was obtained by counting partial stacks from which successive foils were removed. The energy of deuterons can be calculated very accurately as a function of penetration in the lithium. These results agree very well with the previous data of Dmitriev et al., (Ref. 1), except at low energies where there are known energy discrepancies in the new data.

Preliminary analysis has also begun on measurements of activation of copper by deuterons. Table 1 illustrates the reactions that are expected to be most significant for deuterons up to 35 MeV on copper. Some reactions are not included because of estimated weak production, a very short half life or because they have very low energy gamma rays that are easily shielded. All of the radioactive products have been tentatively observed except for ^{66}Cu and ^{62}Cu which, because of their short half lives, decayed away prior to measurements of decay spectra. The nuclides ^{58}Co and ^{59}Fe were not expected to be observed since previous measurements that we are aware of in this energy range have not shown these nuclides. For maintenance purposes, the long lived products ^{65}Zn, ^{58}Co, ^{60}Co, and ^{59}Fe are most important since they build up and do not decay away in a reasonable time. The shorter lived nuclides are of less importance because one can wait until they decay away.

A plot of the thick target production rate of ^{64}Cu, ^{65}Zn, and ^{62}Zn as a function of incident deuteron energy is shown in Figure 3. These iso-

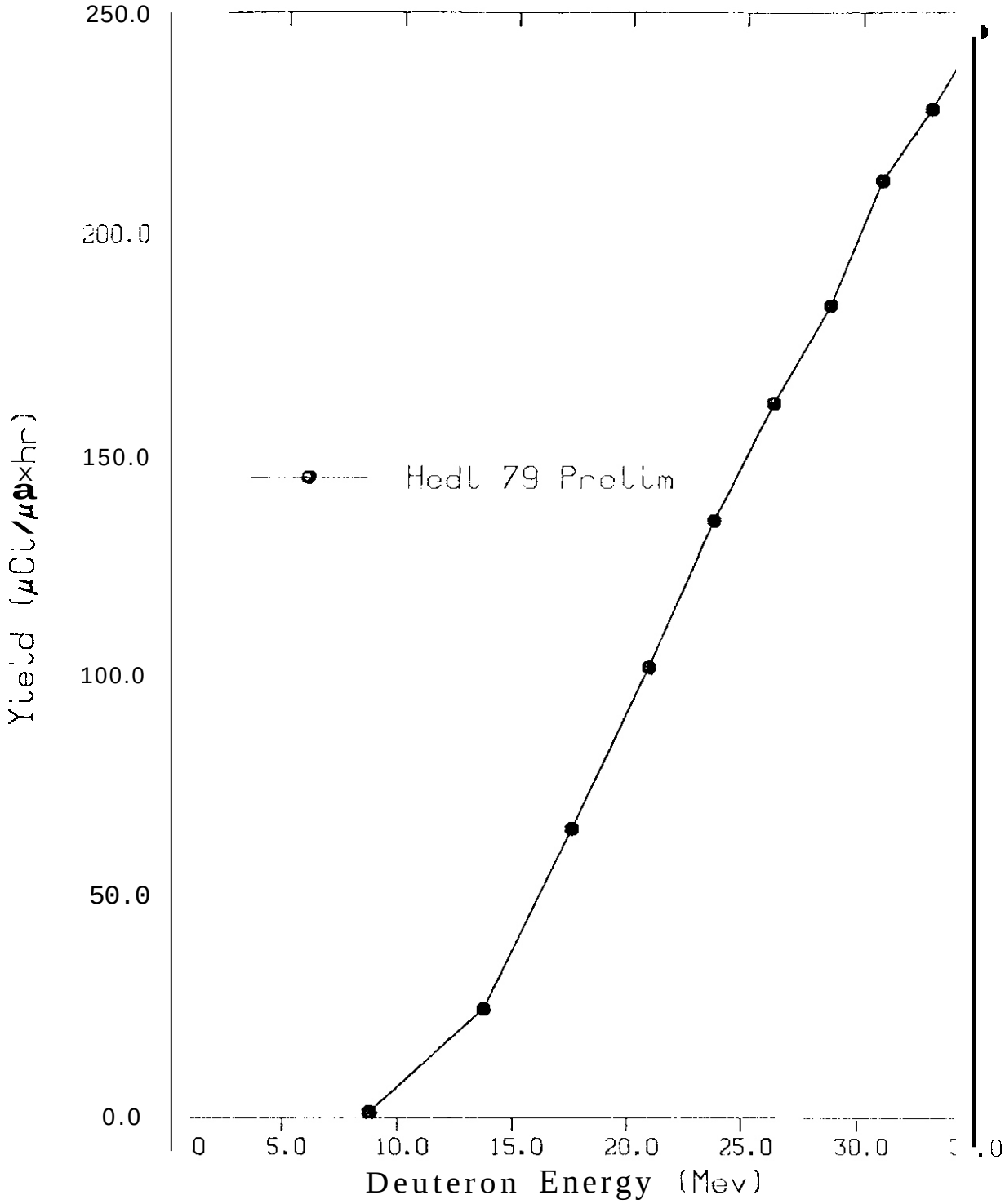

FIGURE 2. Production Rate of ^{7}Be From Deuterons on Thick Natural Lithium. (New Data)

TABLE 1

MOST SIGNIFICANT REACTIONS FOR ACTIVATION OF COPPER BY DEUTERONS UP TO 35 MeV

Reaction	Product Half Life
$^{65}Cu(d,2n)^{65}Zn$	243.8 days
$^{65}Cu(d,5n)63Zn$	38.1 minutes
$^{63}Cu(d,2n)^{63}Zn$	38.1 minutes
$^{63}Cu(d,3n)62Zn$	9.3 hours
$^{65}Cu(d,p)66Cu$	5.1 minutes
$^{65}Cu(d,T)(d,dn)(d,p2n)^{64}Cu$	12.7 hours
$^{63}Cu(d,p)^{64}Cu$	12.7 hours
$^{63}Cu(d,T)(d,dn)(d,p2n)^{62}Cu$	9.7 minutes
$^{63}Cu(d,Tn)(d,d2n)(d,p3n)^{61}Cu$	3.3 hours
$^{65}Cu(d,2p)65Ni.$	2.5 hours
$^{65}Cu(d,d\alpha)^{61}Co$	1.65 hours
$^{63}Cu(d,d2p)(d,^{3}Hep)^{61}Co$	1.65 hours
$^{65}Cu(d,\alpha T)(d,d\alpha n)^{60}Co$	5.3 years
$^{63}Cu(d,\alpha p)(d,d^{3}He)^{60}Co$	5.3 years
$^{63}Cu(d,\alpha T)(d,d\alpha n)^{58}Co$	73.8 days
$^{65}Cu(d,2\alpha)^{59}Fe$	44.6 days
$^{63}Cu(d,\alpha 2p)^{59}Fe$	44.6 days

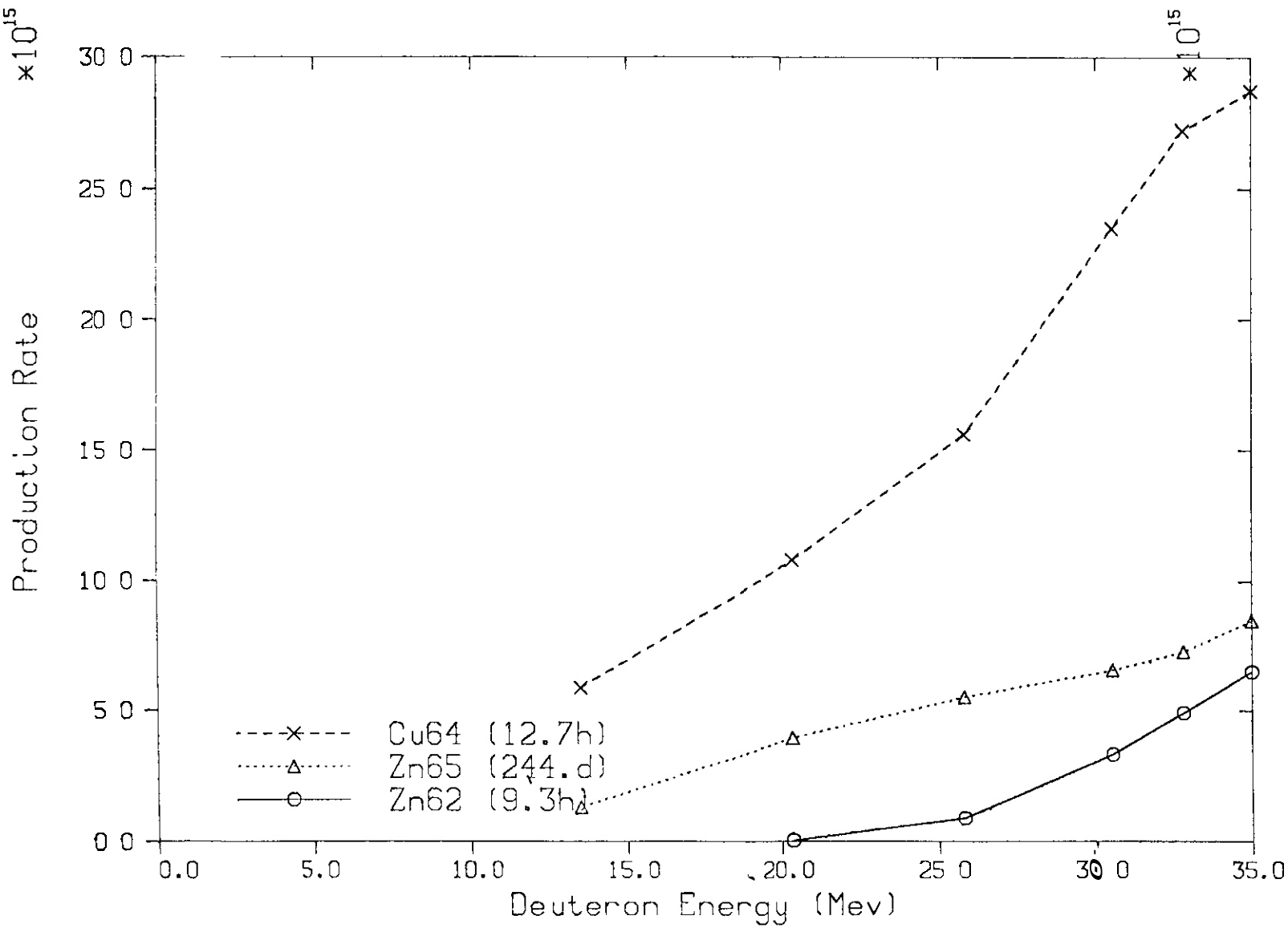

FIGURE 3 Thick Target Production Rate (Atoms/Sec-A).

topes are among the most abundantly produced. The ^{64}Cu production is largest because it can be produced both via $^{65}Cu(d,dn)$ and $^{63}Cu(d,p)$ reactions.

A second set of deuteron induced activation measurements was completed in December 1979 for targets of Al, Fe, Ni, and Mo. Cyclotron problems prevented measurements planned for targets of Na, K, Ca, Cr, and Mn; however, future experiments are planned.

B. Neutron Transport Measurements -- D. L. Johnson (HEDL)

Planning continues for measurements of the transmission of FMIT neutrons through thick iron. The objective is to confirm neutron transport calculations used for predictions of radiation heating in the FMIT test cell walls. Neutrons are to be produced by 35 MeV deuterons incident on a 2 cm. thick lithium target. The conceptual design of this experiment has the target placed at the center of a large mass of solid iron with about 12" of iron for neutrons to penetrate. Neutron spectra will be observed with detectors placed outside the sphere.

An initial concept was for the iron to be in the form of a solid sphere. A bid for construction of a 30" diameter iron sphere was very high and was not accepted. Current plans are to use a nearly cubical ($\sim$ 2' on a side) iron block provided by the Crocker Nuclear Laboratory, University of California at Davis.

C. Neutron Cross Sections for Transport Calculations -- F. M. Mann and R. E. Schenter (HEOL).

When calculating flux in a pure medium using multi-group techniques, great care must be exercised to use the appropriate self-shielded group cross sections. To aid in obtaining the required data, HEOL has implemented the LASL cross section processing system NJOY[2] on the local UNIVAC 1100/44, as described previously. The system is capable of providing

data for discrete ordinate transport calculations, Monte Carlo calculations, Kerma factors, damage parameters, and diffusion theory calculations.

LASL has transferred the NJOY system to the CDC 7600 computer at MFECC. HEDL will convert the system to the CRAY-1.

D. Cross Section Prediction -- F. M. Mann (HEDL) and C. Kalbach (Triangle Universities Nuclear Laboratory).

Two papers on the systematics of experimental angular distributions for particles emitted in the pre-equilibrium phase of nuclear reactions have been submitted to Nuclear Physics for publication.

E. Microscopic Neutron Yield Model -- F. M. Mann and F. Schmittroth (HEDL).

The microscopic neutron yield model has been improved by the inclusion of backward angle experimental data into the least square analysis. In addition, small correction factors have been derived to ensure that the calculated neutron spectra have the same shape as those measured at Ed = 35 MeV by Johnson et al.

F. FMIT Activation Library -- F. M. Mann (HEDL).

A Neutron Activation Library for FMIT energies has been started. The initial library (see Table 2) is based on THRESH model calculations to 40 MeV. Where possible, ENDF/B-V data to 20 MeV has replaced the THRESH results. Activation libraries (to En=20 MeV) have been received from LASL and LLL.

VI. REFERENCES

1. P. P. Dmitriev et al., Soviet Atomic Energy 31 (1971) 876

TABLE 2

GROUP LIBRARY (96 NUCLIDES)

^{6}Li	^{36}Ar	^{55}Mn	^{92}Mo	^{204}Pb
^{7}Li	^{38}Ar	^{54}Fe	^{94}Mo	^{206}Pb
^{12}C	^{40}Ar	^{56}Fe	^{95}Mo	^{207}Pb
^{13}C	^{39}K	^{57}Fe	^{96}Mo	^{208}Pb
^{14}N	^{41}K	^{58}Fe	^{97}Mo	
^{15}N	^{40}Ca	^{59}Co	^{98}Mo	
^{16}O	^{42}Ca	^{58}Ni	^{100}Mo	
	^{43}Ca	^{60}Ni	^{114}Sn	
^{18}O	^{44}Ca	^{61}Ni	^{115}Sn	
^{19}F	^{46}Ca	^{62}Ni	^{116}Sn	
^{20}Ne	^{48}Ca	^{64}Ni	^{117}Sn	
^{21}Ne	^{45}Sc	^{63}Cu	^{118}Sn	
^{22}Ne	^{46}Ti	^{65}Cu	^{119}Sn	
^{23}Na	^{47}Ti	^{64}Zn	^{120}Sn	
^{24}Mg	^{48}Ti	^{66}Zn	^{122}Sn	
^{25}Mg	^{49}Ti	^{67}Zn	^{124}Sn	
^{26}Mg	^{50}Ti	^{68}Zn	^{181}Ta	
^{27}Al	^{50}V	^{90}Zr	^{180}W	
^{28}Si	^{51}V	^{91}Zr	^{182}W	
^{29}Si	^{50}Cr	^{92}Zr	^{183}W	
^{30}Si	^{52}Cr	^{94}Zr	^{184}W	
^{31}P	^{53}Cr	^{96}Zr	^{186}W	
^{32}S	^{54}Cr	^{93}Nb	^{197}Au	

2. R. E. MacFarlane et al., "The NJOY Nuclear Data Processing System User's Manual". LA-7584-M LASL, Dec. 1978.

VII. FUTURE WORK

More measurements of deuteron induced activation of FMIT materials will be performed. Results will be compared to previous calculations.

More evaluations of neutron cross sections for transport calculations will be done as needed by the FMIT architect-engineer and for predictions in the FMIT test cell.

Measurements of the transmission of FMIT neutrons through thick iron will be completed.

The computer code HAUSER*5 will be modified to include the study of angular distributions.

VIII. PUBLICATIONS

1. C. Kalbach and F. M. Mann, Phenomenology of Emitted Particle Angular Distributions for Preequilibrium Reactions: I. Systematics. submitted to Nuclear Physics.

2. C. Kalbach and F. M. Mann, Phenomenology of Emitted Particle Angular Distributions for Preequilibrium Reactions: II. Parameterization. submitted to Nuclear Physics.

CHAPTER 3

SUBTASK A: ENVIRONMENTAL CHARACTERIZATION

I. PROGRAM

Title: Dosimetry and Damage Analysis
Principal Investigator: L. R. Greenwood
Affiliation: Argonne National Laboratory

II OBJECTIVE

To establish the best practicable dosimetry for mixed-spectrum reactors and to provide dosimetry and damage analysis for MFE experimenters.

III. RELEVANT DAFS PROGRAM TASK/SUBTASK

SUBTASK II.A.1.1 Flux-spectral definition in a tailored fission reactor.

IV. SUMMARY

Preliminary flux gradients are presented for the MFE-1 experiment in the Oak Ridge Research Reactor (ORR). The results appear to agree with new neutronics calculations. Dosimetry packages have been assembled for the MFE-4 experiment.

V. ACCOMPLISHMENTS AND STATUS

A. Flux Gradients and He Calculations for ORR-MFE-1

L. R. Greenwood and R. R. Heinrich (ANL)

Preliminary flux gradients have been calculated for the MFE-1 experiment in core position C7 from February - June 1978. Figures 1 and 2 show the flux as a function of vertical height above the midplane. The thermal flux was deduced from the ^{58}Fe and $^{59}Co(n,\gamma)$ reactions, the flux above

0.92 MeV from the $^{54}Fe(n,p)$ reaction, and above 3.3 MeV from the $^{46}Ti(n,p)$ reaction. The values are preliminary since exact spectral-averaped cross sections are not yet available. However, the thermal fluxes and the flux above 3.3 MeV are not expected to change significantly.

New neutronics calculations have been performed by T. Gabriel (ORNL) using the average fuel loading during the MFE-1 experiment. The results appear to agree quite well with our measurements, confirming the steep fast-flux gradient from the South side to the North side of the capsule. When the neutronics calculations are completed, we will revise our flux values using the STAYSL adjustment code.

Preliminary comparisons have also been made between the helium measurements by D. Kneff and H. Farrar IV (RI) and helium calculated using our flux values and ENDF/B-IV helium production cross sections. Table I compares these values for Ni, Fe, and Cu at two positions in the Northeast corner of the MFE-1 capsule. As can be seen, the Ni calculations are quite close to the measured values. The Fe and Cu calculations are about 25% lower than the measurements. It should be noted that both the helium measurements and the flux values are still preliminary; however, the changes are not expected to be very significant. The Ni calculations included the $^{58}Ni(n,\gamma)^{59}Ni(n,\alpha)^{56}Fe$ reaction mechanism using the relationship:(1)

$$\frac{He}{m} = 0.12608 + 0.00664\, e^{-92\phi t} - 0.13272\, e^{-4.6\phi t}$$

where ϕt is the 2200 m/s fluence. This equation is somewhat uncertain due to uncertainties in the assumed nuclea: cross section values.

Table I. He Measurements and Calculations for ORR-MFE 1
(Northeast corner of C7)

Location, cm (above midplane)		He (appm) Ni	Fe	Cu
+ 21.7	Expt.*	10	0.090	-
	Calc.	9.4	0.071	0.070
+ 1.9	Expt.*	48	-	0.18
	Calc.	43.0	0.146	0.144

* D. Kneff and H. Farrar IV, Rockwell International, DOE/ET-0065/6, July 1979.

B. Dosimetry Plan for ORR-MFE-4

L. R. Greenwood (ANL)

Dosimetry capsules have been prepared for the first MFE-4 experiment in ORR scheduled for January 1980. Eight stainless steel tubes measuring 7 cm in length and 0.159 cm in diameter have been filled with nine radiometric and helium accumulation monitors. It is planned that one tube will be placed in each of the four corners of the two levels of the irradiation capsule.

A new technique is being used on this irradiation in that most of the monitor wires will be used for both radiometric and helium measurements. The wires will be gamma counted at ANL and then helium analyzed at RI. This simplifies the capsule construction and saves valuable space. The monitors include Fe, Ni, Nb, Cu, Ti, Co, 80.2% Mn-Cu, and Ag. A few platinum encapsulated helium monitors have also been included to check the wire results.

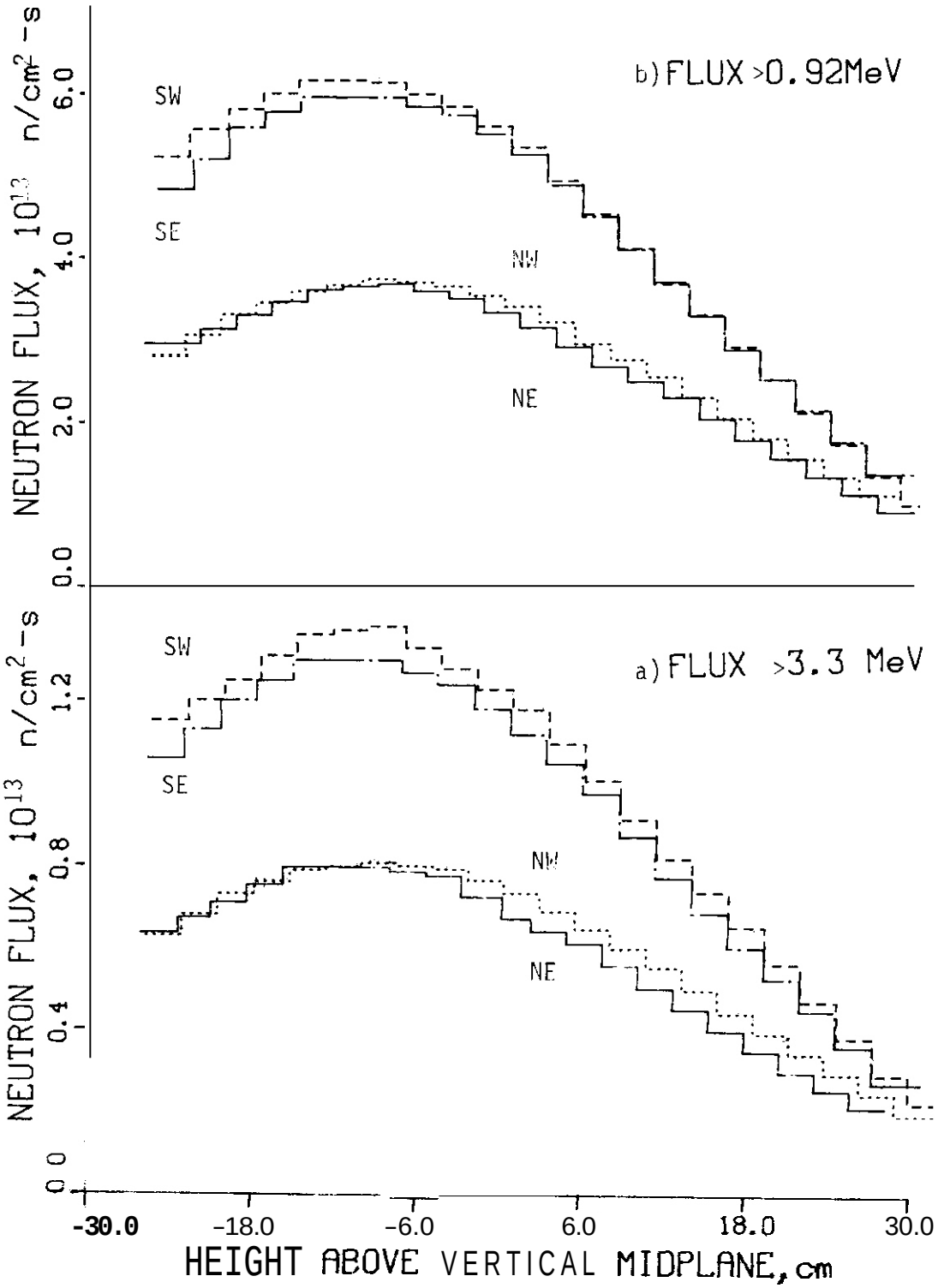

Figure 1. Vertical flux gradients for ORR-MFE-1 with neutron energy limits of a) 3.3 MeV from $^{46}Ti(n,p)$ and b) 0.92 MeV from $^{54}Fe(n,p)$ reactions. Note the steep gradient from South to North.

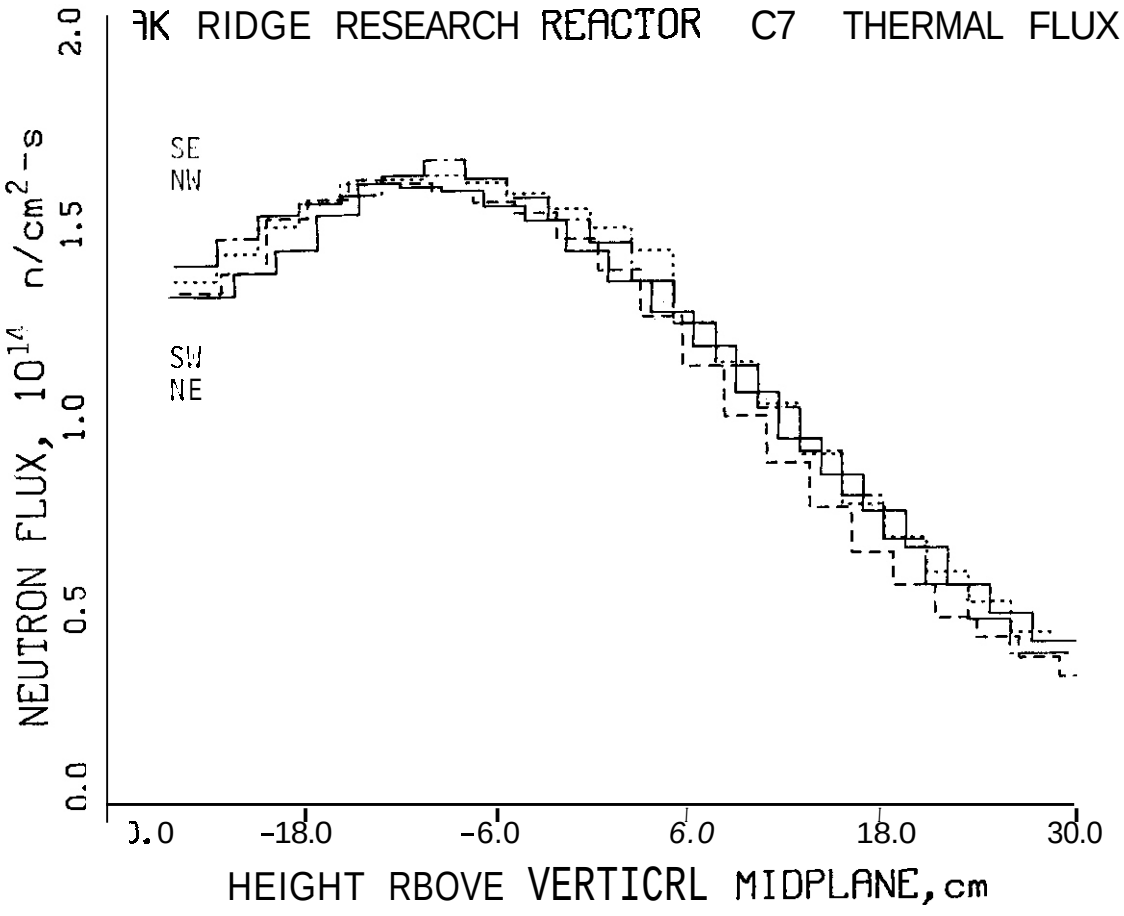

Figure 2. Thermal (<.5 eV) flux gradients for ORR-MFE-1. Note that the flux is nearly isotropic.

VI. REFERENCE

1. T. A. Gabriel, B. L. Bishop and F. W. Wiffen, "Calculated Irradiation Response of Materials Using Fission Reactor (HFIR, ORR and EBR-II) Neutron Spectra," ORNL/TM-6361, August 1979.

VII. FUTURE WORK

The FIFE-1 dosimetry results will be completed as the new neutronics calculations and helium measurements are finalized. Fluence and damage parameter maps will be generated for the irradiation assembly.

The first MFE-4 experiment is scheduled to commence in January. An identical experiment is also planned in March.

The MFE-2 irradiation is expected to be completed in March.

VIII. PUBLICATIONS

None.

I. PROGRAM

Title: Helium Generation in Fusion Reactor Materials
Principal Investigators: D. W. Kneff, Harry Farrar IV
Affiliation: Rockwell International, Energy Systems Group

II. OBJECTIVE

The objective of this part of the fusion program at Rockwell International is to develop and apply helium accumulation neutron dosimetry to the measurement of neutron fluences and energy spectra in mixed-spectrum fission reactors utilized for fusion materials testing.

III. RELEVANT OAFS PROGRAM PLAN TASK/SUBTASK

TASK II.A.1	Fission Reactor Dosimetry
SUBTASK II.A.1.1	Flux-Spectral Definition in a Tailored Fission Reactor
SUBTASK II.A.1.2	Enhance Technique

IV. SUMMARY

The helium accumulation neutron dosimetry analysis has been completed for the Al, Ti, Fe, Ni, and Cu pure-element dosimeters irradiated in the **MFE-1** experiment in the Oak Ridge Research Reactor (ORR). The results, which represent five different vertical positions relative to the core centerline, provide both a matrix of helium generation concentrations for dosimetry unfolding, and direct helium production information relevant to candidate fusion reactor materials. A set of bare and platinum-encapsulated pure-element helium accumulation neutron dosimetry materials was prepared and shipped to Argonne National Laboratory (ANL) for incorporation in the ORR MFE-4 irradiation scheduled to commence in January 1980.

V. ACCOMPLISHMENTS AND STATUS

A. Helium Accumulation Fluence Dosimetry for the MFE-1 Irradiation at the Oak Ridge Research Reactor -- D. W. Kneff, Harry Farrar IV, and M. M. Nakata (Rockwell International, Energy Systems Group)

The MFE-1 irradiation in the Oak Ridge Research Reactor (ORR) included five sets of helium accumulation neutron dosimetry materials. Each set consisted of an array of bare pure-element wires and vanadium-encapsulated samples containing pure elements and binary compounds. These materials were loaded in dosimetry monitor tube No. 9, which was in turn positioned along the northeast cooling tubes in the north section of ORR core Position C7. The dosimetry sets were placed in five different vertical positions relative to the horizontal core centerline. The irradiation lasted 1.164×10^7 s (135 days), with an average power level of 22.524 MW. A detailed description of the helium accumulation dosimetry materials and some initial analysis results were given in previous reports.[1,2]

Analysis of a matrix of the five bare wire helium accumulation dosimetry materials (Al, Ti, Fe, Ni, and Cu) incorporated in MFE-1 has now been completed for the five ORR locations. A summary of the helium concentration results is given in Table 1. Each reported concentration value is the average of at least two independent helium analyses of adjacent segments of each dosimetry wire. The wires were etched to an average depth of about 0.05 mm (2 mils) before analysis, to eliminate possible helium surface effects. Such effects could be produced, for example, by alpha recoil or by the absorption of external helium. Evidence from other helium measurements programs indicates that the elevated temperatures encountered during the irradiation should not have resulted in any significant loss of helium by diffusion. The possible exceptions to this were three aluminum wires which were not analyzed because their surfaces showed evidence of bubbling and softening, making them appear

Core Location (cm)*	^{4}He Concentration (appm)†				
	Al	Ti	Fe	Ni	cu
+21.7	0.154	0.068	0.094	10.2	0.081
+10.0	0.258	0.107	0.147	30.1	0.141
+1.9		0.128	0.177	48.5	0.181
-9.8		0.148	0.200	63.5	0.208
-18.3		0.138	0.202	53.5	0.190

(10^{-6}

less reliable for gas analysis. A total of 53 helium analyses were performed. Scatter in the data was less than 2% in all cases, and generally about 1%.

Examination of the data in Table 1 shows significant helium concentration gradients as a function of core location. The gradients for Ti, Fe, and Cu are nearly identical, and agree with the radiometrically determined vertical flux gradients for the ORR MFE-1 and MFE Spectral Characterization irradiations.[3] The similarity of the relative helium concentration gradients for the five dosimetry materials can be seen more clearly in the top half of Table 2, where the helium generation rates are presented as ratios with respect to the copper results. The ratios for Ti, Fe, and Cu are generally constant as a function of location. The gradient for nickel, as explained later, is steeper.

The measured concentration gradients also imply that any helium contributions by ^{10}B(n,α) reactions with boron impurities in these pure elements are insignificant. Such impurities would have produced smaller helium concentration gradients, because nearly complete burnup of ^{10}B

Neutron Spectrum	Helium Generation Rates Relative to Copper				
	Al	Ti	Fe	Ni	Cu
ORR MFE-1, +21.7 cm	1.90	0.84	1.16	126	1
+10.0 cm	1.83	0.76	1.04	214	1
+1.9 cm		0.71	0.98	268	1
-9.8 cm		0.71	0.96	305	1
-18.3 cm		0.73	1.06	282	1
ORR MFE-1 (average)	1.87	0.75	1.04	126-305	1
EBR-II*	1.87	0.73	0.99	13.2	1
Be(d,n), 30-MeV deuterons†	2.9	0.8	1.0	2.4	1
T(d,n), RTNS-I**	2.80	0.75	0.94	1.92	1

*E. P. Lippincott, et al., Reference 4

†D. W. Kneff, et al., Reference 5

**H. Farrar IV and D. W. Kneff, Reference 6

would have occurred. In contrast, a ~4 weight parts per million boron impurity in the vanadium used to make helium accumulation fluence monitor (HAFM) capsules was previously shown to produce a major helium contribution to the total helium generated in HAFMs irradiated in ORR.(2)

Table 2 also demonstrates some important observations on the use of the pure elements as helium accumulation neutron dosimeters. The bottom half of the table compares the ratios of the measured helium concentrations in ORR with results measured in this laboratory for other, widely differing neutron spectra: EBR-II core center,(4) Be(d,n) neutrons for 30-MeV deuterons,(5) and 14.8-MeV T(d,n) neutrons from RTNS-I.(6) The first observation is that Ti, Fe, and Cu have very similar energy responses for all of these spectra. This is expected, because their

effective reaction thresholds for helium production are several MeV, and the monitors are thus responsive only to the high-energy component of the ORR neutron spectrum. Just one of these monitor materials is thus really required to obtain this dosimetry information. Aluminum is similar, but appears to show a slightly different trend in energy response.

The second observation is that nickel produced a wider range of helium concentrations within ORR, as well as between neutron environments. The reason for this very different response is that helium generation at high neutron fluences in a thermal neutron spectrum is dominated by the two-stage thermal neutron reaction $^{58}Ni(n,\gamma)^{59}Ni(n,\alpha)$. The helium production rate increases dramatically as the ^{59}Ni builds up, resulting in the generation of relatively large amounts of helium. This two-stage reaction makes nickel a particularly responsive and accurate fluence monitor in thermal and mixed-spectrum neutron reactors at these high fluence levels. A paper reporting new, more accurate cross sections for the two-stage nickel reaction rate is now in final preparation.

The helium concentration results in Table 1 thus provide two distinct dosimetry monitor responses which should now be combined with the ANL radiometric reaction rate data to unfold the MFE-1 neutron spectra in more detail. They also provide direct helium generation data from ORR for five pure elements that appear as components of candidate fusion reactor materials.

B. Helium Accumulation Fluence Dosimetry for the MFE-4 Irradiation at ORR -- D. W. Kneff and Harry Farrar IV (Rockwell International, Energy Systems Group)

A new joint ORR dosimetry experiment with ANL was initiated during the report period. A set of helium accumulation dosimetry materials was assembled and shipped to ANL for incorporation in the MFE-4 irradiation

experiment scheduled for ORR in January 1980. The contents of this dosimetry set are summarized in Table 3. Platinum capsules were included for a direct verification of helium retention in the bare dosimetry wires

TABLE 3

HELIUM ACCUMULATION DOSIMETRY MATERIALS SUPPLIED FOR MFE-4

Material	Form
Ti	Bare pure-element wire; Pt-encapsulated wire
Fe	Bare pure-element wire; Pt-encapsulated wire
Ni	Bare pure-element wire; Pt-encapsulated wire
Cu	Bare pure-element wire; Pt-encapsulated wire
Nb	Bare pure-element wire; Pt-encapsulated wire

at the high irradiation temperatures. The selection of the dosimetry materials for this experiment was based on the use of the same specific samples for both radiometric counting and helium analysis. This use of the same monitors for multiple dosimetry analyses is highly advantageous, both because the number of dosimetry materials is minimized, providing a significant savings in space, and because the results of the two dosimetry techniques can be correlated directly using the same samples.

VI. REFERENCES

1. D. W. Kneff and H. Farrar IV, "Helium Accumulation Fluence Dosimetry for Irradiations MFE-1 and MFE-2 at the Oak Ridge Research Reactor," in Damage Analysis and Fundamental Studies, Quarterly Progress Report January-March 1978, DOE/ET-0065/1, U.S. Department of Energy, August 1978.

2. D. W. Kneff, H. Farrar IV, and M. M. Nakata, "Helium Accumulation Fluence Dosimetry for the MFE Spectral Characterization and MFE-1 Irradiations at the Oak Ridge Research Reactor," in Damage Analysis and Fundamental Studies, Quarterly Progress Report April-June 1979, DOE/ET-0065/6, U.S. Department of Energy (May 1979).

3. L. R. Greenwood and R. R. Heinrich, "Flux Gradients and He Calculations for ORR-MFE 1," this volume.

4. E. P. Lippincott, W. N. McElroy, and H. Farrar IV, "Helium Production in Reactor Materials," in Nuclear Cross Sections and Technology, Vol. I, R. A. Schrack and C. D. Bowman, eds., pp. 375-377, National Bureau of Standards Special Publication 425, U.S. Department of Commerce (1975).

5. D. W. Kneff, H. Farrar IV, and M. M. Nakata, "Helium Analyses of Be(d,n)- and T(d,n)-Irradiated Pure Elements," in Damage Analysis and Fundamental Studies, Quarterly Progress Report January-March 1979, DOE/ET-0065/5, U.S. Department of Energy (May 1979).

6. H. Farrar IV and D. W. Kneff, "Helium Generation in Twelve Pure Elements by 14.8-MeV Neutrons," Trans. Am. Nucl. Soc. 28, 197 (1978).

VII. FUTURE WORK

Helium accumulation measurements supporting the MFE experiments in ORR will continue. Additional dosimetry and helium measurement samples, including Cr and Mo, will be prepared for the MFE-4 experimental phase scheduled to start in March 1980. Helium analyses will continue, with near-term emphasis on the MFE-2 materials when they become available.

VIII. PUBLICATIONS

A paper entitled "Experimental and Theoretical Determination of Helium Production in Copper and Aluminum by 14.8-MeV Neutrons," by O. W. Kneff, Harry Farrar IV (Rockwell International), F. M. Mann, and R. E. Schenter (HEDL), was submitted for publication in Nuclear Technology.

A paper entitled "Helium Accumulation Neutron Dosimetry for Fusion Program Be(d,n) and Li(d,n) Neutron Test Environments," by D. W. Kneff, Harry Farrar IV, and M. M. Nakata, was presented at the Third ASTM-EURATOM Symposium on Reactor Dosimetry, Ispra, Italy, on October 1, 1979, and has been submitted for publication in the symposium proceedings.

I. PROGRAM

Title: Dosimetry and Damage Analysis
Principal Investigator: L. R. Greenwood
Affiliation: Argonne National Laboratory

11. OBJECTIVE

To establish the best practicable dosimetry at high energy neutron sources.

III. RELEVANT OAFS PROGRAM TASK/SUBTASK

TASK II.A.2 Flux-spectral definition at high energy neutron sources.

IV. SUMMARY

Neutron flux and spectral measurements have been completed for two irradiations to mock-up the Intense Pulsed Neutron Source (IPNS) now under construction at Argonne. Tantalum and uranium targets were irradiated with 500 MeV protons. The uranium target was found to produce about 50% more neutrons/proton.

V. ACCOMPLISHMENTS AND STATUS

A. Flux and Spectral Measurements for the IPNS Spallation Source

L. R. Greenwood (ANL)

Neutron flux and spectral measurements have been completed at the Argonne ZGS Facility to mock-up the IPNS Facility, now under construction. Tantalum and uranium target assemblies were irradiated with 500 MeV protons and neutron and proton dosimeters were placed in two tubes

parallel and perpendicular to the beam axis. A thin aluminum foil was also used to measure the proton beam intensity and spatial distribution using the $^{27}Al(p, \chi)^{22}Na$ spallation reaction.

Table I lists the measured neutron and proton fluxes per incident proton in the prime materials irradiation facility located at about 90° to the beam and about 6" from the center of the target. The neutron measurements only extended to 44 MeV, the present limit of our cross

Table I. FLUX MEASUREMENTS FOR IPNS
(Flux/Proton, Ep = 500 MeV)

Energy Range MeV	Uranium Target	Tantalum Target	Ratio (U/Ta)
Total	5.79×10^{-2}	3.83×10^{-2}	1.51
Thermal	4.51×10^{-4}	8.31×10^{-4}	0.54
>0.1	3.62×10^{-2}	2.09×10^{-2}	1.73
>1	1.14×10^{-2}	6.02×10^{-3}	1.89
>10	1.06×10^{-3}	8.35×10^{-4}	1.27
>20	7.78×10^{-4}	5.65×10^{-4}	1.38
>30	6.00×10^{-4}	3.90×10^{-4}	1.53
>45*	4.06×10^{-4}	2.25×10^{-4}	1.80
Proton Flux (p/cm^2-s) (~20-40 MeV)	$\sim 10^8$	$\sim 10^8$	

* Calculated; measurements stop at 44 MeV

section file.' Calculated fluxes were thus used above 44 MeV to compute our integral values. Proton fluxes were estimated from the ^{7}Li, ^{65}Cu, and ^{51}V (p,n) reactions. We believe that most of the protons are in the 20-40 MeV energy range. Higher energy protons were looked for using the $^{27}Al(p,\chi)^{22}Na$ reaction; however, the observed ^{22}Na activity can be completely accounted for by neutron-induced spallation. This weak proton flux is not expected to cause any significant damage in materials and

does not appear to affect the dosimetry measurements [e.g., the (p,d) reaction is identical to (n,2n), etc.].

Figure 1 shows the spectra determined with the STAYSL code. Input spectra were provided by neutronics calculations, which roughly agree with our measurements, including flux gradients both perpendicular and parallel to the beam axis. Whereas the neutronics calculations agree quite well in magnitude with the tantalum measurements, the uranium target results are about 50-70% higher than calculated. This difference is not understood, although the calculations do not include all known effects, such as fission in uranium.

As can be seen in Table I, the uranium target produces about 50% more neutrons/proton than the tantalum target. In addition, the U spectrum is slightly harder than Ta so that calculated displacement damage rates are 60-70% higher for the U target. Hence, uranium is the clear choice for damage production at a spallation source.

VI. REFERENCES

1. L. R. Greenwood, Extrapolated Neutron Activation Cross Sections for Dosimetry to 44 MeV, ANL/FPP/-TM-115, (1978).

VII. FUTURE WORK

This work was presented informally at the APS meeting in Knoxville, Tennessee, October 1979. A paper is being prepared for publication.

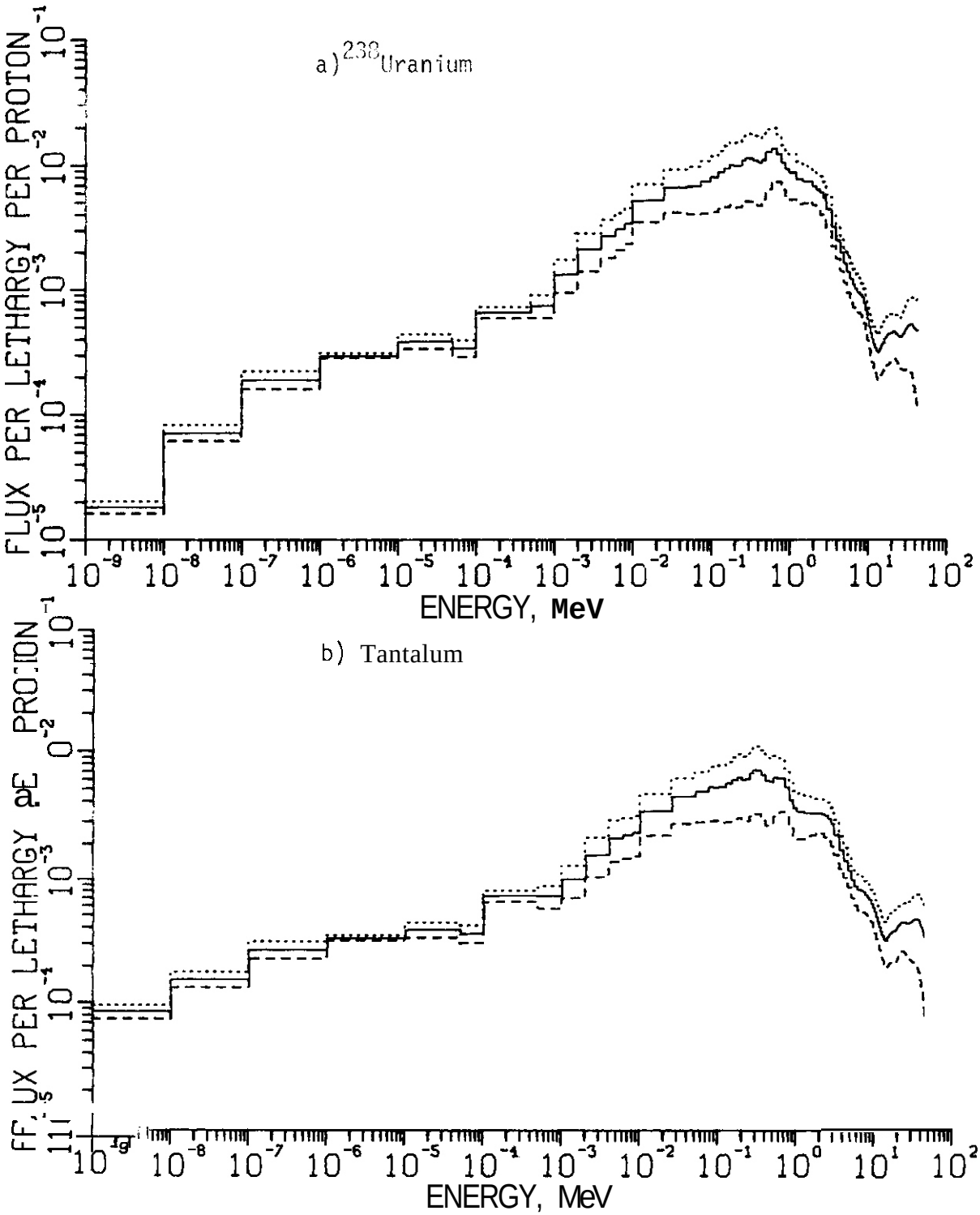

Figure 1. Neutron flux spectra unfolded with the STAYSL code using 28 reactions. A 500 MeV proton beam was stopped in a) a ^{238}U and b) a Ta target. Flux times neutron energy is shown per incident proton.

CHAPTER 4

SUBTASK B: DAMAGE PRODUCTION

I. PROGRAM

Title: Damage Analysis and Dosimetry Radiation Damage Analysis
Principal Investigator: A. N. Goland
Affiliation: Brookhaven National Laboratory

II. OBJECTIVE

Radiation damage analysis studies associated with the use of electrical insulators in fusion reactors.

111. RELEVANT DAFS PROGRAMS PLAN TASK/SUBTASK

SUBTASK II.A.2.4 Flux Spectral Definition in FMIT

SUBTASK II.B.l Calculation of Displacement Cross Sections

IV. SUMMARY

Transport calculations made using two different versions of the MORSE neutron transport code yield neutron flux spectra that are consistent and gamma ray flux spectra that are inconsistent. The cause of this difference is not yet determined.

The status of efforts to evaluate ionization assisted displacement cross sections is reported. The results of Yarlagadda and Robinson for C–C and He-Si ion-atom systems have been duplicated. The extension of these evaluations to constituents of insulators is complicated by the lack of experimental data and limitation of theories describing ion-atom collisions.

V. ACCOMPLISHMENTS AND STATUS

Neutron Flux Characterizations and Damage Analysis Studies--

A. N. Goland, H. C. Berry, G. F. Dell, and O. W. Lazareth (BNL).

1. Transport Codes

Preliminary calculations using the Livermore version of the MORSE neutron transport code, MORSE-L, yielded gamma ray fluxes having greater magnitude and average energy than the fluxes obtained using the RSIC version of MORSE. If real, these fluxes would require a reevaluation of the importance of gamma rays in producing displacement at an FMIT facility.[1]

The special source subroutine that is used to generate neutrons from Li(d,n) reactions was incorporated into MORSE-L, and comparison runs were made using the two versions of MORSE. The neutron spectra obtained are consistent with each other, but the gamma ray spectra are different. A comparison of these spectra is shown in Figures 1 and 2.

There is a certain amount of arbitrariness in selecting the input parameters that govern gamma ray generation in the two codes. Attempts were made to select parameters that would not bias or distort the gamma ray spectra. The differences between the results from the two codes is not yet understood and will require further consideration.

2. Ionization Assisted Displacement Cross Section

The fraction of primary recoil energy that is expended in producing displacements decreases as the primary recoil energy increases. For elements having masses up to and including silicon, less than half of the energy of a 100 keV recoil atom is dissipated in producing recoil atom damage. For the hard neutron spectra anticipated at the FMIT facility, recoil energies in the MeV range will be common, and much of the PKA energy is expected to be dissipated by processes other than those giving rise to the Lindhard stopping power.

Yarlagadda and Robinson have estimated the cross section for producing displacements through Coulomb repulsion between ions and atoms.' This ionization assisted damage mechanism should only be important in insulators.

We have started to evaluate the ionization assisted cross sections for low Z elements such as C, N, O, Mg, Al, and Si that are constituents of many insulator candidate materials. The first step in this task has been to reproduce the results of Yarlagadda and Robinson.

Yarlagadda and Robinson used the C-C ion-atom data of Fortner et al.[3] to estimate the stopping power due to K shell ionization, and they used the binary encounter approximation[4] to obtain the stopping power due to L shell ionization of silicon by helium ions. Their results for C-C were small compared to the Lindhard nuclear stopping power, whereas their results for He-Si were large compared to the Lindhard nuclear stopping power.

We have duplicated the results of Yarlagadda and Robinson. In addition we find that the stopping power due to K shell ionization of Si by helium ions is always smaller than the Lindhard stopping power just as it was for K shell ionization in the C-C case. This finding suggests that it is necessary to include the L and M shells if one is to obtain a realistic evaluation of the magnitude of the ionization assisted stopping power for recoil atoms.

The extension of these calculations to other materials is made difficult by the lack of experimental data for the ion-atom systems of interest as well as by the rapid decrease of the validity of the binary encounter approximation for projectiles heavier than helium.

VI. REFERENCES

1. A. N. Goland, H. C. Berry, G. F. Dell, and O. W. Lazareth, Damage Analysis and Fundamental Studies Quarterly Technical Progress Report, April-June 1979, p. 44, DOE/ET-0065/6.

2. B. S. Yarlagadda and J. E. Robinson, Journal of Nuclear Materials 63 (1976) 466.
3. R. J. Fortner, B. P. Curry, R. C. Der, T. M. Kavanagh, and J. M. Khan, Physical Review 185 (1969) 164.
4. J. D. Garcia, R. J. Fortner, and T. M. Kavanagh, Reviews of Modern Physics 45, 111 (1973) 175.

VII. FUTURE WORK

Continued effort will be made to evaluate ionization cross sections for ion-atom systems of interest for insulators. The binary encounter approximation will be used to evaluate the cross sections for hydrogen and helium ions. For heavy ions such as recoil atoms, theoretical values normalized to existing data will be used to estimate the ionization cross sections.

The ionization cross sections will be used to determine the stopping power due to the ionization assisted mechanism, and these stopping powers will be used in the damage code DON to evaluate the damage, due to ionization assisted processes, to materials exposed to FMIT neutron spectra.

VIII. PUBLICATIONS

G. F. Dell, H. C. Berry, A. N. Goland, and O. W. Lazareth. Calculation or Radiation Damage in Insulators for Fusion Reactors. Journal of Nuclear Materials 85&86, 373 (1979).

Allen N. Goland, Experimental Evaluation of the Primary Damage Process-Neutron Energy Effects. Journal of Nuclear Materials 85&86, 453 (1979).

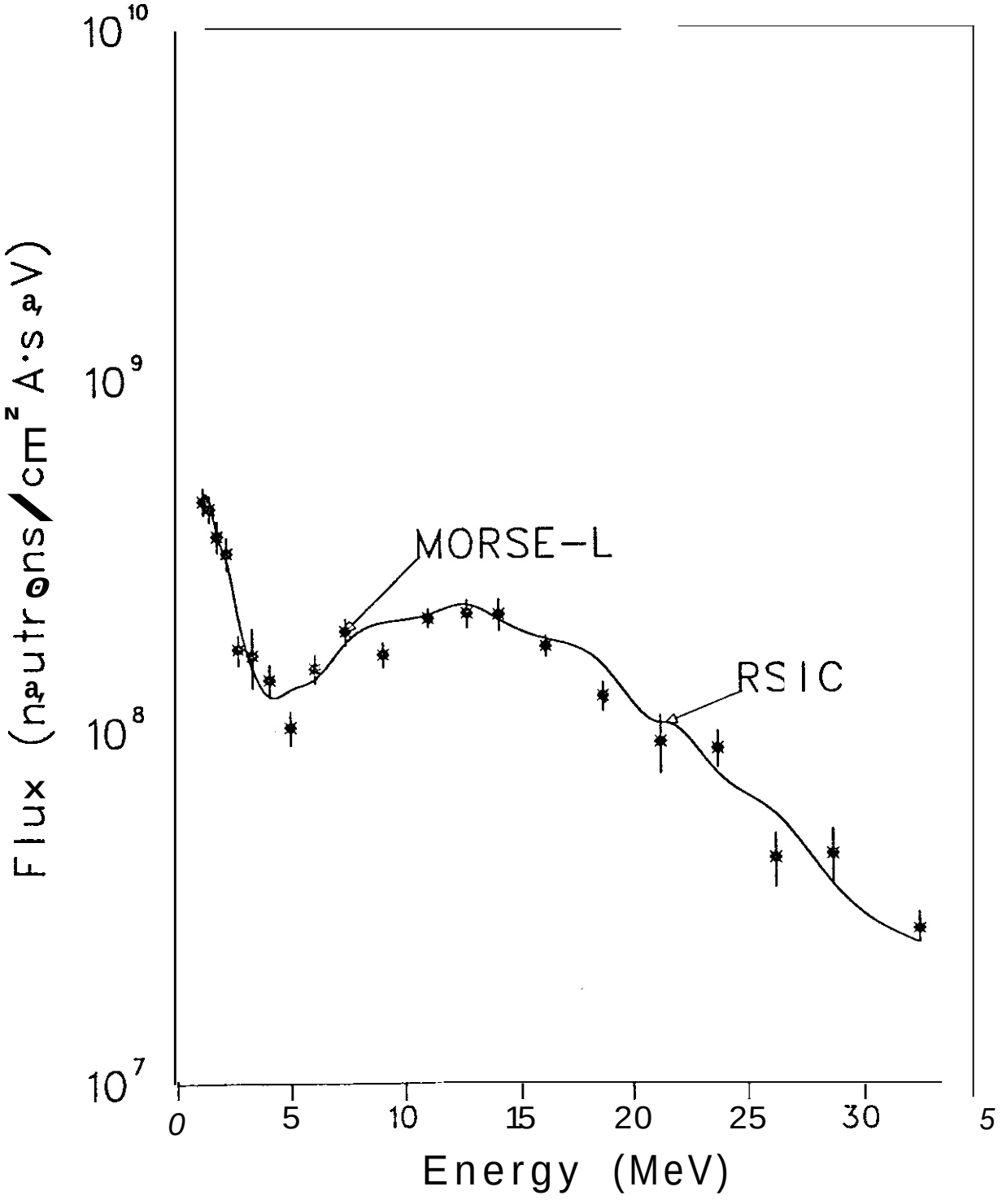

Figure 1 Neutron **fluxes** at a depth of 8cm along the central axis of a $30 \times 20 \times 20$ cm^3 Fe block having density of 1.925 g/cm^3 generated by the RSIC and Livermore versions of MORSE.

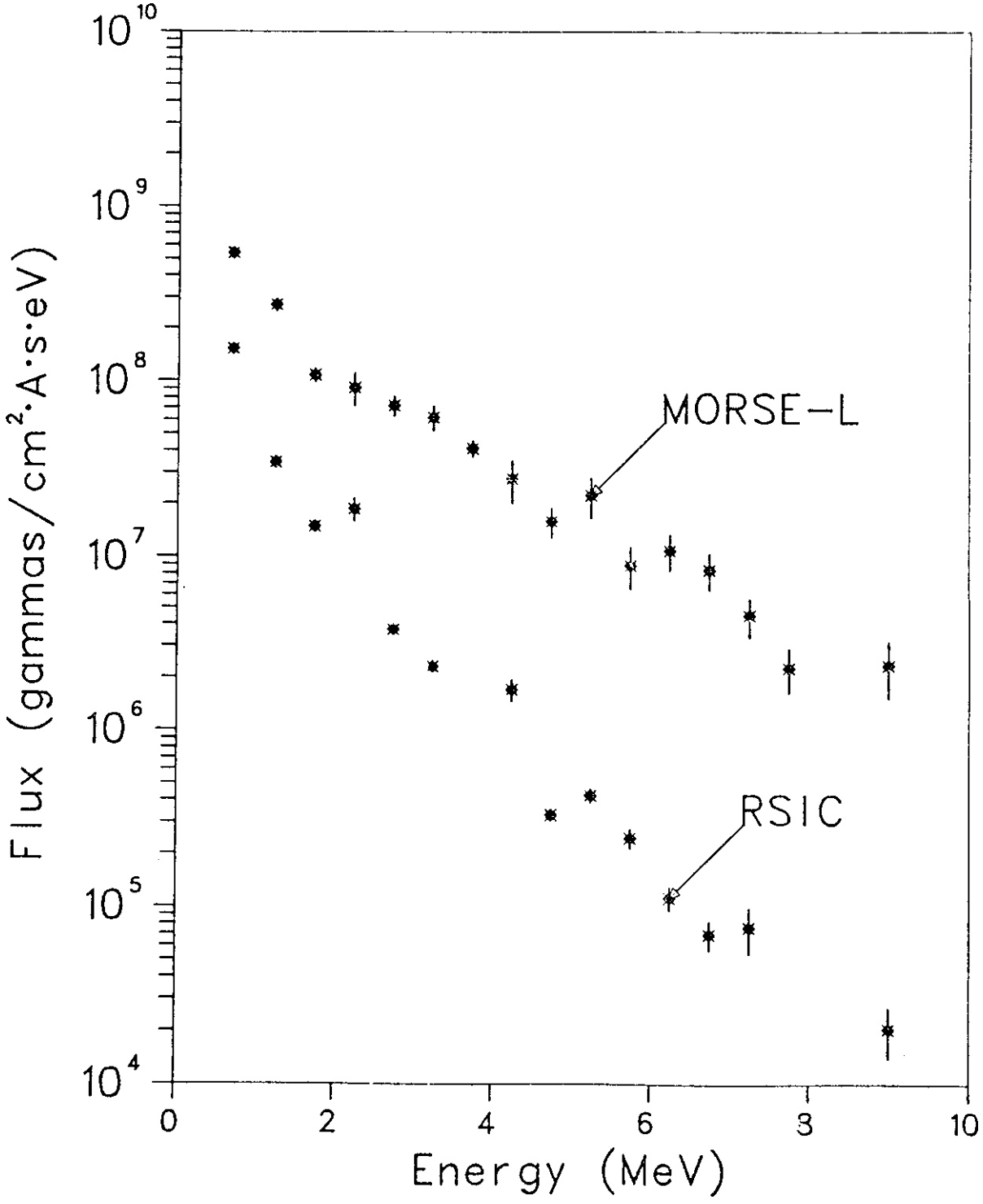

Figure 2 Gama-ray fluxes at a depth of 8cm along the central axis of a 30 × 20 × 20 cm^3 Fe block having density of 1.925 g/cm^3 generated by the RSIC and Livermore versions of MORSE.

I. PROGRAM

Title: Irradiation Effects Analysis (AKJ)
Principal Investigator: D. G. Doran
Affiliation: Hanford Engineering Development Laboratory

II. OBJECTIVE

The objective of this work is to develop computer models for the simulation of high energy cascades which will be used to generate defect production functions for correlation analyses of radiation effects.

III. RELEVANT DAFS PROGRAM TASK/SUBTASK

SUBTASK II.B.2.3 Cascade Production Methodology

IV. SUMMARY

Cascades generated with two versions of MARLOWE, using high and low displacement energies, are compared. Raising the displacement energy makes feasible the simulation of higher energy cascades. Defect yields consistent with resistivity measurements are obtained from both models by application of different energy independent recombination volumes. The resulting cascades are then compared after annealing with the stochastic cascade annealing simulation code SCAS, the calibration of which is described in a separate section of this report. The small differences suggest that a simple adjustment scheme based on defect yields will suffice to account for the adverse effects of raising the displacement energy.

V. ACCOMPLISHMENTS AND STATUS

A. Modeling of Defect Production in High Energy Cascades in FCC Metals - H. L. Heinisch, Jr. (HEDL)

1. Introduction

The binary collision code MARLOWE has been calibrated to yield approximately the same numbers of defects and lengths of replacement sequences as dynamical simulations of low energy displacement events in fcc metals (<1 keV in copper).[1] However, with MARLOWE parameters set to produce the replacement sequences seen in low energy simulations, it is not computationally feasible to model the initial displacement damage in high energy cascades (up to hundreds of keVs) which result from the high energy neutrons striking a fusion reactor's first wall. In this application of MARLOWE, any atom given more than 5 eV is considered part of the cascade (the following MARLOWE parameter settings were used: RB = .62, EBND = .2, EOISP = 5.0, EQUIT = 4.8). With this criterion for displacement, the number of atoms participating in the cascade becomes too large for efficient processing at PKA (primary knock-on atom) energies above perhaps 50 keV, although the energy range of interest extends to several hundred keV. However, 50 keV is well into the beginning of the "high energy region" where displacement cascades form with densities independent of damage energy.[2]

To get to higher energies with MARLOWE it is necessary to exclude atoms from participating in the cascade by raising the displacement criterion above 5 eV. One effect of this is to eliminate long replacement sequences. The minimum energy for production of a displaced atom in copper as determined by dynarnical simulation[3] using the same Moliere potential used in MARLOWE is about 17 eV; we have used this value for the displacement energy in the high energy cascade modeling reported here (i.e., EDISP = 17, EQUIT = 16.8). So far, individual cascades of up to 100 keV have been run with this model.

A primary consideration in this work is that the model used at high energies should maintain as much consistency as possible with the model calibrated for very low energy events. By comparing results in the energy region where both models are applicable, systematic aspects of their differences can be identified and used to calibrate the high energy model.

Both the total numbers of point defects produced and their spatial distributions are important. Therefore, the simulated annealing of the cascades through normal, thermally activated diffusion was performed in order to investigate the importance of differences in the initial spatial distributions of the cascades.

2. Approximating Cascade "Quenching"

Ten cascades of random orientation were generated with MARLOWE at 5 keV and at 20 keV using both the 5 eV and 17 eV displacement energies. At PKA energies above a few keV MARLOWE produces too many defect pairs. For example, for a 20 keV PKA in copper, the average Frenkel pair yield extracted from resistivity data measured for low temperature ion irradiations is 70 pairs, while MARLOWE produces 150 pairs, even after allowing for a "spontaneous recombination distance" of 1.5 lattice parameters. (With a recombination distance of 1 lattice parameter this model yields 215 pairs, about the same as for the modified Kinchin-Pease model.) When the 5 eV displacement energy is used in MARLOWE, the yield after spontaneous recombination is 330 pairs.

Because the resistivity experiments are performed at low temperatures, there should be little recombination due to thermally activated diffusion of defects. The recombination is due to redistribution of the defects during localized quenching of the highly excited cascade region. As a first approximation to simulate the recombination which takes place during the "quenching," a large effective recombination volume is imposed after the cascade development. The resulting yields are shown in the fourth column of Table 1. Using MARLOWE with a displacement energy of 5 eV, and effective recombination radius of 5 lattice parameters provides yields consistent with those extracted from the resistivity data for both the 5 keV and 20 keV cascades, about 20 and 70 pairs, respectively. With the 17 eV displacement energy, similar results were obtained using a 3 lattice parameter recombination radius. Thus, both models appear to give the "measured"

TABLE 1

COMPARISON OF LOW (A) AND HIGH (B) DISPLACEMENT ENERGY MARLOWE CASCADES AFTER SHORT TERM ANNEALING

Defect yields extracted from resistivity data on low temperature ion irradiations are 70±5 pairs for 20 keV PKAs and 20±1 pairs for 5 keV PKAs. The pre-anneal recombination radii are 5 lattice parameters for Model A and 3 lattice parameters for Model B.

Cascade Model	PKA Energy (keV)	τ	No. of Pairs After Pre-Anneal	No. of Pairs at Time τ	VACANCIES			INTERSTITIALS		
					Clusters		Mobile Fraction	Clusters		Mobile Fraction
					Average Number	Average Size		Average Number	Average Size	
A	20	1000	72±5*	65±6*	0.2	5.5	98%	18	4.1	89%
B	20	1000	68±5	54±5	0	-	100%	17	4.5	86%
A	≥20	End	72±5	55±8	4.9	7.5	34%	≥.0	4.7	83%
B	≥20	End	68±5	44±8	2.9	7.6	50%	≥.0	5.2	76%
A	5	1000	22±2	20±3	0	-	100%	0.2	4.0	96%
B	5	1000	19±2	15±2	0	-	100%	0.3	4.3	91%
A	5	End	22±2	18±4	1.2	7.5	50%	0.4	4.7	90%
B	5	End	19±2	12±2	0.8	8.1	44%	0.2	5.0	93%

* One standard deviation

defect yields when an appropriate recombination volume, independent of energy, is imposed. It is encouraging that the defect yields can be obtained from this simple, energy independent model, which has as its physical basis only the notion that the closest pairs have the highest initial probability of recombination. However, the model has little basis for predicting the actual spatial distribution of the defects.

Some details of the spatial distribution of defects in MARLOWE runs for the same PKA using high and low displacement energies were compared after imposing recombination criteria to bring them to about the same number of Frenkel pairs. The distributions of vacancies along the PKA direction were very similar, which might be expected since the primary effect of the higher displacement energy is the truncation of replacement sequences. The major discrepancies were in the distribution of the interstitial defects.

3. Short-Term Annealing Results

One way of evaluating the nature of the differences in the defect configurations achieved with each model in a statistical sense is by observing their behavior in a simulation of short-term annealing. The degree of recombination and clustering resulting from defect motion indicates the importance of the differences in the initial displacement damage. In practice, cascades are produced at temperatures such that some short-term annealing takes place, so the differences observed after simulated annealing are significant.

The 5 keV and 20 keV cascades generated with both high and low displacement energies were annealed using the SCAS annealing code (see Section B). The annealing was carried out using the relative jump rates and critical reaction distances which were found to give the best results in the calibration of SCAS (see Section B). To simulate the quenching of the cascade region, the low displacement energy cascades were given a pre-anneal treatment by recombinipg pairs using a radius of 5 lattice parameters. The high displacement energy cascades were pre-annealed using a 3 lattice

parameter radius. Thus, for both models, the cascades had about the "measured" number of pairs when the annealing simulation began. Results averaged over ten cascades in each case are shown in Table 1 for two stages of annealing. The first stage corresponds to a simulated time equal to that for 1000 jumps by a single interstitial. At this time few, if any, single interstitials remain and few vacancy jumps have occurred, a condition corresponding to an irradiation at about room temperature. The second stage is at a simulated time equal to the lesser of 10^{12} single interstitial jumps or the exhaustion of all mobile defects from the cascade volume. The information on clusters refers only to those considered immobile (see Section B), while the "mobile fraction" refers to that percentage of the total number of remaining defects which is mobile.

At τ = 1000 jumps the only significant difference between the two cascade models is in the total number of remaining defects i.e., the degree of recombination. Essentially all vacancies are mobile, and the interstitial clusters which have formed are of about the same average size and number in both models. The fractions of remaining defects which are mobile are also very similar, though the numbers of mobile defects are not.

At the "end" of annealing slightly more recombination has occurred, and the vacancies have formed immobile clusters. The characteristics of the interstitial population are much the same as at τ = 1000, and the two models continue to agree well on the interstitials. The numbers of vacancy clusters disagree somewhat, especially for 20 keV. It is interesting to note that the mobile fractions of vacancies are not the same, but the number of mobile vacancies is about the same for each model.

This behavior is consistent with the usual concept of a cascade consisting of a vacancy-rich region surrounded by a somewhat more diffuse cloud of interstitials. The closer proximity of the interstitial distribution to the vacancy core in the high displacement energy model (which suppresses replacement sequences) allows for more of them to recombine with vacancies, though nearly the same fraction of remaining interstitials become mobile defects.

4. Conclusions

The overall results of this comparison of models are very encouraging. On the basis of comparison after short-term annealing, the high displacement energy model of MARLOWE produces cascades with essentially the same character as the cascades produced with the low displacement energy model, except for the amount of recombination. This should lead to a simple calibration of MARLOWE for high energy cascades, with defect yields being the most important consideration.

Other questions remain to be answered, however. The spatial distribution of clusters remaining after annealing should be compared for the two models. The pre-anneal treatment, representing "quenching" of the cascade might be modeled in a simple but more realistic way than just recombination of single defects. It is likely that some clustering of interstitials and vacancies occurs during this process. These problems and others will continue to be investigated as the modeling of high energy cascades proceeds.

B. Stochastic Cascade Annealing Simulation - H. L. Heinisch, Jr. and D. G. Doran (HEDL), D. M. Schwartz (Cal. State Univ., Northridge)

1. Introduction

MARLOWE can model the initial displacement stage of the cascade development, but to model subsequent behavior there must be another tool which, like MARLOWE, can produce statistically meaningful results with a reasonable expenditure of computational effort. The Stochastic Cascade Annealing Simulator computer code (SCAS) is such a tool. SCAS is an atomic level simulation which allows defects, each associated with a lattice site, to migrate and interact stochastically in accordance with given jump rates and critical interaction distances. SCAS was developed as a higher speed, but somewhat less physically-based, sequel to the Hybrid Annealing Program (HAP)[4] with the objective that SCAS could routinely handle the annealing

of large numbers of high energy cascades.

2. Calibration of SCAS

SCAS was run with the same set of 5 keV and 20 keV MARLOWE cascades as had been annealed with HAP in order to test the validity of the simplifications employed in SCAS to increase its computational speed. In SCAS all defect clusters are assumed spherical and centered on fcc lattice sites, defects interact with others which fall inside a spherical critical reaction volume without regard to the proximity of other defects, and mobile defect clusters are moved as a whole one lattice site at a time. In HAP the individual point defects maintained their identity and were allowed jumps correlated to their association with a particular cluster. Spontaneous vacancy-interstitial annihilation regions were defined by a set of lattice sites surrounding the defects.

In HAP a mobile defect was followed until its distance from all other defects was greater than a fixed value. The point of termination of an annealing simulation of an isolated cascade was somewhat open-ended; runs were stopped if no reactions occurred during some large number of jumps. In SCAS a mobile defect which wanders beyond a set of fixed boundaries is no longer followed. Runs are routinely allowed to continue until no mobile defects remain within the volume.

With relative jump frequences and critical reaction distances chosen to represent the corresponding HAP values, SCAS runs were done on the same sets of ten different 5 keV and 20 keV cascades generated with an early version of MARLOWE, which were part of the original input to the HAP annealing study.(5)

In SCAS a critical reaction parameter is defined for the interaction of any two defects. The fcc lattice sites are defined in terms of half-lattice parameters, and if squares of distances are used, all distance calculations can be done in integer arithmetic. A cluster is assumed to

have a radius of $(\frac{3n}{2\pi})^{1/3}$ where n is the number of defects in the cluster. Then, two defects interact if the square of the distance from their centers is less than or equal to

$$\text{INTEGER}\left([R(S_1,T_1) + R(S_2,T_2) + D(T_1,T_2)]^2 + 1\right)$$

where $R(S_1,T_1)$ and $R(S_2,T_2)$ are the radii of clusters of size S_1 and S_2 respectively and types T_1 and T_2 respectively. The increment $D(T_1,T_2)$ is an adjustment such that the range of interaction of different types of defects may be different.

The best comparison of **HAP** and **SCAS** results was achieved with D set such that a vacancy could cluster with another vacancy only if it were at a nearest neighbor position, interstitials would cluster with others at up to third neighbor distances, and annihilations of vacancies with interstitials would occur for all which were second neighbors or less. These critical reaction distances are, on the whole, somewhat smaller than those used in **HAP.** In both models vacancy clusters up to size four and interstitial clusters up to size three are considered mobile, and the relative jump frequencies of the different mobile species were the same in both models. Results are fairly insensitive to the jump frequencies.

HAP and SCAS were compared at three stages of annealing:

(1) at $\tau = 0$, before any motion, but after spontaneous reactions had occurred,
(2) at $\tau = 1000$, i.e., after the simulated time interval it would take a single interstitial to make 1000 jumps, and
(3) at the nominal "end of annealing," which occurs in **SCAS** when no mobile defects remain in the volume.

Since the second neighbor **SCAS** recombination volume contains fewer sites than **HAP's** 32-site region, less annihilation is expected to occur. However, the clustering model in SCAS assumes that point defects are coalesced into larger spherical defects centered on a single lattice

point. Clustering at $\tau = 0$ in SCAS therefore has the effect of changing the relative position of some defects, and further annihilation is possible because of this reshuffling during the clustering procedure. Thus, the number of pairs surviving in SCAS before this clustering is slightly greater than in HAP, but after clustering it is slightly less as reported in Table 2.

At $\tau = 1000$ interstitial jumps most annihilations have occurred and the vacancies have not yet moved. Few mobile interstitials remain. It is near the end of the most active part of the annealing. Table 2 shows that at this point the average number of pairs and the fractions of remaining defects which are mobile are the same by both models. After this stage, primarily vacancy motion, resulting in clustering and some additional recombination, occurs during the simulated time of $\sim 10^{12}$ jumps until no mobile defects remain.

Because of the way clustering is done in SCAS there is little chance for large clusters to form in the pre-annealing spontaneous reactions. As can be seen at $\tau = 1000$ and at the end, the clustering of migrating defects occurs about the same in SCAS and HAP. Some of the differences could be due to the longer effective annealing times simulated by SCAS, as well as the difference in the definition of how the mobile defects leave the system. Despite the major differences in treating the details of defect interactions, the two annealing models give remarkably similar results using interaction and jump parameters which are not inconsistent with each other.

The most significant difference between the models is that of computational speed and cost. While somewhat difficult to assess because of the major differences in computing machinery used, our best estimate is that SCAS is faster/cheaper than HAP by about two orders of magnitude.

TABLE 2

COMPARISON OF HAP AND SCAS ANNEALING OF MARLOWE CASCADES

These cascades are those used in the original HAP work,[5] and have a displacement energy of 25 eV.

Annealing Model	PKA Energy (keV)	τ	No. of Pairs at Time τ	VACANCIES			INTERSTITIALS		
				Clusters		Mobile Fraction	Clusters		Mobile Fraction
				Average Number	Average Size		Average Number	Average Size	
HAP	20	0	159±8 *						
SCAS	20	0	146±6						
HAP	20	1000	81±6	0.7	5.8	95%	6.1	4.5	66%
SCAS	20	1000	86±10	0.4	6.8	98%	7.0	4.8	60%
HAP	20	$\leq n <$	52±9	4.3	8.3	32%	4.4	5.4	55%
SCAS	20	$\leq n \sqsubset$	57±5	4.7	8.1	32%	4.9	5.3	54%
HAP	5	0	42±4						
SCAS	5	0	40±3						
HAP	5	1000	22±5	0.2	$\leq$.0	93%	1.1	4.5	78%
SCAS	5	1000	22±5	0	-	100%	1.4	4.5	71%
HAP	5	End	18±3	1.5	7.2	41%	0.7	5.0	80%
SCAS	5	End	15±4	1.3	6.7	42%	0.7	5.$\leq$	74%

*One standard deviation

VI. REFERENCES

1. M. T. Robinson, OAFS Quarterly Progress Report, October-December 1978, DOE/ET-0065/4.

2. H. L. Heinisch, Jr., DAFS Quarterly Progress Report, April-June 1979, DOE/ET-0065/6.

3. J. O. Schiffgens and R. D. Bourquin, J. Nucl. Mat. 69 (1978) p. 790.

4. D. G. Doran and R. A. Burnett, Interatomic Potentials and Simulation of Lattice Defects, P. C. Genien, J. R. Beeler and R. I. Jaffee, eds., Plenum Press, New York (1972) p. 403.

5. D. G. Doran and J. O. Schiffgens, Proceedings of the Workshop on Correlation of Neutron and Charged Particle Damage, Oak Ridge National Lab, June 8-10, 1976, CONF-760673.

VII. FUTURE WORK

A calibrated MARLOWE cascade model will be used to generate high energy cascades. Studies of their behavior after simulated annealing will continue.

VIII. PUBLICATIONS

H. L. Heinisch, Jr., D. M. Schwartz and D. G. Doran, "Simulation of Short-Term Annealing of Displacement Cascades in FCC Metals," abstract submitted to ASTM Symposium on the Effects of Radiation in Materials, Savannah, Georgia, June 1980.

CHAPTER 5

SUBTASK C: DAMAGE MICROSTRUCTURE EVOLUTION AND MECHANICAL BEHAVIOR

I. PROGRAM

Title: Irradiation Effects Analysis (AKJ)
Principal Investigator: D. G. Doran
Affiliation: Hanford Engineering Development Laboratory

II. OBJECTIVE

The general objective of this work is to define efforts needed under the DAFS program in order to meet program milestones. The specific objective of current work is to assess understanding of radiation damage mechanisms in AISI 316 stainless steel in light of the need to develop fission-fusion correlations.

III. RELEVANT DAFS PROGRAM TASK/SUBTASK

TASK II.C.1 Effects of Material Parameters on Microstructure
II.C.2 Effects of Helium on Microstructure
II.C.14 Models of Flow and Fracture Under Irradiation
II.C.16 Composite Correlation Models and Experiments
II.C.17 Microstructural Characterization

IV. SUMMARY

The DAFS program must be responsive to recent chanpes in schedules of major fusion devices, especially ETF*. A review is in progress of needed modeling, analysis, and experimental work. The emphasis is on the extension of the data base and associated analyses developed under the Breeder Reactor Program, especially on AISI 316 stainless steel, to fusion design environments and integration of those efforts with ETF demand dates.

* Engineering Test Facility, currently in the conceptual design phase at Oak Ridge National Laboratory.

V. ACCOMPLISHMENTS AND STATUS

A. Review of Needs for Developing Fission-Fusion Correlations - F. A. Garner (HEDL)

1. Introduction

One of the major objectives of the DAFS program is the development and application of a methodology, based on damage mechanisms, for correlating the mechanical and dimensional behavior of materials exposed to diverse test environments (largely fission reactors) and projecting this behavior to magnetic fusion reactor environments. In order to address this objective, an assessment has been proceeding to determine the following:

(1) What constitutes the full array of damage mechanisms to be considered?

(2) What needs to be done to provide models of these mechanisms?

(3) How are these models to be applied to fission-fusion correlation efforts?

While this assessment is only partially complete, a preliminary outline of the necessary research is emerging and is presented in this report. Some of the damage mechanisms that have been identified as requiring attention are already under study (e.g., see Reference 1).

The assessment has proceeded in light of the major considerations listed below.

(1) The Engineering Test Facility (ETF) schedule and milestones have been set and require short-term input from the DAFS effort.

(2) The DAFS Task Group has been reorganized recently to provide increased emphasis on fundamental mechanical behavior. (See Chapter 1).

(3) Fission-fusion correlations require both an adequate data base covering relevant fluence-flux-temperature regimes and adequate descriptions of the operating damage mechanisms. AISI 316 is the one alloy in the US fast reactor program for which a sufficient amount of data exists to discern the competitive and synergistic influence of many important variables. Data on AISI 304 comprise the second largest data set. However, not all of the important damage mechanisms have yet been identified for these two alloys.

(4) AISI 316 has been selected as the primary structural material for the first conceptual design of ETF. Ferritics may be included subject to the outcome of a short-term research program initiated under the Alloy Development for Improved Performance (ADIP) program.

(5) The first wall of ETF is currently slated to operate at temperatures of 50-300°C in order to avoid the use of liquid metal coolants. As yet undefined higher temperatures will occur in ETF in various experimental test modules. The overwhelming majority of the fast reactor-generated data base lies above 375°C, the exception being some UK measurements at temperatures approaching 270°C, the inlet temperature of DFR.

(6) It has recently been recognized that the radiation-induced mechanical. and dimensional changes of AISI 316 are strongly influenced by a complex microchemical evolution of the alloy matrix that develops concurrently with the microstructural evolution. The instantaneous matrix microchemistry of this steel has been found to be sensitive to the preirradiation thermal mechanical treatment, temperature history, displacement rate, neutron spectrum, stress and the helium level, all of which must be considered in the fission-fusion correlation process.

(7) Additional data on the property changes and microchemical evolution of AISI 316 obtained in the breeder program are being finalized for dissemination and incorporation into the fusion effort.

(8) The use of charged particle bombardments and even mixed spectrum fission reactor irradiations provide at best simulations of the response of a material to a fusion environment. Previous studies of charged particle/ fast reactor correlations have demonstrated the caution with which the results of simulation experiments must be employed.

2. Areas Requiring Attention

a. Data Needs

The most critical near-term DAFS requirement is the collection and development of a low temperature data base on AISI 316 in order to contribute to completion of various ETF design milestones, the earliest being September 1980. Any data available in the short term will be derived

from low flux, low fluence irradiations and from heats of steel different from that employed in the breeder program. There is also very little microstructural information at these temperatures on which to base correlations. An effort to collect and interpret the available data has been initiated. An immediate objective of this effort is to help guide low temperature irradiation experiments in mixed spectrum reactors.

b. Microstructural/Microchemical Evolution

For the temperature range 370-700°C the microstructural development of AISI 316 in fast reactor spectra is quite well known. There are also some data developed in the HFIR reactor for this temperature range. Correlations based on the action of microstructural components are therefore well founded. What is not as well known is the appropriate description of the sink capture efficiencies needed to describe swelling, irradiation creep, microchemical evolution of the matrix, and various segregation phenomena. There is no satisfactory model for the basic compositional dependence of irradiation-induced property changes, or for the dependence on various solute species. Furthermore, satisfactory explanations do not exist for the behavior of ferritic alloys relative to that of austenitic alloys, and for the development of vacancy loops in some alloys and under some irradiation conditions, but not others.

The following actions have been initiated to address these needs.

(1) Models are being developed for the action of major solutes in AISI 316. The first effort on the action of silicon in AISI 316 and other alloys is included in a companion report.(1)

(2) Summaries are being prepared from all available data on the apparent role of each element whose influence has been identified as a major one in the determination of the irradiation response of AISI 316.

(3) The dependence of phase development in AISI 316 on all major environmental or fabrication variables is being reviewed and compiled to aid in performing fission-fusion correlation. Each of the phases in AISI 316 has

been found to be sensitive to a different array of variables.

(4) A model is being developed which will describe the dependence of swelling, creep and mechanical properties on starting composition in ferritic and Fe-Ni-Cr alloys, and also on instantaneous matrix composition in AISI 316. This effort involves the compositional dependence of sink biases. The model is now conceptual in nature but mathematical models are currently being developed.

(5) Joint efforts with other laboratories are being initiated to test the validity of several available theories describing sink capture efficiencies which form the basis of the models being developed in (4).

(6) Although the microstructural evolution of AISI 316 is fairly well known, identification of the damage mechanisms giving rise to particular microstructural features is not straightforward. Consider, for example, the double-peaked swelling and creep profiles observed in AISI 316 reactor components and the bimodal void populations observed in the alloy at higher temperatures. Each of these phenomena has been shown recently to have a microchemical description rather than previously advanced microstructural and diffusion-based descriptions. Continued efforts to identify relevant mechanisms are expected to aid in the projection of fission data to fusion environments.

c. Mechanical Properties

Whereas most previous microstructural/microchemical modeling efforts by this author focused on swelling and creep, attention is now being directed toward mechanical properties. The first effort undertaken in this area involves a microstructural/microchemical explanation of yield strength and ductility data on both annealed and cold-worked AISI 316 irradiated in fast reactors. The major new insight gained in this effort has been that the interactive microchemical and microstructural evolution of this steel can be used to explain both the low-temperature hardening and the high fluence saturation of these properties at all relevant temperatures.

d. Spectrum/Flux Considerations

One of the major requirements for fission-fusion correlations is the development of an adequate description of the effect of the different energy deposition and damage characteristics of the two neutron environments. To help meet this need, DAFS programs are in progress utilizing mixed spectrum reactors and RTNS-II. The proper extrapolation to higher fluences will also require an adequate incorporation of spectrum dependence in the original data sets. In correlations developed for the breeder program, the neutron spectrum dependence has been incorporated only through a neutron energy threshold (0.1 MeV) or, in a few cases, the parameter dpa. Perhaps more importantly, the effect of displacement rate (flux) has not been incorporated. (Both flux and spectrum effects may be buried in an apparent temperature dependence.) Since flux and spectrum effects are intimately linked for data obtained in the EBR-II, DFR. Rapsodie and Phenix fast reactors it is important that breeder correlations be reformulated to include such variables prior to attempting to extrapolate to the fusion environment. Since the radiation-induced evolution of AISI 3i6 has been found to be very sensitive to displacement rate, the separate influence of these variables must be incorporated into existing correlations.

The influence of spectrum on helium production is adequately covered in other DAFS programs and will not be included in this effort.

e. Helium Effects

HFIR irradiations show that the microstructural and microchemical evolution of AISI 316 is sensitive to the helium content. The swelling of this steel has been shown to be quite sensitive to helium also. There are existing experimental efforts, utilizing either dual ion or fast and mixed-spectrum reactor irradiations, directed toward identifying the effect and role of helium. Unfortunately, not even the reactor experiments are single-variable experiments; differences in flux and spectrum complicate their interpretation in terms of helium content.

To complement these simulation experiments, two different single-variable (helium) experiments have been proposed which could be performed using currently existing EBR-II irradiated material. These efforts involve only microscopy. These are the helium halo technique[2] and the recoil-injection/pressurized tube technique. The latter involves the examination of the inner wall near-surface material of creep experiment tubes. The analytical tools necessary to interpret the microscopy data are being developed and an inventory is being conducted of available specimens.

VI. REFERENCES

1. F. A. Garner and W. G. Wolfer, "The Effect of Solute Additions on Void Nucleation," this report.

2. F. A. Garner and D. S. Gelles, "Analysis of the Helium Halo Effect In Neutron-Irradiated Alloys," DAFS Quarterly Report No. 4, DOE/ET-0065/5.

VII. FUTURE WORK

Each of the areas covered in this report will continue with primary emphasis on microstructural/microchemical modeling, low temperature AISI 316 data acquisition and modeling of mechanical properties. Efforts will be made to report relevant data generated under the breeder program as it is released in order to ensure effective and timely utilization by the fusion materials community. The discussion in this report will be used in a current task group assessment of DAFS milestones.

I. PROGRAM

Title: Irradiation Effects Analysis (AKJ)
Principal Investigator: D. G. Doran
Affiliation: Hanford Engineering Development Laboratory

II OBJECTIVE

The objective of this effort is to model the effect of various solute additions on void nucleation in irradiated metals

111. RELEVANT OAFS PROGRAM TASK/SUBTASK

SUBTASK II.C.l Effects of Material Parameters on Microstructure

IV. SUMMARY

The fast-diffusing species concept appears to be a viable mechanism for suppression of void nucleation by silicon atoms in AISI 316 and other alloys. The addition of slow-diffusing elements has an opposite but less pronounced effect on void nucleation. The enhanced diffusivity of the alloy which results from the addition of silicon leads to a substantial increase in the free energy barrier to void nucleation, particularly at higher temperatures. The fast-diffusion mechanism operates in addition to the interstitial-solute binding effect, and the combined fast-diffusion/interstitial binding model dispenses with the requirement of unrealistically large interstitial-solute binding energies needed for the solute-binding concept. Solute binding may account for most of the observed silicon segregation behavior while fast-diffusion accounts for the void suppression.

In 316 stainless steel, nickel and silicon are major determinants of the swelling behavior. While the role of silicon can be ascribed at least partially to the fast-diffusion effect, the role of nickel cannot, and its

influence lies in the operation of other physical mechanisms.

V. ACCOMPLISHMENTS AND STATUS

A. The Effect of Solute Additions on Void Nucleation - F. A. Garner (HEDL) and W. G. Wolfer (University of Wisconsin)

1. Introduction

There now exists ample evidence that certain minor alloying elements have a pronounced effect of delaying neutron-induced void formation in many metals and alloys. This suppression of nucleation is effective only as long as the active elements remain in solution. It appears that during irradiation these elements are inevitably removed from the alloy matrix, however, which can lead to substantial alteration of the matrix composition due to coprecipitation of major alloy components into various second phases.[1-3] Venker, Ehrlich and Giesecke[4,5] have recently conjectured that there exists a correlation between the suppression of void formation and the presence of fast diffusing solute or solvent elements. They did not demonstrate, however, that such a correlation arises from a specific physical mechanism.

The conjecture of Venker et al. appears to be an alternative to the concept that defect trapping at solute elements reduces void formation. This possibility has been proposed and analyzed by several authors.[6] The trapping of interstitials and/or vacancies at solute atoms or impurities enhances the probability of recombination, and thereby lowers the supersaturation of vacancies. However, the enhanced recombination by trapping is only significant for vacancy-solute binding energies of 0.3 eV or greater[6] or for interstitial-solute binding energies of the order of or greater than the vacancy migration energy. Binding energies of this magnitude have not been confirmed by experiment for interstitial-solute complexes in fcc metals, and measured vacancy-solute binding energies are generally 0.2 eV or less for substitutional solute elements.[7] The action of trapping and detrapping may be expressed in terms of reducing the effective

diffusion coefficient for the point defect, as has been shown by Mansur.[6] Enhanced recombination by trapping implies slower diffusion rather than faster diffusion.

To determine the relative contributions of the trapping mechanism and the conjecture of Venker et al., it is important to realize that the former process requires immobile or slowly diffusing solute atoms, whereas the latter assumes highly mobile solute atoms. It will be shown in this report that when fast-diffusing solute atoms enhance the vacancy mobility, the vacancy supersaturation is reduced, and the void nucleation rate reduced. Both mechanisms, namely trapping at fixed solute elements and enhanced diffusion due to mobile solutes, lead to a similar suppression of void nucleation, and they appear to be two extreme cases of the effects of mobile vacancy traps.

In the following section the concept of effective vacancy diffusion is examined in a metal with substitutional impurities. The effective vacancy diffusion coefficient is then used in the void nucleation theory to demonstrate that fast-diffusing solutes can significantly reduce void nucleation. The results and their correlation with experimental evidence are examined in the last section.

2. The Effective Vacancy Migration Coefficient

The normal diffusion of substitutional impurity atoms occurs by vacancy migration. For dilute concentrations of impurities, diffusion is commonly analyzed in terms of the five-frequency model,[8] from which Howard and Lidiard[9] have derived an effective diffusion coefficient for vacancy migration. In the present work, we employ the somewhat simpler expression by Flynn,[10]

$$D_v^{eff} = (D_v + K C_s D_s)/(1 + K C_s), \qquad [1]$$

where D_v is the diffusion coefficient for migration of a free vacancy, and D_s is the diffusion coefficient for a solute-vacancy pair. C_s is the solute

concentration, and

$$K = 12 \exp(E_b/kT) \qquad [2]$$

is the rate constant for the solute-vacancy dissociation in an fcc lattice, and E_b is the solute-vacancy binding energy

As shown by Howard and Lidiard, Equation [1] is valid if the concentration of bound vacancies is small compared to the solute concentration C_s. Considering the fact that the steady-state vacancy concentration in metals irradiated in a fast neutron flux is of the order of 10^{-6} per atom or less, this condition is met. A further restriction on the validity of Equation [1] is that the jump frequency of a free vacancy into a bound position must not differ greatly from the jump frequency of an isolated vacancy. Once formed, however, the vacancy-solute pair may possess a jump frequency that differs substantially from that of the free vacancy.

It should be noted that Equation [1] is equally applicable when the flow of solute is in the same or opposite direction to the flow of vacancies. Therefore, both solute drag and inverse Kirkendall effects are compatible with this treatment.

Equation [1] was derived assuming a quenched-in vacancy supersaturation in the absence of self-interstitials. Therefore, its application to metals subject to irradiation is suspect. In a soon to be published paper, Mansur has derived an expression for D_v^{eff} which is more general than Equation [1], and which incorporates the effect of trapping and the recombination of interstitials and bound vacancies, as well as the transport of bound vacancies to sinks. He has shown, however, that trapping can be neglected whenever the binding energy $E_b \gtrsim 5$ kT, i.e., <0.27 eV at temperatures of 350°C or higher. Bound recombination need not be considered as being different from free recombination provided $E_b \lesssim 10$ kT. Finally, transport of bound vacancies has little effect on the effective diffusion coefficient in Equation [1] if

$$E_b \lesssim [10 + \ln (D_v/D_s)]\ kT. \qquad [2]$$

As long as $E_b \lesssim 5$ kT, condition (2) is also satisfied when D_s is no larger than about 100 D_v.

All these conditions are met for vacancy-solute binding energies in the range of measured values. Therefore, Equation [1] may be used as the effective vacancy diffusion coefficient in the conventional rate theory in which the interstitial mobility is much greater than the vacancy mobility.

The vacancy diffusion coefficient for nickel is given by

$$D_v = 0.0153 \exp(-E_v^m /kT) \qquad [3]$$

with E_v^m = 1.4 eV. For an imaginary solute atom in nickel we assume a diffusion coefficient of

$$D_s = 0.0153 \exp(-E_s^m/ kT) \qquad [4]$$

where E_s^m differs from E_v^m at the most by ±0.2 eV.

Figure 1 shows the effective vacancy diffusion coefficient D_V^{eff} for the case that E_s^m = 1.2 eV and E_b = 0.05 eV, and for solute concentrations up to 5 at.%. It is seen that small additions of a fast diffusing solute element greatly enhance the vacancy mobility. Note that relatively minor solute additions are quite effective and that additional solute has a proportionally smaller effect. With increasing solute content, D_v^{eff} approaches D_s at a rate governed by the sign and magnitude of the binding energy E_b.

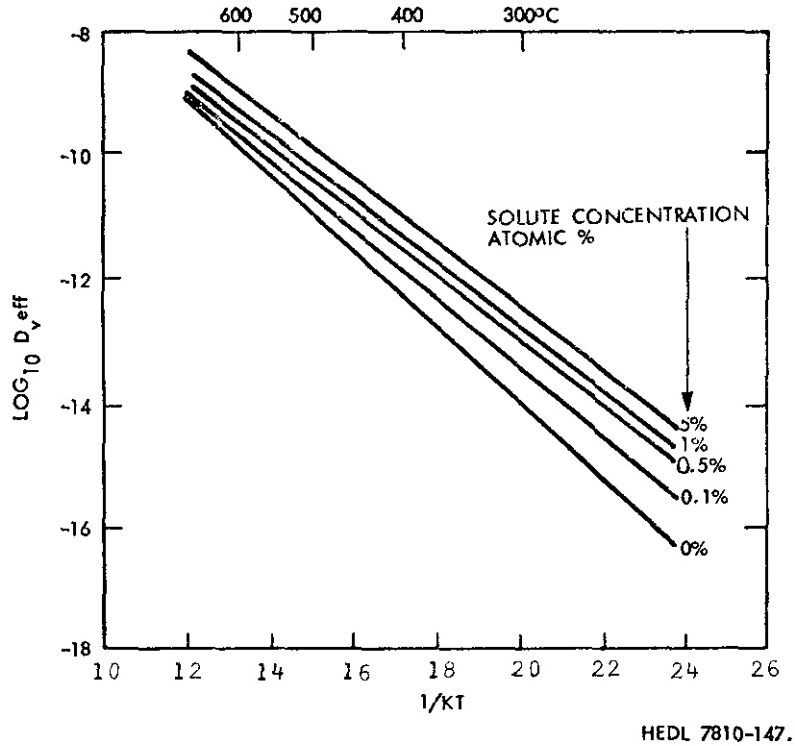

FIGURE 1. Calculated Effective Diffusion Coefficient for Vacancies in Nickel With Various Concentrations of Fast-Diffusing Solute.

3. Void Nucleation Rates

To study the impact of fast-diffusing solute elements on void formation, the nucleation theory of Katz, Wiedersich and Russell[11] (KWR) is utilized in conjunction with the standard rate theory. In the latter, however, the effective vacancy diffusion coefficient D_v^{eff} is substituted for D_v. The nucleation barrier energy $\Delta G(x)$ has been givenpreviously,[12,13] and can be written in the form

$$\Delta G(x)/kT = -\sum_{n=2}^{x-1} \ln \left\{ [\lambda(n)\Delta C_v + C_v^{\circ}(n)]/[\Delta C_v + C_v^{\overline{eq}}] \right\} \qquad [5]$$

where

$$\lambda(n) = \left(1 + \frac{1}{n}\right)^{1/3} \frac{Z_i^{\circ}(n+1)}{Z_v^{\circ}(n)} \frac{\overline{Z}_v}{\overline{Z}_i}, \qquad [6]$$

ΔC_v is the radiation-produced vacancy concentration over and above the average thermal vacancy concentration $\bar{C}_v^{eq}$ in equilibrium with the sinks, and $C_v^\circ(n)$ is the vacancy concentration in equilibrium with a void containing n vacancies. Z_i° and Z_v° are the interstitial and vacancy capture efficiencies of voids, and $\bar{Z}_i$ and $\bar{Z}_v$ are average capture efficiencies of all sinks. All these quantities have been given and discussed extensively elsewhere.(12,13)

The excess vacancy concentration ΔC_v can easily be obtained from the rate equations. Using the materials parameters for nickel as given in Reference 13 and a displacement rate of 10^{-6} dpa/sec, the nucleation barrier $\Delta G(x)/kT$ for "pure nickel" is obtained from Equation [5] as a function of the number of vacancies, x, contained in the void, and the results are shown in Figure 2 for different temperatures.

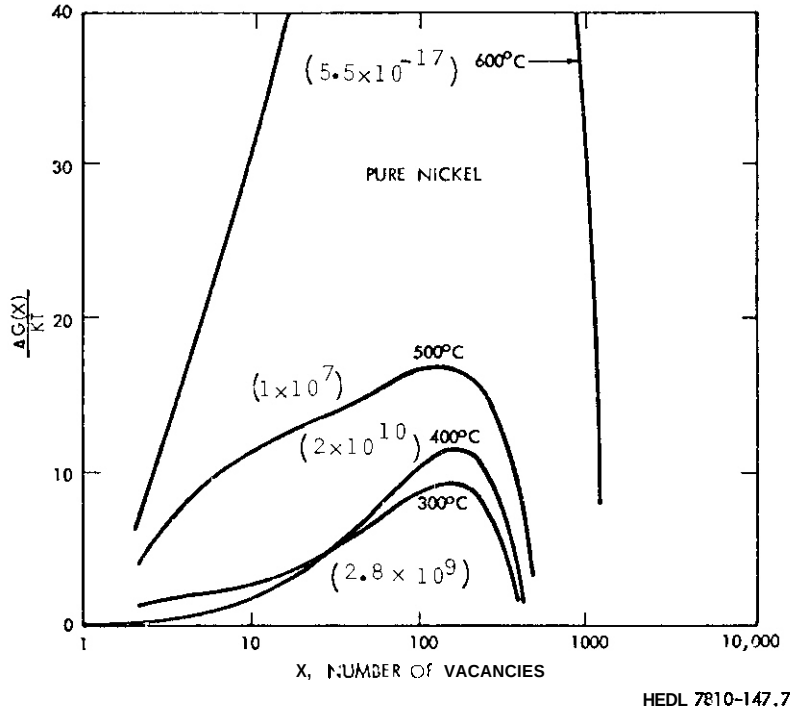

FIGURE 2. Void Nucleation Barrier Calculated for "Pure Nickel". Numbers in brackets are the steady-state nucleation rates per cm^3 and sec.

The numbers in brackets are the steady-state void nucleation rates given by

$$I = 2(6\pi^2\Omega)^{1/3} D_v^{eff} (\Delta C_v + \bar{C}_v^{eq})^2 \left\{ \sum_{x=2}^{\infty} \frac{\exp[\Delta G(x)/kT]}{x^{1/3} Z_v^{\circ}(x)} \right\}^{-1} \qquad [7]$$

In the following, the void nucleation rate for the pure material, i.e., when $D_v^{eff} = D_v$, will be designated by I_o. Note that the nucleation rate for 600°C irradiation is very low because the influence of helium atoms has not been included. It has been shown earlier, however, that the ratios I/I_o are relatively insensitive to the presence of gas when studying the parametric influence of variables such as stress.(13)

The effect of 1 at.% of solute atoms whose activation energy for migration is E_s^m = 1.2 eV and whose binding energy with vacancies is $E_{,,}$ = 0.05 eV is shown in Figure 3.

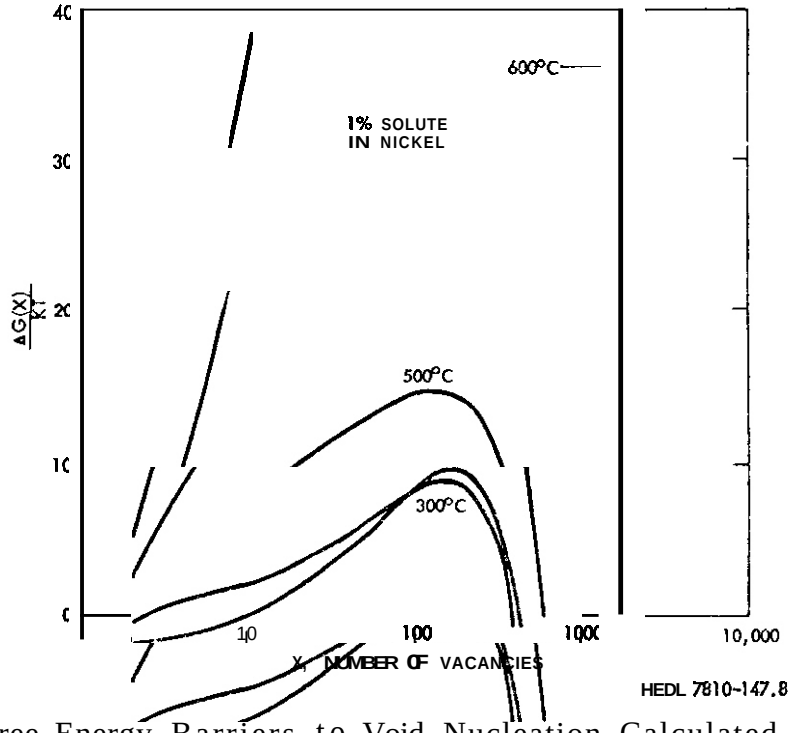

FIGURE 3. Free-Energy Barriers to Void Nucleation Calculated for Nickel-1% Solute Alloy.

Due to the enhanced mobility of vacancies, the nucleation barrier is raised for temperatures where recombination does not dominate the point defect concentrations and the steady state nucleation rate, I, is decreased. This is more clearly illustrated in Figure 4 which gives the relative nucleation rates I/I_0 as a function of the solute concentration C_s.

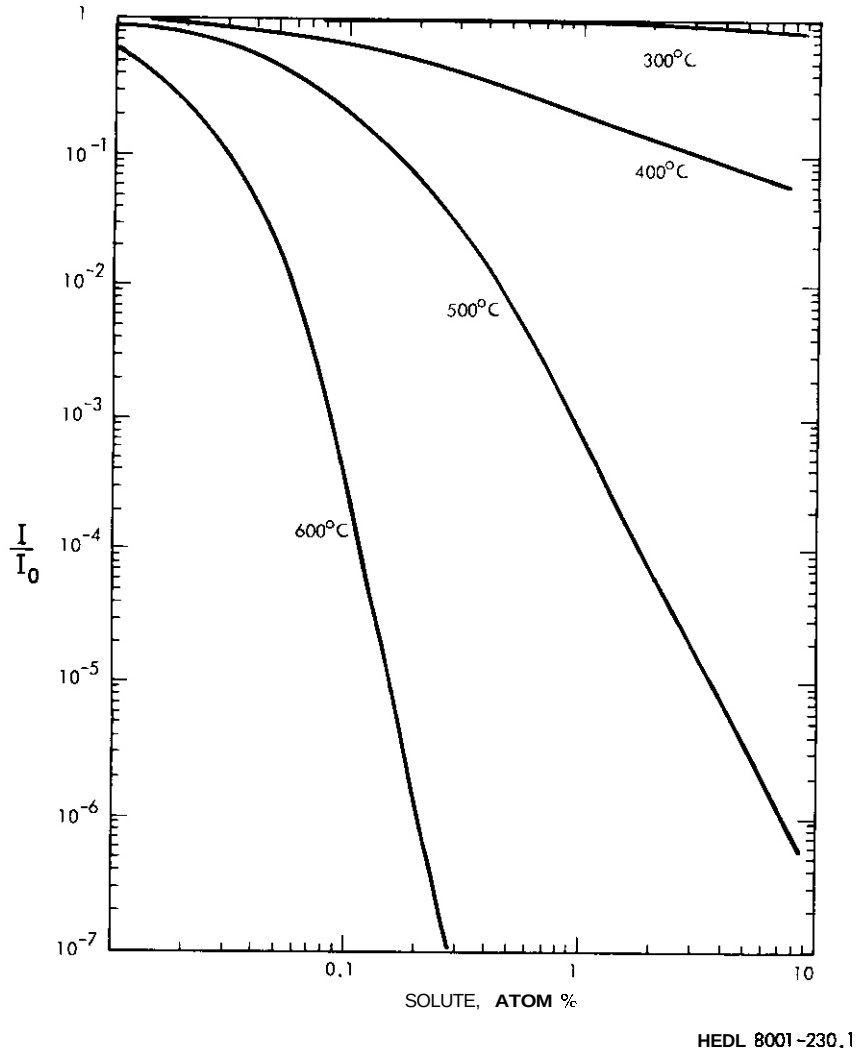

FIGURE 4. Relative Void Nucleation Rates for Solute Additions with E_s^m = 1.2 eV and E_b = 0.05 eV.

These results not only confirm the conjecture of Venker et al., but at the same time demonstrate that fast-diffusing solute additions reduce the void nucleation rate and thereby increase the incubation dose for void swelling. The effect can be interpreted in a simple manner. The enhancement of vacancy mobility by addition of fast-diffusing solutes is analogous to an increase in temperature. In both cases the vacancy supersaturation is reduced, and the void nucleation rate depressed.

This argument can be carried further by considering the influence of slow-diffusing solute additions. Accordingly, several cases have been investigated wherein the solute possesses a migration energy of. E_s^m = 1.6 eV, i.e., 0.2 eV higher than E_v^m. Figure 5 gives the results for 0.1 at.% solute additions. The lower solid curve shows again the fast-diffusing case for solutes with E_s^m = 1.2 eV and E_b = 0.05 eV, whereas the upper solid curve is for a slow-diffusing solute with E_s^m = 1.6 eV and E_b = 0.05 eV. Although the nucleation rate is increased with slow-diffusing solutes, the effect is less pronounced than the corresponding suppression of nucleation by fast-diffusing solutes, provided the binding energy is small.

For strong binding with E_b = 0.2 eV, the slow-diffusing solute (E_s^m = 1.6 eV) produces a more significant increase in the void nucleation rate, as shown by the upper dashed curve. This latter case is considered a very important demonstration that solute trapping of vacancies does not necessarily lead to a reduction in void swelling. In fact, for reasonable binding energies and for a slower but finite mobility of the solute the present analysis leads to the opposite conclusion. This in no way contradicts earlier work on the effectiveness of immobile traps on reducing swelling[14] and irradiation creep.[15] Rather, it emphasizes the fact that effective trapping requires probably small precipitates or clusters of impurities. Conversely, solutes with low mobility are enhancing void nucleation, and a higher void number density may be obtained, resulting in a lower swelling rate.

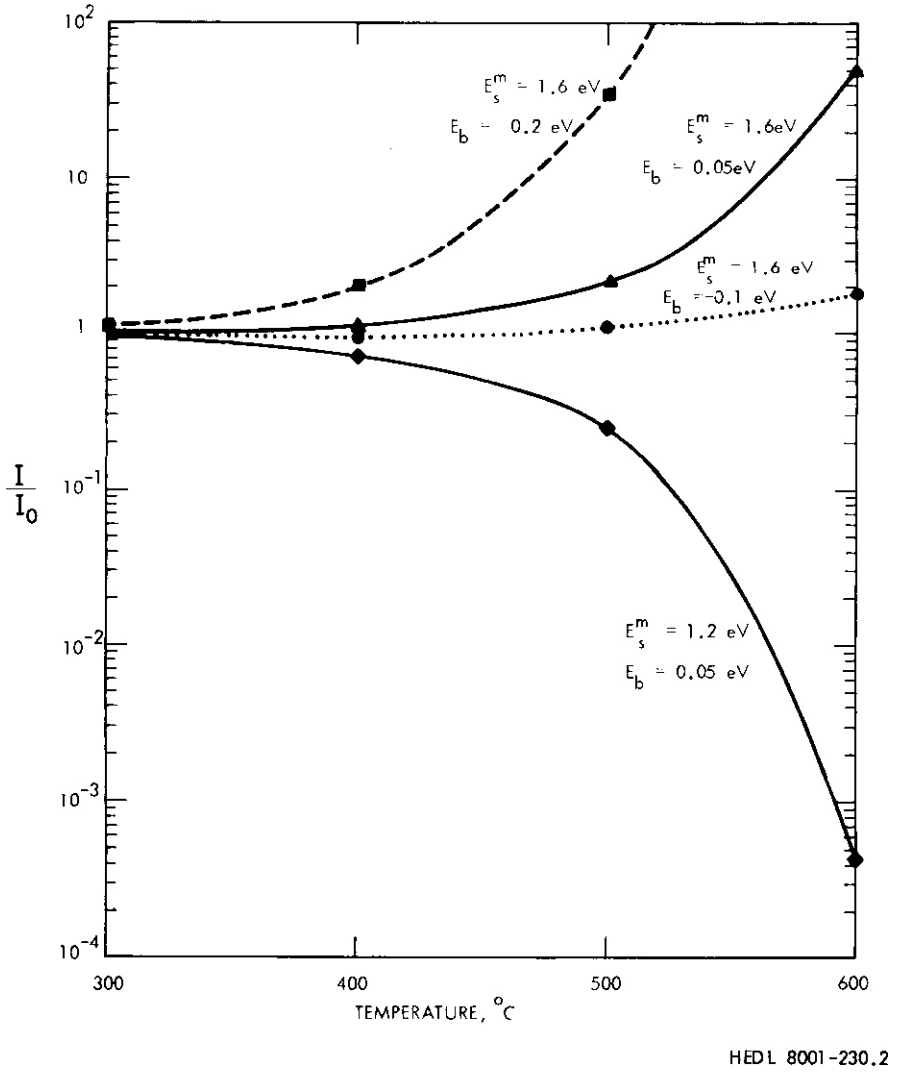

FIGURE 5. Effect on the Relative Void Nucleation Rate of Slow and Fast-Diffusing Solute With 0.1 at.% Concentration.

The interaction of a vacancy with a substitutional solute atom may be repulsive rather than attractive, in which case E_b is negative. This possibility may particularly exist with slow-diffusing solute additions. Therefore, such a case was considered wherein E_s^m = 1.6 eV and E_b = -0.1 eV. The repulsive interaction of a vacancy and a solute offsets the contribution of the solutes to the effective vacancy mobility, and void nucleation is not affected much (as also shown in Figure 5).

4. Discussion

Silicon As a Fast-Diffusing Species in AISI 316: An Assessment

The above calculations demonstrate that the addition of a fast-diffusing substitutional element can have a substantial effect on void nucleation even at very low concentrations. The effect does not require binding to occur, exhibits a saturation behavior with increasing solute, and the relative suppression can vary over the temperature range. The important question to answer is whether this proposed mechanism is one of the dominant mechanisms by which impurities influence void growth in AISI 316.

In thermal environments, silicon is thought to migrate in nickel by vacancy exchange mechanisms, as evidenced[16] by its activation energy for diffusion (61.7 Kcal/gram atom).[16] It has also been shown that the addition of silicon leads to a reduction in void number density in 316 stainless steel at low displacement levels in both neutron and electron irradiations. Other alloys also show a suppression of void nucleation with silicon. Since its diffusivity is from two to three orders of magnitude greater than that of nickel, silicon appears to be an excellent example of the fast-diffusing solute[16]

There is, however, some tendency in the radiation effects community to view the fast-diffusion model as being in opposition to another postulated mechanism, that of solute drag by formation of bound

interstitials. This latter mechanisms involves the formation of di-interstitial complexes with the smaller atoms of the lattice, lowering the effective interstitial diffusion coefficient.[17] Silicon is indeed one of the smaller atoms in austenitic alloys and there is substantial evidence that solute drag effects occur. The segregation of silicon to various sinks is often cited as evidence of solute-drag effects since silicon could migrate with interstitials, while it would migrate away from the net vacancy flow. Segregation of silicon at sinks cannot be considered prima facie evidence for solute drag effects as the only operative mechanism, however. Wolfer[18] notes that all sinks have preferences for interstitials over vacancies and the growth of voids results only from dislocations having higher preferences for interstitials than do voids. It should be noted, however, that the net flow of interstitials over vacancies is very small for all sinks, and the enhanced diffusivity of unbound silicon would eventually result in its sampling all lattice sites. The segregation of silicon might therefore result from random migration to sinks at which the free energy of silicon is lowered. Segregation would also result if there were vacancy-solute binding.[19]

There is one type of evidence which argues very convincingly that solute drag effects operate on the silicon atoms.[20] Silicon is known to migrate to specimen surfaces during irradiation and form silicon-rich phases. If the irradiation ceases while the temperature is maintained the silicon-rich phases almost immediately dissolve. This means that the free energy state is not lower at this type of sink and the silicon must have been carried or dragged up an otherwise insurmountable energy barrier in order to form such phases.

There is therefore no doubt that solute drag effects exist, but the fast diffusing and solute drag concepts are not necessarily mutually exclusive models. Both theories require that the bound defect concentration is relatively small compared to the total solute level, so direct competition of the two mechanisms would not be a major factor. It is quite likely that a combination of these two mechanisms is operating, and

the combination would alleviate one of the major problems with the solute-binding model. While solute-binding effects could account for segregation at surfaces, exceptionally high binding energies are required to affect void nucleation. In effect, the interstitial would have to become the slowest-moving defect, which requires binding energies ≥ 0.7 eV. Some parameter studies by Okamoto et al.[21] have indicated that at low damage rates (10^{-6} dpa/sec) even a binding energy of interstitials to 0.1% of silicon atoms of 1.5 eV has a negligible effect in increasing vacancy-interstitial recombination. Marwick[22] has shown that even 1% of interstitial traps with binding energy of 1 eV would have a negligible effect on radiation-enhanced diffusion at a damage rate of 10^{-5} dpa/sec. Recent measurements of loop formation during electron irradiation suggest that the silicon-interstitial binding energy is only on the order of 0.26 eV,[23] although the experiment was conducted in a manner which did not take into account possible silicon segregation to foil surfaces.

There are several sets of data which support the combined fast diffusion/interstitial binding model. Several researchers have observed silicon depletion in the irradiated zone of ion-bombarded specimens, a process which results in silicon enrichment both at the surface and beyond the ion range.[24,25] This would be the inevitable result of solute binding. Solute-vacancy binding would not yield this result.[24] Marwick and Pillar have shown, however, that addition of silicon to nickel reduces the mobility of implanted tracer chromium atoms during ion bombardment.[22] This demonstrates a strong effect of silicon on the vacancy mobility and the subsequent diffusion of other substitutional components. Assassa and Guiraldenq[26] have recently shown that silicon additions to a Fe-16Cr-14Ni alloy increases the frequency factors for diffusion of all three solvent atoms, which also signals silicon's influence on vacancy diffusion.

Fast Diffusion by Solvent Atoms: An Assessment

Nickel is the slowest diffusing component of Fe-Ni-Cr ternary alloys. It also has the smallest partial molar volume of Fe-Ni-Cr-Si[27]

alloys so that one would expect nickel to concentrate at sinks by both nickel-interstitial binding effects and by preferential out-migration of faster diffusing Fe and Cr atoms. Such behavior would be consistent with the coprecipitation of nickel and silicon observed in bulk material[1-3] if the coprecipitation were occurring on microstructural sinks. At external surfaces, however, the situation is not quite so clear. Nickel has been observed to be depleted at surfaces in 71Fe-15Cr-14Ni[22] during ion bombardment, but accumulated at surfaces in 73Fe-18Cr-8Ni-1Si.[17] The differences in nickel behavior may represent slower segregation phenomena involving ordered phases such as Ni_3Fe. In any event the fast-diffusion effect involving solvent atoms would be expected to be slower than that involving silicon. This may explain why an irradiation-induced phase such as γ' in 316 stainless steel requires thousands of hours to form.[1]

There does appear to be some relationship between solute and solvent migration however. Not only do silicon and nickel coprecipitate under irradiation but the addition of silicon changes the ratios of diffusivities of the various solvent atoms in thermal diffusion studies at 1334°C.[28] These authors showed that the fast diffusion effect is not a viable mechanism for solvent atoms in Fe-Ni-Cr alloys.

As will be shown in later reports the role of nickel appears not to be associated with a large direct effect on bulk diffusion behavior, but in its effect on sink preferences for point defects.

VI. REFERENCES

1. H. R. Brager and F. A. Garner, "Swelling as a Consequence of Gamma Prime (γ') and $M_{23}(C,Si)_6$ Formation in Neutron Irradiated 316 Stainless Steel," J. Nucl. Mat., 73 (1973) pp. 9-19.

2. H. R. Brager and F. A. Garner, "The Influence of Preirradiation Thermal Mechanical Treatment on Phase Stability and Swelling in 316 Stainless Steel," Trans. ANS (1978) p. 151.

3. H. R. Brager and F. A. Garner, "Dependence of Void Formation on Phase Stability in Neutron-Irradiated Type 316 Stainless Steel," in Proceedings ASTM Symposium on Effects of Radiation on Structural Materials, July 10, 1978, Richland, Washington.

4. H. Venker and K. Ehrlich, J. Nucl. Mat. 60 (1976) p. 374.

5. H. Venker, P. Giesecke and K. Ehrlich, "The Influence of Fast Diffusing Substitutional Elements on the Swelling Behavior of Ni and Cu Alloys," in Proceedings of International Conference on Radiation Effects in Breeder Reactor Structural Materials, June 19-23, 1977, Scottsdale, Arizona, p. 415.

6. See review by L. K. Mansur, J. Nucl. Mat. 83 (1979) p. 109.

7. J. Burke, J. Less-Common Metals 28 (1972) p. 441.

8. N. L. Peterson, Solid State Physics 22 (1968) p. 409.

9. R. E. Howard and A. B. Lidiard, Phil. Mag. 11 (1965) p. 1179.

10. C. P. Flynn, Phil. Mag. 10 (1964) p. 909.

11. J. L. Katz and H. Widersich, J. Chem. Physics 55 (1971) p. 1414.

12. W. G. Wolfer and M. H. Yoo in "Radiation Effects and Tritium Technology for Fusion Reactors," CONF-750989.

13. W. G. Wolfer, L. K. Mansur and J. F. Sprague, "Theory of Swelling and Irradiation Creep," Ibid., Reference 5, p. 841.

14. L. K. Mansur and M. H. Yoo, J. Nucl. Mat. 74 (1978) p. 73.

15. L. K. Mansur and W. G. Wolfer, Ibid., Reference 3.

16. R. A. Swalin, A. Martin and R. Olsen, Trans. AIME (1957) p. 936.

17. P. Okamoto and H. Wiedersich, J. Nucl. Mat. 53 (1974) p. 336.

18. W. G. Wolfer, M. Ashkin and A. Boltax, "Creep and Swelling Deformation in Structural Materials During Fast Neutron Irradiation," ASTM STP 570, p. 233.

19. R. A. Johnston and N. Q. Lam, J. Nucl. Mat. 69 (1978) pp. 424-433.

20. L. E. Rehn, P. R. Okamoto, D. I. Potter and H. Wiedersich, "Radiation-Induced Segregation Nickel-Silicon Alloys," Ibid., Reference 3.

21. P. Okamoto, N. Q. Lam and H. Wiedersich, in Proceedings of the Workshop on Correlation of Neutron and Charged Particle Damage, ORNL 760673 (1976).

22. Contribution by A. D. Warwick to ND-M-75(S), "Factor Affecting Void Swelling in Fe-Cr-Ni Alloys," compiled by J. S. Watkin (September 1977) p. 8.

23. M. K. Hossain and L. M. Brown, Radiation Effects, Volume 31 (1977) pp. 203-211.

24. N. Q. Lam, P. R. Okamoto and R. A. Johnston, "Solute Segregation and Precipitation Under Heavy Ion Bombardment," accepted for publication in J. Nucl. Mat.

25. R. C. Pillar and A. D. Marwick, J. Nucl. Mat. 71 (1978) pp. 309-313.

26. W. Assassa and P. Guiraldenq, Metal Sciences (march 1973) p. 123.

27. J. L. Straalsund and J. F. Bates, Met. Trans. 5 (1974) p. 1493.

28. S. J. Rothman, L. J. Nowicki and G. E. Murch, "Tracer Diffusion of Cr, Ni and Fe in Austenitic Fe-Cr-Ni Alloys," presented at Fall AIME Meeting, St. Louis, Missouri, October 15-19, 1978.

VII. FUTURE WORK

Modeling on the compositional dependence of various radiation-induced property changes will continue, as well as the application of these models to the development of fission-fusion correlations.

VIII. PUBLICATIONS

A somewhat expanded version of this report is intended for submission to Journal of Nuclear Materials.

I. PROGRAM

Title: Irradiation Response of Materials

Principal Investigators: S. Wood, J. A. Spitznagel and W. J. Choyke
Affiliation: Westinghouse Research and Development Center

II. OBJECTIVE

The objective of this work is to assess the phenomenology and mechanisms of microstructural evolution in materials exposed to simultaneous helium injection and creation of atomic displacement damage by a second ion beam.

III. RELEVANT DAFS PROGRAM TASK/SUBTASK

SUBTASK II.C.l, II.C.2, II.C.3, II.C.5, II.C.9, II.C.18

IV. SUMMARY

Dual ion irradiation experiments on SA 316 and 20% C.R. 316 SS were conducted over a wide range of damage rates, helium injection rates and ambient oxygen partial pressures. It is concluded that the rapid cavity growth regime observed in SA 316 at 600°C is independent of the ambient oxygen partial pressure. Atomic displacement and helium injection rate mapping of the rapid cavity growth regime over 2-3 orders of magnitude variation in rates is shown to be possible. Experimentally determined maximum equilibrium bubble sizes and "upper bound" theoretical critical cavity sizes for a transition from gas-driven bubble growth to bias-driven void growth are shown to be in reasonable agreement.

V. ACCOMPLISHMENTS AND STATUS

A. Simultaneous Irradiation Experiments in Controlled Oxygen Atmospheres

Simultaneous implantation of helium and bombardment with the heavy ion, Si^{+6}, beam may result in very rapid cavity growth at 600°C in solution annealed 316 SS, as discussed in earlier reports.[1,2] However, additional experiments showed[2] that specimens irradiated at somewhat higher damage rates ($\geq 1.7 \times 10^{-4}$ dpa/s) and in a better vacuum (lower O_2 partial pressure) did not reveal the explosive growth phenomenon. Thus, in order to separate damage rate and oxygen partial pressure effects, a small matrix of samples were dually irradiated for the nominal conditions given in Table I: two partial pressures of oxygen and three damage rates were utilized. A change in damage rate at constant section depth was effected by changing the Si^{+6} beam current and irradiation time. As usual, the He beam was tailored to match the *Si* $S_D(x)$ curve and the He current was also adjusted to yield a fixed He level ($\sim$ 18 appm) for all specimens at the section depth investigated.

The oxygen partial pressure was controlled by adding a Granville-Phillips variable leak valve to the simultaneous implantation furnace chamber. The conductance of this valve is continuously variable from 0.4 liters/sec to 10^{-11} liters/sec, thereby allowing a wide range of system pressures to be accurately maintained. Measurements of these pressures were obtained using a Bayard-Alpert ionization gauge and applying a gauge correction factor for oxygen. As a final check, the composition of the gas in the vicinity of the sample was examined using the Extranuclear Laboratory residual gas analyzer.[3] The only ions observed using this instrument were O^+ and O_2^+ indicating an essentially pure oxygen atmosphere near the sample surface. As given in Table I, the two oxygen partial pressures selected were 6.7×10^{-4} and 6.7×10^{-6} Pa, respectively, and the damage rates were chosen to encompass those utilized in previous experiments showing the explosive growth effect.

TABLE 1. EXPERIMENTAL PARAMETERS USED TO DETERMINE THE EFFECT OF OXYGEN PARTIAL PRESSURE ON MICROSTRUCTURE

Oxygen Partial Pressure, Pa	Damage Rate, dpa/s (Helium injection rate appm/s)*		
6.7×10^{-4}	2.0×10^{-4} (1.6×10^{-3})	1.3×10^{-4} (8.4×10^{-4})	5.5×10^{-5} (4.0×10^{-4})
6.7×10^{-6}	2.3×10^{-4} (1.1×10^{-3})	1.1×10^{-4} (7.6×10^{-4})	5.7×10^{-5} (3.9×10^{-4})

* He rates are bracketed below the damage rates.

Representative cavity microstructures from 4 of the samples are shown in Fig. 1, all at fluences ∿ 2.5 dpa. (Note that the micrographs in Figs. 1a and 1c reflect an inhomogeneous thinning of the specimens.) Comparison revealed that, for all three damage rates (and, therefore, helium injection rates), the microstructures produced in the different oxygen atmospheres are very similar and exhibit only minor differences. Certainly, the oxygen partial pressure was not a major influence in the development of high swelling. Of the 6 specimens investigated, the only 2 which exhibited a profusion of large cavities were those irradiated at the highest damage and helium injection rates (Figs. 1a and 1b). Those bombarded at the intermediate rates (not shown) had microstructures very similar to those shown in Figs. 1c and 1d, with a relatively small number density of voids, often associated with acicular precipitates. These precipitates were not observed in the high rate samples, but there are particles with a more blocky morphology present in both. An additional feature in the samples presented in Figs. 1c and 1d is the presence of numerous small (∿ 20Å) bubbles nucleated along the acicular precipitates. Since the specimen irradiated at the lower oxygen $pp0_2$ has a higher density of precipitates, it appears to have a higher bubble density. Dislocation structures were also more rate than oxygen pressure dependent, showing an increase in faulted loops with decreasing damage rate for both partial pressures of oxygen. Quantification of both void and dislocation densities is still in progress.

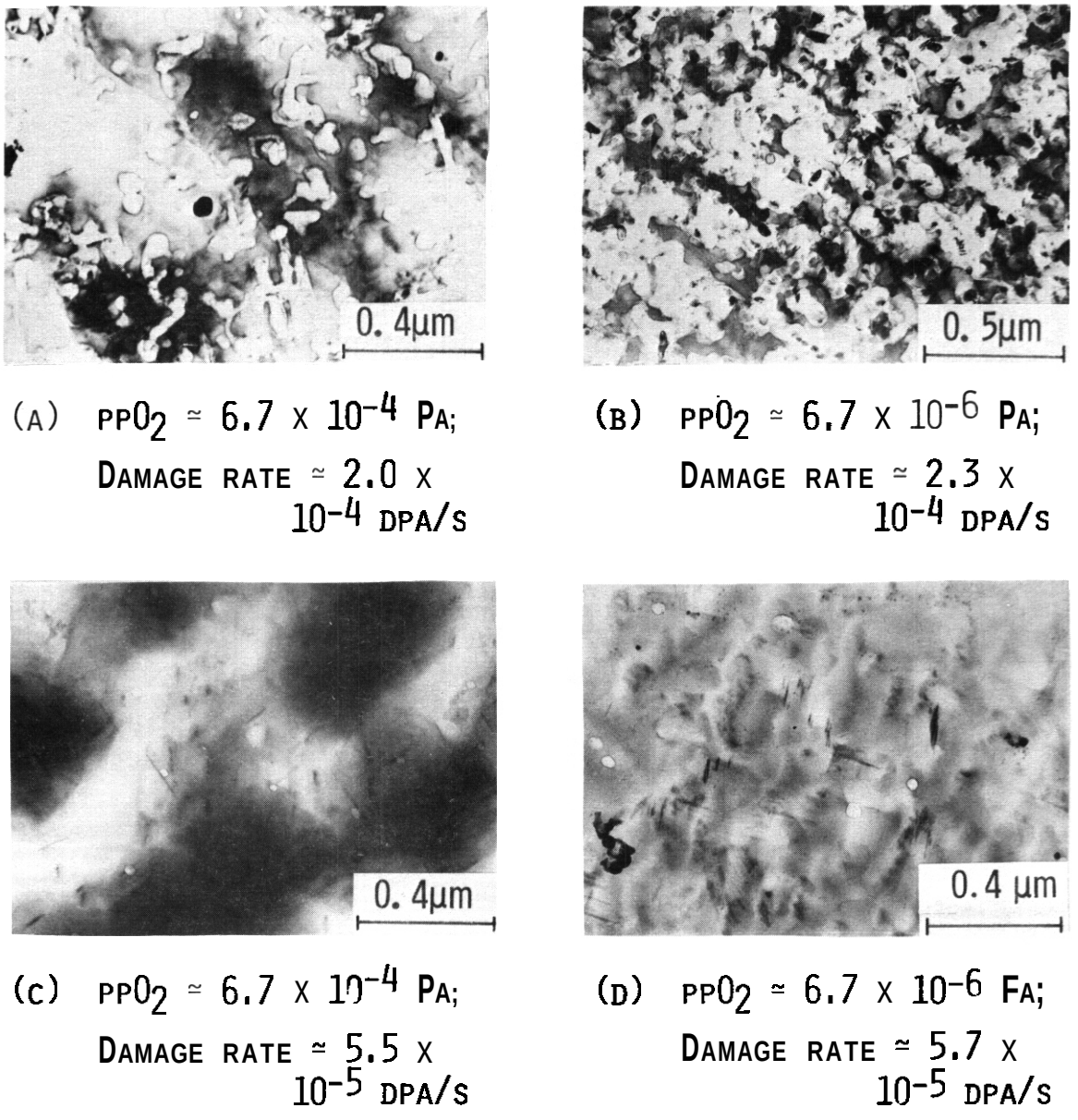

(A) $P_{PO_2} \simeq 6.7 \times 10^{-4}$ PA; DAMAGE RATE $\simeq 2.0 \times 10^{-4}$ DPA/S

(B) $P_{PO_2} \simeq 6.7 \times 10^{-6}$ PA; DAMAGE RATE $\simeq 2.3 \times 10^{-4}$ DPA/S

(C) $P_{PO_2} \simeq 6.7 \times 10^{-4}$ PA; DAMAGE RATE $\simeq 5.5 \times 10^{-5}$ DPA/S

(D) $P_{PO_2} \simeq 6.7 \times 10^{-6}$ FA; DAMAGE RATE $\simeq 5.7 \times 10^{-5}$ DPA/S

FIGURE 1. Cavity Microstructures Produced By Simultaneously Bombarding SA 316 SS With He and Si^{+6} at 600°C in Different O_2 Partial Pressures.

Thus, these results suggest that the explosive cavity growth regime is not a function of the oxygen pressure, but is dependent on both damage and helium injection rates. This observation is in good agreement with additional experiments designed to delineate the boundaries of the regime which are discussed further in the next section.

B. Rapid Cavity Growth in Simultaneously Bombarded 316 SS at 600°C

The occurrence of the high swelling phenomenon in SA 316 SS simultaneously bombarded with Si^{+6} and lie at 600°C has been discussed in some detail previously.[1,2] It has been observed that the high cavity growth regime appears to be very dependent upon both damage rate and helium injection rate, and thus, attempts are currently underway to map out the specific values for which this severely detrimental microstructural effect is observed. Designing and performing dual beam experiments for which the Si^{+6} beam current can be accurately controlled and kept constant at the specimen (within ± 10%) over a range of values (0.3 - 3 μA) only became possible after the introduction of new experimental modifications. Firstly, the carbon stripping foils have been much improved, and secondly, a thermoelectric cooling device has been added to the Cs boiler in the Universal Negative Ion Source. Improved carbon foils permit excellent beam stability, even at the higher beam currents, and the cooling device allows achievement of very low (10^{-6} - 10^{-5} dpa/s) damage rates.

Figure 2 documents the experimental observations to date. The data strongly suggest that there are specific ranges of damage and helium injection rates for which rapid cavity growth occurs, and that outside these ranges, it is not induced. At present, the data define part of the boundary *of* the regime and show where the phenomenon has been observed but do not extend significantly into the region of "no rapid cavity growth." It is assumed that, for example, a damage rate of ∿ 2.5 x 10^{-4} dpa/s at a helium injection rate of ∿ 1.5 x 10^{-3} appm/s is the boundary between rapid and more "normal" cavity growth. It is not, however, accurate to say that high helium levels independently suppress the phenomenon since the occurrence is also interdependent on damage rate.

A complete mapping of the "growth/no growth" boundary may not be possible because of several experimental factors. Firstly, at this fluence (2-5 dpa), data at damage rates > 2.5 x 10^{-4} dpa/s are difficult

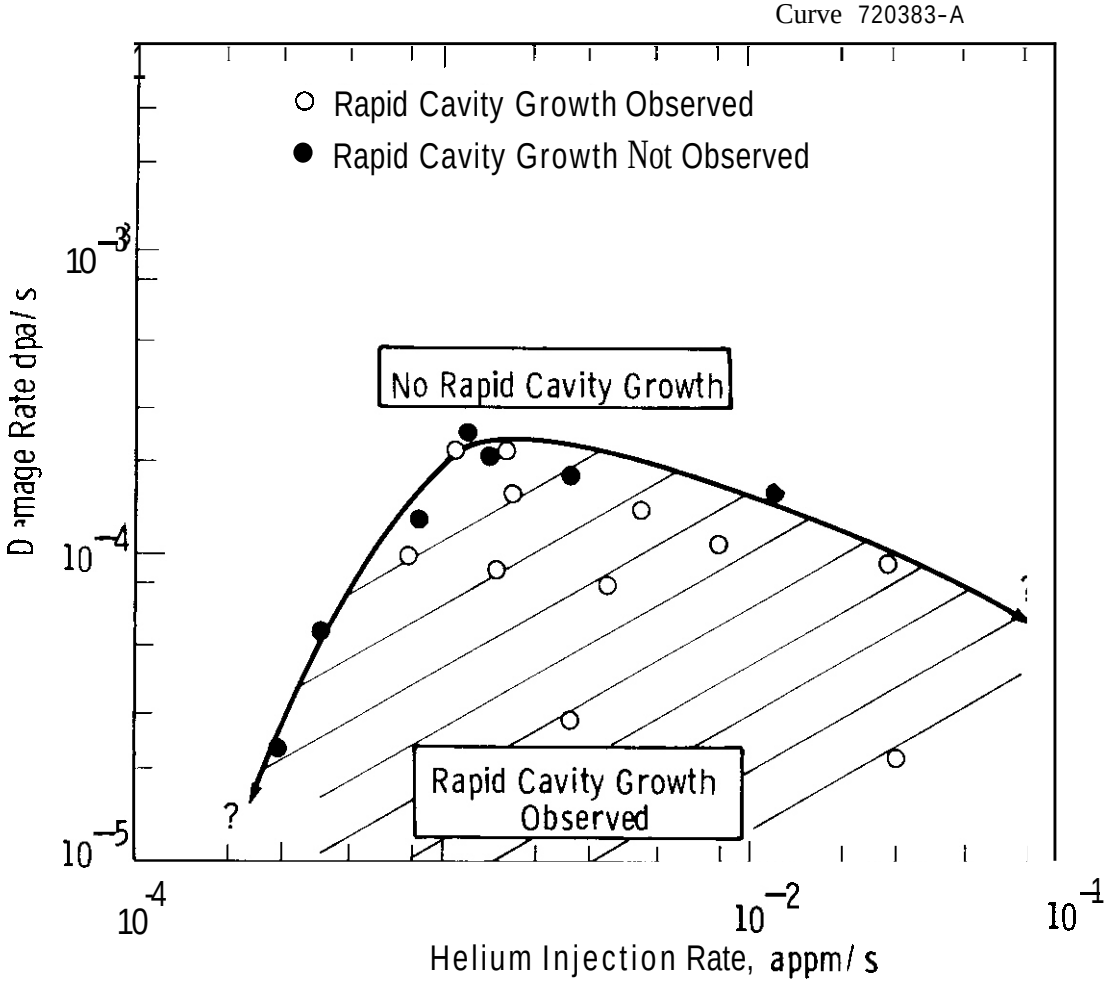

FIGURE 2. Observation of Rapid Cavity Growth in SA 316 SS Simultaneously Irradiated with He and Si^{+6} at 600°C to 2-5 dpa.

to obtain because of beam current limitations. Also, at high helium injection rates, the damage incurred by the helium beam becomes a significant fraction of the total dpa. For example, for the specimen irradiated at 2.2×10^{-5} dpa/s and 3×10^{-2} appm He/s, $\sim$ 30% of the damage may be incurred by the He beam. These problems suggest that the most fruitful area for future experiments will utilize low damage rates and low helium injection rates.

The high swelling observed in SA 316 SS at 600°C is often accompanied by cavity alignment and acicular precipitate formation which prompted the suggestion that the explosive growth phenomenon is directly linked to solute segregation.[2] In any event, the rapid cavity growth is obviously the result of a delicate balance between atomic displacement rate, helium injection rate and irradiation temperature. A more detailed analysis of the data presented in Fig. 2 is still in progress. In particular, it is not fully understood why the high swelling is suppressed at high damage and helium injection rates, although an independent study in 304 SS has shown that high helium levels inhibit acicular precipitate formation.[4] Suppression may occur at low damage rates because of a reduction in the defect flux, but present data unfortunately suggest that the rates characteristic of projected fusion reactor first wall conditions favor the anomalous cavity growth regime.

C. Experimental Determination of the Maximum Equilibrium Bubble Size in 316 SS and Comparison with the Theoretically Predicted Critical Cavity Size for the Transition from Gas-Driven to Bias-Driven Growth

Helium mobility, bubble nucleation and growth rates and the microstructural conditions leading to rapid bias-driven cavity growth from a population of bubbles are not known. Such information is essential for understanding helium effects in first wall and blanket elements under projected fusion reactor conditions. In addition, such information is necessary for intelligent planning and modeling of high energy neutron

source and mixed-spectrum fission reactor experiments on microstructural and mechanical property changes at high (and variable) helium to dpa ratios. Dual ion irradiation experiments are well suited for the determination of these quantities because of the precision with which damage rate, helium injection rate and temperature can be controlled. In this section we discuss some recent results of conducting computerized "helium inventory" calculations on experimentally measured cavity size distributions. The results are compared with theoretically predicted "critical cavity" sizes over a range of temperatures.

In an earlier report[2] we described the construction of computerized data files which facilitate rapid retrieval of dual ion irradiation data, and a code which permits queries to delineate parametric sensitivity of cavity, dislocation loop and precipitate size distributions. The code can quickly scan data from hundreds of dual-ion runs; select the data sets from the files which satisfy imposed criteria (e.g., a specified combination of irradiation temperature, damage rate, appm He/dpa level, etc.); calculate the desired statistics (moments of size distribution, etc.); and plot (calcomp) the statistics versus a specified irradiation parameter.

In this quarter, the file system and computer code were used to determine the maximum possible equilibrium bubble diameter, D_c, for solution annealed and 20% cold worked targets of 316 SS bombarded simultaneously with 2 MeV helium and 28 MeV Si^{+6} over a range of temperatures. Additional criteria were imposed with respect to damage rate (5.4×10^{-5} dpa/s to 2×10^{-4} dpa/s), helium injection rate (7×10^{-4} appm/s to 3×10^{-3} appm/s) and dpa level (1.4 - 5.0 dpa). Targets satisfying the criteria had all been bombarded at appm He/dpa ratios of $\sim$ 7-13.

To obtain the maximum equilibrium bubble diameter (D_c) for samples satisfying the imposed criteria, the files were searched for the relevant cavity size distributions. A "helium inventory" calculation was then performed for each size class in a given distribution. This was accomplished

by having the code start with the smallest observed cavity size and calculate and sum the number of helium atoms in each size class using the Van der Waals equation of state and surface energies obtained from extrapolations of "zero creep" data as described elsewhere.(5) In performing the summation it is assumed that cavities larger than the maximum equilibrium bubble size must have passed through that size in their growth and thus contain the same number of helium atoms as the largest equilibrium bubbles. When the helium concentration summed over the size classes equals the implanted concentration the code designates the last size class filled with helium as D_c. Clearly D_c is an upper estimate of the true maximum bubble diameter because additional He atoms in submicroscopic bubbles and helium in large cavities with $D > D_c$ cannot be accurately "inventoried" using only TEM micrographs.

Figure 3 shows the temperature dependence of D_c for solution annealed and 20% cold worked targets of 316 SS satisfying the imposed atomic displacement and helium doping conditions. At temperatures above 700°C D_c increases rapidly. At all temperatures the maximum equilibrium bubble size is identical for both solution annealed and cold worked material within the uncertainty of the measurements and calculations. In all of the cavity size distributions studied, D_c is smaller than the largest cavity diameter. For all but one sample, D_c is larger than the average cavity diameter. This indicates that the damage rate and microstructural sink strengths are adequate to permit some cavities to grow larger than the equilibrium bubble size by bias-driven growth at all temperatures from 550 to 750°C. The parameter D_c is thus related to the theoretically predicted "critical cavity radius" (r_c^c) for the transition from gas-driven bubble growth to bias-driven void growth.(6)

Wood et. al.(6) have derived a simple analytical approximation for r_c^c by ignoring both recombination and the interactive terms in the calculation of cavity sink strengths. They thus obtain an "upper bound" estimate to the critical size given by:

$$r_c^c = 2\gamma D_s^v Z_i Z_v \rho_D \Omega/(Z_i - Z_v) K kt$$

where D_s^v = self diffusion coefficient
K = damage rate
D = dislocation density
γ = surface energy
Z_i, Z_v = dislocation bias factor for interstitials and vacancies, respectively
Ω = atomic volume
k = Boltzmann's constant
T = absolute temperature in °K

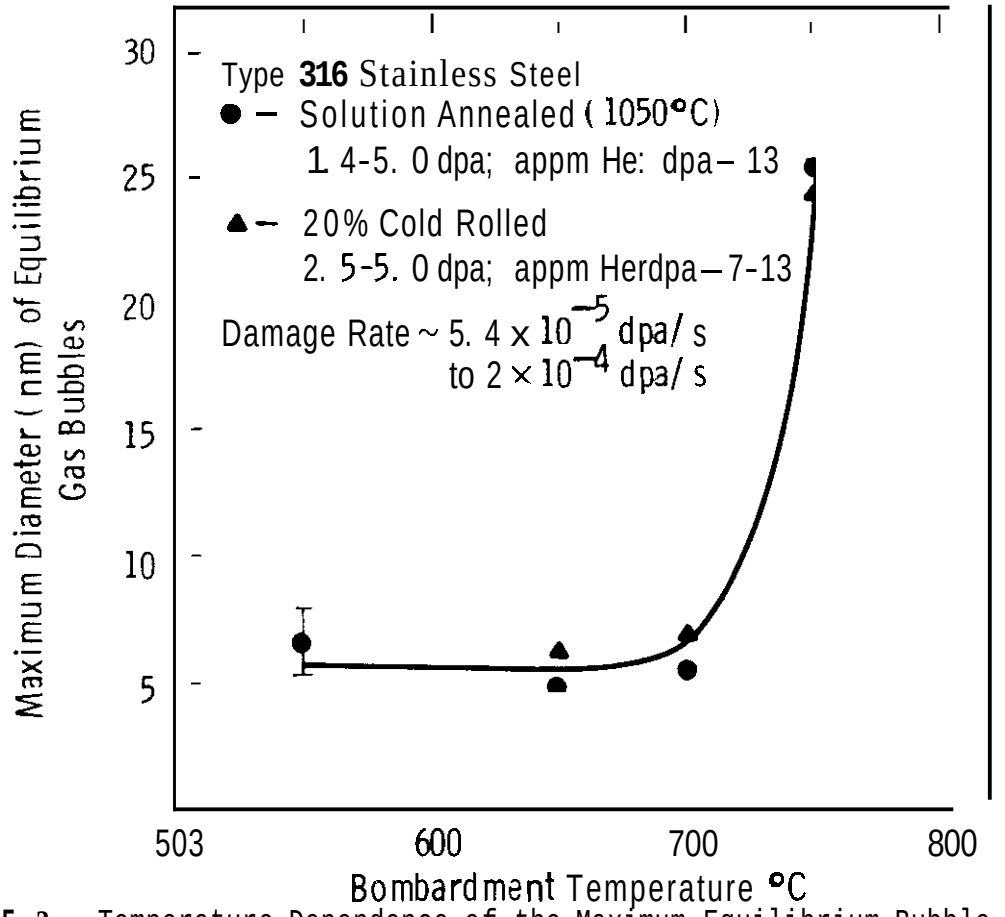

FIGURE 3. Temperature Dependence of the Maximum Equilibrium Bubble Size Calculated from Experimentally Determined Cavity Size Distributions in Dual-Ion Bombarded 316 SS. Calculations performed with the Irwin code using the helium inventory method.[1]

Table 2 summarizes results of the calculations of D_c from the experimentally measured cavity size distributions and $2 r_c^c$ calculated using the Wood et. al. equation. Both D_c and $2 r_c^c$ exhibit a strong variation with temperature and generally agree within an order of magnitude. This is reasonable agreement considering the uncertainties in the experimental measurements and approximations in the model calculations. Better comparisons of D_c and $2 r_c^c$ will be forthcoming through the use of (a) the full rate theory model; (b) studies of the dose-dependence of cavity evolution to observe the development of a bi-modal population; and (c) temperature change experiments.

TABLE 2. COMPARISON OF MAXIMUM EQUILIBRIUM BUBBLE SIZE (D_c) AND THEORETICALLY PREDICTED CRITICAL CAVITY SIZE ($2 r_c^c$) FOR THE TRANSITION FROM GAS-DRIVEN TO BIAS-DRIVEN CAVITY GROWTH

	IRRADIATION TEMPERATURE "C	D_c (nm)	$2 r_c^c$ (nm)
SA 316 SS	550	7	0.2
	650	5	3
	700	6	17
	750	25	28
20% CR 316 SS	600	no visible cavities	
	650	6	20
	700	6	93
	750	24	160

VI. REFERENCES

1. S. Wood, J. A. Spitznagel and W. J. Choyke, OAFS Quarterly Report No. 6, April-June (1979), DOE/ET-0065/6.

2. S. Wood, J. A. Spitznagel and W. J. Choyke, OAFS Quarterly Report No. 7, July-September (1979), DOE/ET-0065/7.

3. J. A. Spitznagel and W. J. Choyke, OAFS Quarterly Report No. 1, January-March (19781, DOE/ET-0065/1.

4. W. J. Choyke, J. N. McGruer, J. R. Townsend, J. A. Spitznagel, N. J. Doyle and F. J. Venskytis, Proceedings of 1st Topical Meeting ON Fusion Reactor Materials, Bal Harbour, FL, Jan. 29-31, 1979, to be published in J. Nucl. Mater. (1980).

5. J. R. Cost and K. Y. Chen, J. Nucl. Mater. *67*, p. ***265*** (1977).

6. M. H. Wood, M. R. Hayns and R. **Bullough**, "The Dependence of Cavity Nucleation Density Upon Gas Implantation Rate and its Importance in Dual Beam Irradiation Conditions," UKAEA Report **AERE-R9099**, May (1978).

VII. FUTURE WORK

Microstructural analysis followed by data computerization will be completed for the 800°C aged 316 SS samples used to study the effects of primary recoil spectra differences under dual ion bombardment. Very low damage rates approaching projected fusion reactor first wall values will be employed in dual ion bombardment of SA 316 SS to further define how low dose microstructural evolution "scales" with instantaneous dpa and He injection rates. Specimens of Ti-modified 316 SS from the same heat of material used in HFIR experiments at ORNL will be subjected to dual-ion bombardment to study plausible mechanisms of He trapping at TiC interfaces.

VIII. PUBLICATIONS

None

I. PROGRAM

Title: Radiation Effects on Fusion Reactor Materials
Principal Investigators: G.L. Kulcinski and P. Wilkes
Affiliation: University of Wisconsin, Madison

II. OBJECTIVE

To develop a fundamental understanding of the formation of voids, loops and precipitates in heavy ion and electron irradiated metals and alloys.

III. RELEVANT DAFS PROGRAM TASK/SUBTASK

Subtask II.C.1.2. Modeling and Analysis of Effects of Materials Parameters on Microstructural

IV. SUMMARY

An investigation of the effects of heavy-ion irradiation on the stability of precipitates and on the redistribution of solute atoms in several Cu-rich binary alloys is in progress. The alloys Cu-.5 wt.% Be, Cu-1 wt.% Co and Cu-1 wt.% Fe, are irradiated at elevated temperatures in the University of Wisconsin Heavy Ion Irradiation Facility with 14 MeV Cu ions. Following irradiation, the alloy microstructure is examined in a 120 KV transmission electron microscope (TEM). Solute concentration profiles near the ion bombarded surface are measured using Auger Electron Spectroscopy combined with sputtering.

For this study a new specimen holder/heater arrangement, which allows individual heating of a specimen during irradiation, has been designed and built. A TEM specimen preparation technique has been developed for the Cu alloys that allows examination of irradiated samples in cross section, along the path of the incident ions. To date, a set of

eight Cu-Be and Cu-Co foils have been irradiated at temperature between 350°C- 475°C, to doses of 0.3 to $3x10^{16}$ ions/cm^2. Analysis of these specimens has not been completed. Copious precipitation was observed in Cu-Be foils irradiated at 400°C, while no precipitation occurred in regions of these foils masked from the ion beam. Surface enrichment of the Be solute (compared to nonirradiated regions of the specimens) was found in most of the Cu-Be foils.

V. ACCOMPLISHMENTS AND STATUS

A. Heavy Ion Irradiation of Copper Alloys - R. W. Knoll

In order to perform high temperature irradiation effects experiments on alloys, it was necessary to redesign the specimen holder/heater assembly in the target chamber of the U.W. Heavy Ion Irradiation Facility. In the previous design,' 8 specimens were mounted on a linear holder, which sat within a cylindrical furnace during irradiation. Specimens were irradiated one at a time. However, they were not thermally isolated from one another, so they were subjected to unwanted pre-irradiation and post-irradiation heating. In the new design, the heater consists of two concentric, cylindrical-sections of tantalum sheet, which subtend an angle of 40°, and which are separated by a small yap. The sheets are heated resistively. The specimens are mounted on a carousel-like holder suspended above the heater. During irradiation, a specimen is rotated into the gap between the heater sheets, and is heated by thermal radiation. The other specimens remain at ambient temperature.

Specimens of a Cu-.5 wt.% Be alloy (3.4 at.% Be) were irradiated with 14 MeV Cu ions at temperatures of 350, 400, 430 and 475°C, to doses of .3 to $3x10^{16}$ ions/cm^2 (4 to 40 peak dpa). Prior to irradiation, the specimens were solution treated at 800°C in an H_2 atmosphere, then quenched. Two samples irradiated at 400°C have been examined in the electron microscope. These specimens were prepared for microscopy using two different thinning methods - a conventional (backthinning) and a cross sectioning method. In the former, about 1 micron was removed from the

irradiated surface of the sample, then the sample was thinned from the reverse side until perforation occurred. This region of the foil (which was subjected to a dose of about 5 dpa) contained many plate-like precipitates, tentatively identified as the γ' CuBe phase. Non-irradiated areas of the specimen contained no precipitates. No voids were observed in the irradiated regions. The second specimen was electroplated with Cu following irradiation, and was then cross sectioned and thinned in the damage region. This cross sectioning technique, which is similar to that used by Whitley[3] in this laboratory to study pure Ni, allows the microstructure to be examined as a function of depth from the irradiated surface (hence a dose-scan can be obtained from a single specimen). As shown in Figure 1, precipitation occurred in the damage region, extending nearly to the end of range of the incident ions. No precipitates are visible in the unirradiated area. The mechanism responsible for this radiation-induced precipitation has not yet been determined.

Auger electron spectroscopy combined with Ar^+ or Xe^+ sputtering was used to profile the near-surface Be concentration in Cu-Be specimens irradiated at 350, 430, and 475°C. Measurements were taken on both irradiated and non-irradiated areas of each sample. The Auger transitions that were used occurred at 94 eV (Be), 920 eV (Cu) and 508 eV (O). In agreement with solute segregation theory,[3] the undersized Be solute was found to be enriched near the irradiated surface. A smaller degree of Be enrichment was found near the non-irradiated surfaces, presumably due to equilibrium segregation. The relative concentrations of elements within 70 nm of the irradiated and nonirradiated surfaces of a 475°C sample are plotted in Figure 2. The concentrations were calculated according to the method of Davis, et al.[(4)] A relatively large oxygen concentration, which follows the Be profile, is evident. The oxygen is believed to be introduced as an impurity in the sputtering gas.

The near-surface Co concentration in Cu-1% Co specimens irradiated at 400°C and 475°C with 3×10^{15} ions/cm^2 was also measured using AES. The

magnitude of the 656 eV peak of Co was compared to the 920 eV peak of Cu, as a function of depth from the irradiated surface. No change was observed in the peak heights, so it is concluded that in this temperature range, irradiation does not cause segregation of the Co solute in Cu. This is consistent also with solute segregation theory, since the Co atom in solution with Cu is nearly the same size as the Cu atom.

VI. REFERENCES

1. H.V. Smith and R.G. Lott, Nuc. Inst. Methods, 143 (1977) 125-132.
2. J.B. Whitley, G.L. Kulcinski, P. Wilkes, H.V. Smith, J. Nuc. Mat. (1978).
3. P.R. Okamoto and H. Wiedersich, J. Nuc. Mat. 53 (1974) 336.
4. L.E. David, et al., Handbook of Auger Electron Spectroscopy, Second Ed., Physical Electronic Industries.

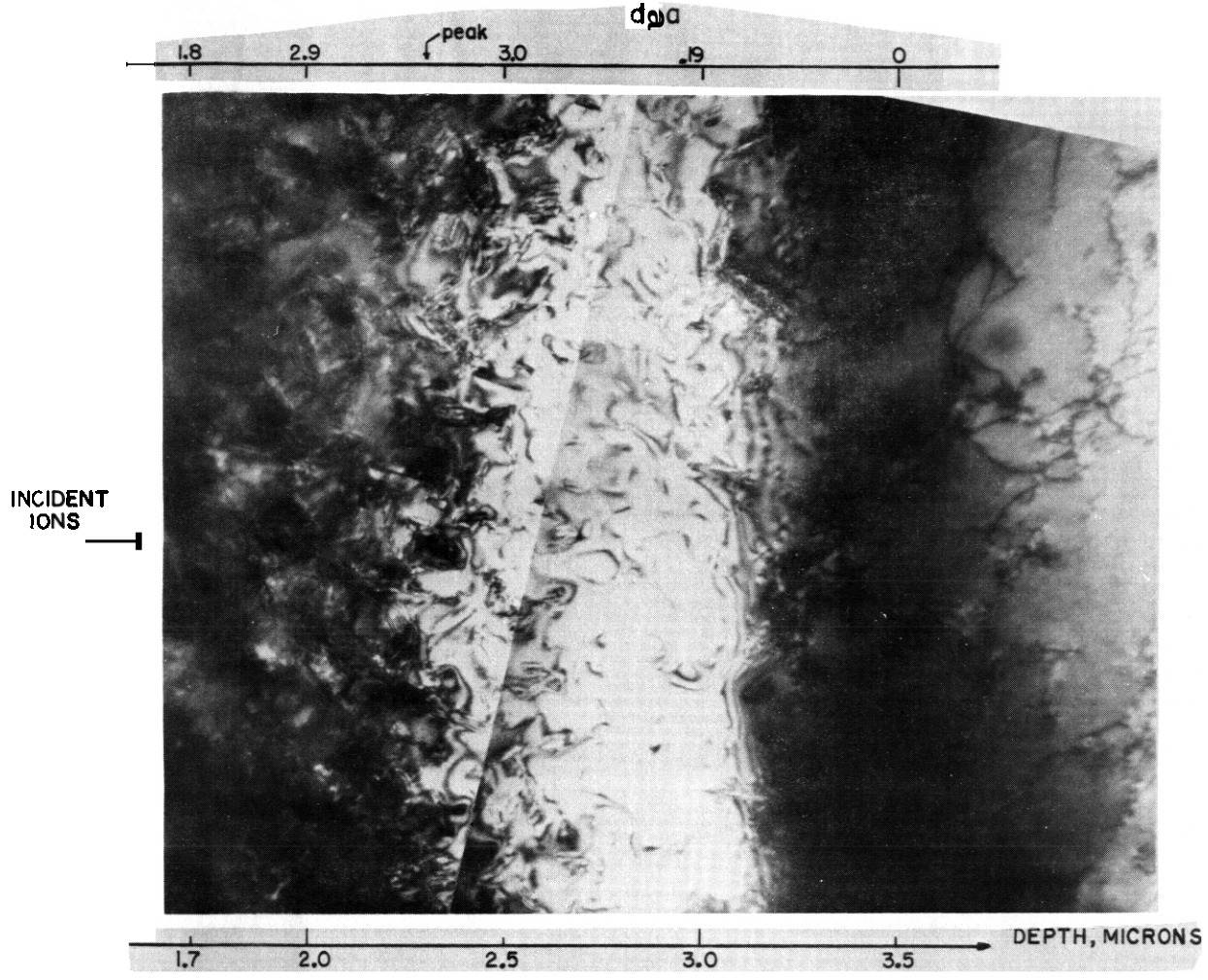

FIGURE 1. Radiation-Induced Precipitation in Heavy Ion Bombarded Cu-3.4 at.%Be, in Cross Section. (14 MeV Cu Ions, 3.2 x $10^{15}/cm^2$, 400°C)

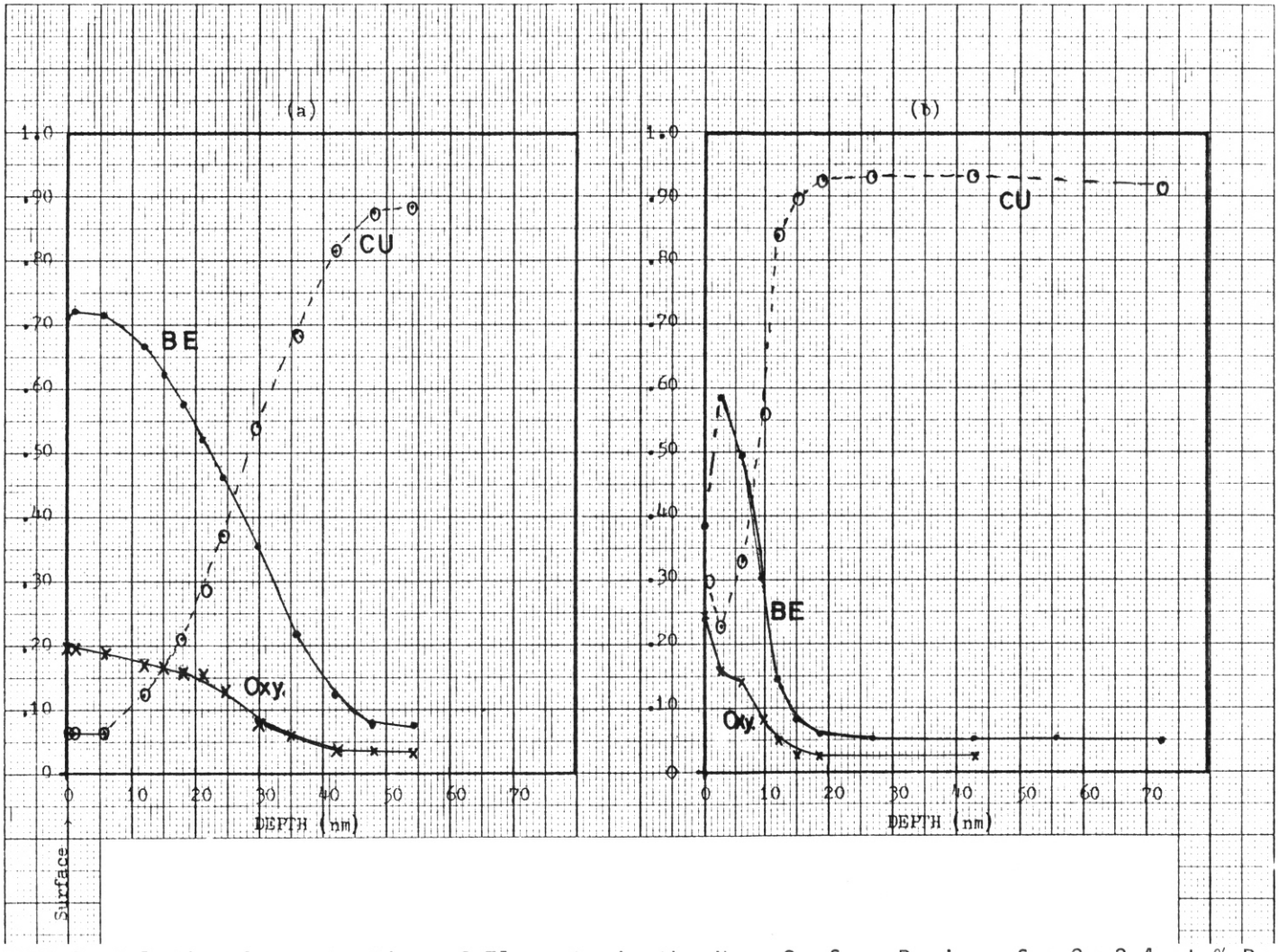

FIGURE 2. Relative Concentration of Elements in the Near-Surface Region of a Cu-3.4 at.% Be Foil. Depth profiles were generated from Auger electron spectroscopy data. a) Irradiated with 3 x 10^{15} Cu Ions/cm^2 @ 475°C; b) A nonirradiated region of the same specimen.

I. PROGRAM

Title: Mechanical Properties
Principal Investigator: R. H. Jones
Affiliation: Pacific Northwest Laboratory
Operated by Battelle Memorial Institute

II. OBJECTIVE

The objective of this program is to study the effects of fusion energy neutrons on the mechanical properties and microstructures of selected metals for the purpose of developing correlations between the displacement damage produced by fusion and fission energy neutrons. The specific objectives of the work described herein are to determine:

- If a hardening plateau exists in titanium and vanadium irradiated with T(d,n) neutrons;
- The effect of oxygen on the hardening plateau in niobium;
- The effect of temperature on the hardening response of titanium, vanadium, and niobium.

III. RELEVANT DAFS PROGRAM PLAN TASK/SUBTASK

II.C.6 Effects of Damage Rate and Cascades on Microstructures
II.C.11 Effects of Cascades and Flux on Flow
II.C.18 Relating Low and High Exposure Microstructures

IV. SUMMARY

Experiments have been planned to establish the effects of T(d,n) neutron irradiation on the tensile properties and microstructures of

titanium, vanadium, and oxygen-doped niobium. The materials for these experiments have been obtained and are currently being prepared for irradiation in the Rotating Target Neutron Source (RTNS)-II.

Preliminary tensile tests of the titanium and vanadium materials indicate reproducible results can be obtained with wire specimens of these materials using the preparation techniques described herein. The tensile properties measured with the wire specimens are similar to reported values obtained with large specimens except the yield strengths of the wire specimens are high.

V. ACCOMPLISHMENTS AND STATUS

High Energy Neutron Studies -- E. R. Bradley and R. H. Jones (PNL)

1. Introduction

An understanding of the effects of high energy neutron irradiation on the mechanical properties of metals is needed for the design and development of fusion reactors. The currently available high energy neutron sources have small irradiation volumes and low neutron fluxes. Thus, a correlation between fusion and fission neutron irradiation induced microstructure and mechanical properties is required so that data from fission neutron irradiations can be confidently used for fusion applications.

Previous results from this program have shown a hardening plateau occurs with increasing fluence in high purity niobium.[1] The height of the hardening plateau and the fluence corresponding to the end of the plateau were dependent upon the irradiating particle, i.e., 16 MeV protons produced greater hardening and the plateau extended to higher fluences than for Be(d,n) neutrons. A similar hardening plateau in niobium single crystals irradiated with fission neutrons has been reported by

Loomis and Gerber.[2] Their results show the height and duration of the hardening plateau to depend on the oxygen content of the niobium. Direct comparison of the hardening responses from the fission and fusion energy neutrons is not possible because of the differences in purity and crystalline state of the niobium used in the two investigations. However, the fluence at the end of the hardening plateau is about an order of magnitude higher for the fission neutrons compared to the Be(d,n) neutrons and, therefore, suggests a significant spectral effect in irradiated niobium.

Experiments have been initiated to determine if a hardening plateau occurs in vanadium and titanium. Also, the temperature dependence of the irradiation induced hardening in niobium, vanadium, and titanium as well as the effect of oxygen on the radiation behavior of these three metals will be studied in these experiments.

2. Irradiation Program

Neutron irradiations during the current fiscal year will be concentrated on T(d,n) neutron irradiations at the RTNS-II. The planned irradiations include both room temperature and elevated temperature irradiations of high purity titanium and vanadium as well as oxygen-doped niobium. Both wire and foil specimens for tensile testing and transmission electron microscopy, respectively, will be included in the irradiation packets.

A total of six room temperature irradiations over the fluence range 5×10^{16} to 2×10^{18} n/cm^2 will be performed to establish if a hardening plateau exists in high purity titanium and vanadium and to establish the effects of oxygen content on the hardening plateau produced in niobium by T(d,n) neutrons. Comparison of the data obtained from these irradiations to the previous results from high purity niobium and nickel will provide information regarding the effects of crystal structure and purity on the irradiation induced hardening and microstructural evolution.

Four elevated temperature irradiations (175°C) are also planned for later in the fiscal year. In addition to the materials used in the room temperature irradiations, high purity niobium wires and foils will also be included in these irradiation packets. The fluence levels for these irradiations will be selected to coincide to those of the room temperature irradiations within the fluence range where a hardening plateau is expected (1×10^{17} to 1×10^{18} n/cm^2). Thus, direct comparisons of the results from the two irradiation temperatures will enable the effects of irradiation temperature on the hardening response and microstructural evolution to be established.

Future irradiations of the same materials with Be(d,n) and fission neutrons will be used to determine the effects of the neutron energy spectra on the radiation induced property changes. The results obtained from the RTNS-II irradiations will guide the planning and scope of these irradiations.

3. Specimen Preparation

The majority of the materials for the initial irradiations are currently available. Titanium and vanadium wire (0.51 mm diameter) and sheet (0.25 mm thick) stock material was obtained from R. W. Powell, Hanford Engineering Development Laboratory (HEOL). The vanadium wire contained many surface defects and laminations which could effect the data from tensile tests of these small diameter wires. Therefore, additional vanadium wire stock is currently being prepared by F. W. Wiffen, Oak Ridge National Laboratory (ORNL). The existing supply of Materials Research Corporation Marz Grade niobium will be used for oxygen doping in order to directly compare the results to the previous data on this material.

The procedures for preparing the titanium and vanadium wires for irradiation have been developed. The as-received wires are cut to the approximate length and vacuum annealed at $\sim 10^{-8}$ torr for one hour.

The individual wires are then straightened by a small amount of plastic deformation in tension, cut to final length, and annealed in vacuum for an additional hour. The annealing temperature for the vanadium was 950°C which produces an equiaxed grain structure with an average grain size of about 25 μm. An average grain size of about 15 μm was produced in the titanium wires when annealed at 650°C. These sizes are sufficiently small to meet the fine grain size requirements for testing the 0.51 mm diameter wires.

Specimens of both the titanium and vanadium wires have been prepared by the above procedures and are ready for irradiation. However, the vanadium wires will not be used if the new wire obtained from ORNL is of better quality.

A vacuum system with a controlled oxygen leak has been designed for oxygen doping the high purity niobium. The components for the system are available and it is currently being assembled.

4. Tensile Testing

A few tensile tests on the titanium and vanadium wires have been conducted. The primary objectives of these tests were to develop the electropolishing conditions for producing the reduced gage section in these materials and establish the optimum testing procedures. The results of these tests show that fairly uniform gage sections can be consistently obtained after the cathode configuration and electropolishing conditions are established. The measured yield strength of the titanium and vanadium were 202 ± 20 MPa and 394 ± 20 MPa, respectively. These values are 25 to 50% higher than reported in the literature for materials with similar grain sizes.[3,4] The higher yield strengths for the wire specimens is thought to be partially associated with the grips used for the testing. These grips were designed for 0.38 mm diameter wires and some bending

occurred during loading the larger diameter wires. New grips are being designed which will minimize deformation during loading and thereby improve the reliability of the data. Also, tests are planned to measure the yield strength as a function of the specimen diameter in these materials and thus, the effects of specimen purity will be minimized.

VI. REFERENCES

1. R. H. Jones, DAFS Quarterly Progress Report, DOE/ET/0065-6, April-June, (1979), 185.

2. B. A. Loomis and S. B. Gerber, "Effect of Oxygen Impurity on Defect Agglomeration and Hardening of Neutron Irradiated Niobium", Acta Met., 33, (1973), 165.

3. R. J. Lederich, S. M. L. Sastry, J. E. O'Neal, and B. B. Rath, "The Effect of Grain Size on Yield Stress and Work Harding of Polycrystalline Titanium at 295K and 575K", Mater. Sci. Eng., 33, (1978), 183.

4. G. H. Keith and D. R. Mathews, "Effects of Interstitial Impurities on Twinning and Low-Temperature Mechanical Properties of Electrorefined Vanadium", Refractory Metals and Alloys IV, AIME Metallurgical Society Conference, Volume 41, (1967), 247.

VII. FUTURE WORK

The specimens for the room temperature irradiations will be prepared, loaded into the irradiation packets, and sent to LLL for RTNS-II irradiation.

New grips for tensile testing the 0.51 mm diameter wire specimens will be designed and fabricated.

VIII. PUBLICATIONS

A paper entitled "Hardening Stages in Niobium Irradiated With Energetic Neutrons and Protons", R. H. Jones, E. R. Bradley and D. L. Styris, was presented at the 1979 Fall AIME Conference, Milwaukee, WI, September 10, 1979.

I. PROGRAM

Title: Irradiation Effects Analysis (AKJ)
Principal Investigator: D. G. Doran
Affiliation: Hanford Engineering Development Laboratory

II OBJECTIVE

The objective of this work is to determine the effects of high energy neutrons on damage production and evolution, and the relationships of these effects to effects produced by fission reactor neutrons. Specific objectives of current work are the planning and performance of an irradiation program at the Rotating Target Neutron Source (RTNS)-II at the Lawrence Livermore Laboratory (LLL) and postirradiation testing.

111. RELEVANT OAFS PROGRAM TASK/SUBTASK

SUBTASK II.B.3.2 Experimental Characterization of Primary Damage State; Studies of Metals

II.C.6.3 Effects of Damage Rate and Cascade Structure on Microstructure; Low-Energy/High-Energy Neutron Correlations

II.C.11.4 Effects of Cascades and Flux on Flow; High-Energy Neutron Irradiations

II.C.17.1 Microstructural Characterization; Monitor and Assess New Methodologies

II.C.18.1 Relating Low- and High-Exposure Microstructures; Nucleation Experiments

IV. SUMMARY

The dosimetry from the HEDL-2 irradiation shows a maximum fluence of 1.19 x 10^{18} n/cm^2 and a spatial variation that is consistent with a beam diameter of about 1 cm. The high vacuum furnace designed and fabricated

at HEDL has been received and assembled at RTNS-II.

V. ACCOMPLISHMENTS AND STATUS

A. RTNS-II Irradiation Program - N. F. Panayotou (HEDL)

1. Specimen Preparation

Marz grade Fe foil has been obtained for the RTNS-II metal stockpile. Procurement of other forms of the same heat of Fe is in progress.

2. Status of Irradiations

The irradiation of HEDL's fourth capsule has been delayed until mid-January due to equipment problems at the RTNS-II facility. A new irradiation capsule (see Figure 1) will be employed which allows for simultaneous irradiation of wire and disk specimens. The results from postirradiation tensile tests on the wire specimen will be correlated with data obtained from the microhardness testing of disk specimens.

Dosimetry results have been received from LLL for HEDL's second irradiation. Some of the Nb dosimetry data are displayed in Figure 2 in order to demonstrate the dosimetry coverage. As the source characteristics become better known, it should be possible to reduce the number of foils. The absolute uncertainty is believed to be less than 10%; the relative uncertainties, due primarily to the need for interpolation, are less than 3%. The peak fluence at a specimen location was 1.19×10^{18} n/cm^2. The minimum fluence was lower by a factor of 25. This is close to the factor of 30 estimated using the assumed flux distribution for a fixed 1 cm source; it compares with the value of 15 obtained in HEDL's first experiment. The new beam steering technique which was in place for HEDL-2 appears to have improved the long-term stability of the beam position. However, the peak fluence was not obtained on the capsule axis, but was displaced by about 3 mm.

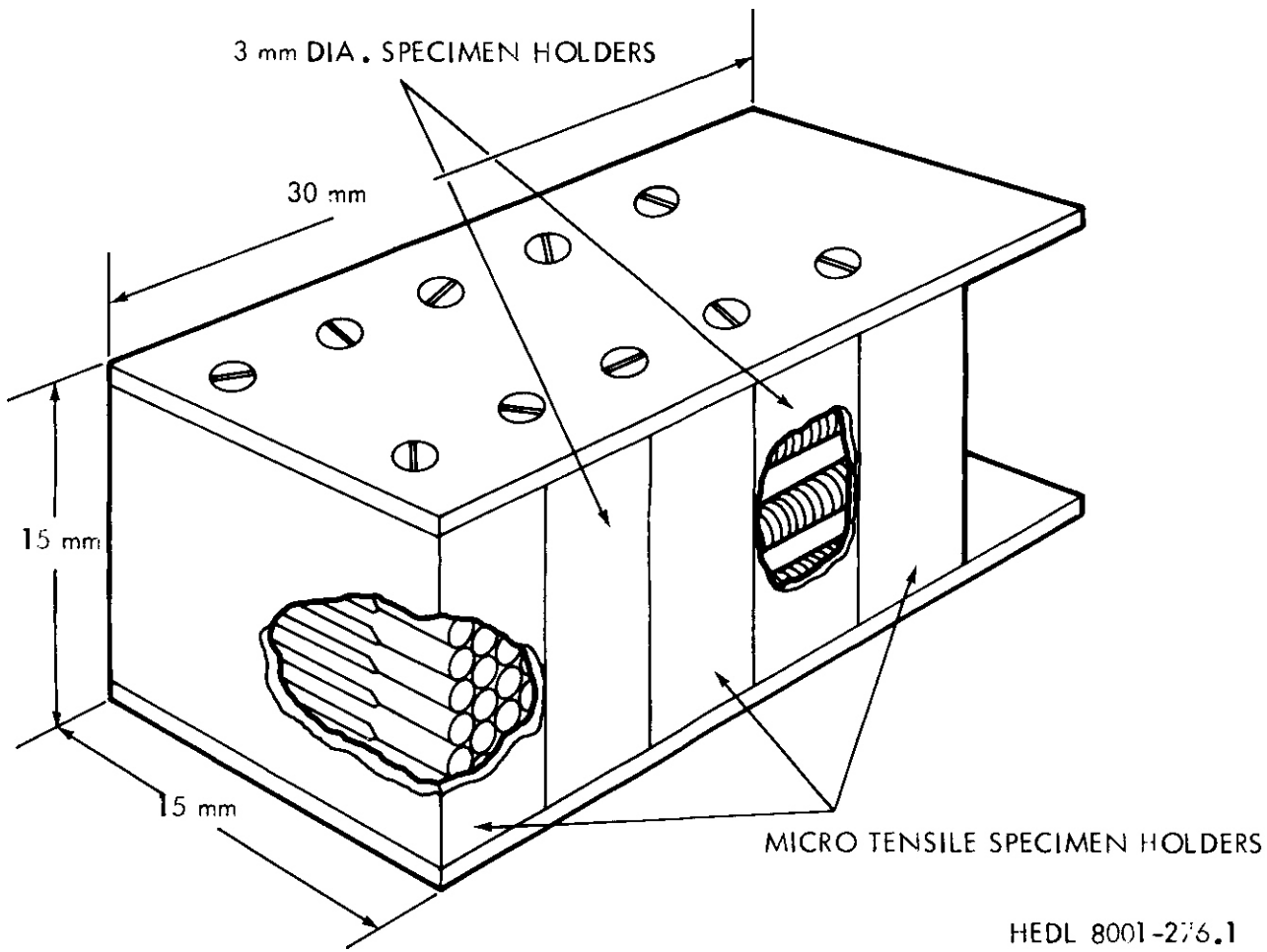
3 mm DIA. SPECIMEN HOLDERS
30 mm
15 mm
15 mm
MICRO TENSILE SPECIMEN HOLDERS
HEDL 8001-276.1

FIGURE 1.

le.

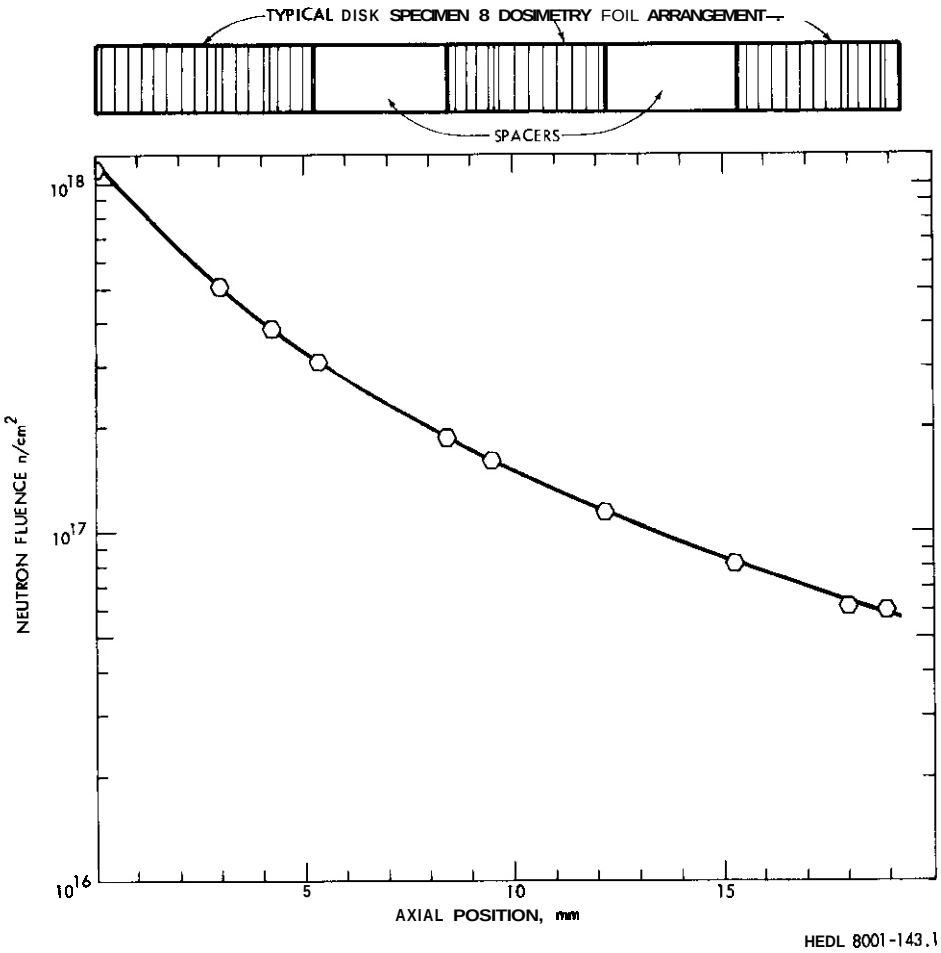

FIGURE **2.** Measured Fluences in Specimen Capsule Parallel to Beam Axis But Displaced Radially 3.8 mm (Nominally).

3. Elevated Temperature Irradiations

The first generation RTNS-II ultra high vacuum furnace was delivered to the RTNS-II facility. The furnace and associated components were assembled and checked out.

VI. FUTURE WORK

The fourth HEDL irradiation should begin in January 1980. It will contain microtensile and TEM disk specimens. Plans are being made for extended irradiations at an elevated temperature, probably near 300°C. Plans are also being made in collaboration with LLL for comparative irradiations in the Omega-West reactor at Los Alamos.

I. PROGRAM

Title: Effects of Irradiation on Fusion Reactor Materials
Principal Investigators: F. V. Nolfi, Jr. and A. P. L. Turner
Affiliation: Argonne National Laboratory

II. OBJECTIVE

The objective of this work is to establish the effects of flux, stress, alloying elements and solute redistribution on the creep-deformation behavior of various classes of materials during light-ion irradiation.

III. RELEVANT DAFS PROGRAM PLAN TASK/SUBTASK

SUBTASK II.C.ll.l Light Particle Irradiations

IV. SUMMARY

Further experiments were performed on solution annealed and aged type 316 stainless steel (MFE Heat # 15893) to resolve the phenomenon of negative irradiation creep. It is shown that negative strains are limited to a small dose; ~0.2 dpa. In-situ electron irradiations suggest the formation of ferrite via radiation induced segregation (RIS) as a possible mechanism.

In order to understand the effects of RIS on the mechanical properties, torsional creep measurements are also being made on model systems viz., pure Ni, Ni-Si and Ni-Al alloys. New data is presented on Ni-4 % Si that shows that RIS affects the mechanical properties by defect cluster decoration, long before the effects are visible in the microstructure. A two phase γ' dispersed alloy of Ni-Al shows very little radiation enhancement of creep, and no irradiation hardening.

V. ACCOMPLISHMENTS AND STATUS

A. Creep Deformation Behavior of Type 316 Stainless Steel -- V. Sethi

In a recent progress report, we showed that solution annealed and aged type 316 stainless steel (MFE Heat No. 15393) exhibits an anamolous radiation creep behavior[1] viz., negative irradiation creep. Further irradiation creep measurements have been made on wire specimens of the alloy to characterize the phenomenon. In addition, in-situ HVEM electron irradiations were performed at low dose-rates ($\sim 6 \times 10^{-6}$ dpa$\cdot$s^{-1}), and small total dose (<0.5 dpa) to identify the responsible mechanism. The experiments and results are described in this section.

Specimen 316 SA 15893-01, with a minimum diameter ~0.013 cm and gauge length ~0.5 cm, was installed in the torsional creep apparatus. Specimen preparation techniques and the details of the torsional creep apparatus are given elsewhere[1-2]. The specimen was heated to 400°C and a torque of 4.75×10^{-5} N$\cdot$m was applied (maximum shear stress at the minimum diameter ~110 MPa). The specimen was allowed to creep for 2.45 h prior to irradiation with 21 MeV deuterons (dose-rate $\sim 2 \times 10^{-6}$ dpa$\cdot$s^{-1}). The specimen was irradiated on four separate occasions to a total accumulated dose ~0.25 dpa.

Figure 1 illustrates the creep strain as a function of time for the specimen for the duration of the test 2.170 h. To facilitate the discussion, the creep strain curve is divided into nine regions that are separated by dotted lines, and are labeled as regions 1-9. Region 1 shows the thermal creep curve at 400°C and 110 MPa prior to irradiation. During the first irradiation (region 2), we observe irradiation enhanced creep that quickly changes to negative creep, and the alloy continues to deform against the applied stress for the duration of the first irradiation period. When the beam is turned off (region 3) the deformation behavior reverts to normal. During the second irradiation period (region 4) the negative creep resumes

but slows down continuously throughout the irradiation. Again, during the beam off period in region 5, normal thermal creep is observed with a creep-rate that is identical to that observed in regions 1 and 3 ($\sim 6 \times 10^{-11} s^{-1}$). During the third irradiation period (region 6), the mechanism responsible for the negative deformation seems to have reached near saturation, and a gradual transition from negative creep to normal creep behavior is observed. During the fourth irradiation period (region 8), the creep-rate is higher than the thermal creep-rate i.e., irradiation-enhanced creep is observed. Figure 2 illustrates the accumulated strain in the specimen during irradiation as a function of dose. Transition from a negative creep to irradiation enhanced creep occurs at ~ 0.16 dpa, and for dose $\gtrsim 0.2$ dpa the creep-rate is constant ($\sim 3.2 \times 10^{-10,-1}$).

If one assumes that the irradiation creep curve shown in Figure 2 consists of two components viz., irradiation enhanced creep with a creep-rate $d.2 \times 10^{-10} s^{-1}$, and a negative creep component caused by precipitation, swelling etc., the total negative strain accumulated during the test is $\sim 6 \times 10^{-5}$.

The elastic response of a wire specimen of diameter d, shear modulus G under the action of an applied torque T is given by

$$\gamma_{el} = \frac{16\,T}{\pi d^3 G} = \frac{\tau_{max}}{G} \qquad (1)$$

where γ_{el} is the shear strain and τ_{max} is the maximum shear stress. Based on Equation 1, in a previous progress report[1] we speculated that a dose dependent irradiation induced increase in G and/or d will result in a decrease in γ_{el} at a fixed T, which if larger than the irradiation creep-rate will cause a net negative strain to be measured during the course of a creep experiment. In Fig. 3 the plots of γ_{el} vs. T are shown for the specimen 316 SA 15893-01 for preirradiation and post-irradiation conditions. Irradiation induced increase in the stiffness is quite clear inplying that $d^3 \cdot G$ has increased. For $T = 4.75 \times 10^{-5}$ N·m (maximum shear stress

$\sim$110 MPa) the reduction in γ_{el} is $\sim 10^{-4}$, consistent with the amount of negative strain calculated from the irradiation creep strain curve of Figure 2.

In order to identify the microstructural changes that are responsible for the modulus and density changes, thin foils of the alloy, that had been heat treated similarly to the creep specimens, were irradiated with 1 MeV electrons in the Kratos EM-7 1.2 MV High Voltage Electron Microscope. Irradiation conditions were similar to those of the Cyclotron irradiations i.e., 400°C; dose-rate $<10^{-5}$ dpa$\cdot$s^{-1} and total dose $\sim$0.2 dpa. To achieve these low dose-rates, irradiations were carried out at low magnifications with defocused beam, and thus in-situ observation was not possible. Irradiated regions were later examined in the JEM 100C microscope. Electron irradiated foils were found to contain irregularly shaped precipitates (Figure 4). Selected area diffraction patterns obtained from these particles are consistent with a body centered cubic lattice with the lattice parameter a = 2.878 which is the expected lattice parameter for a high chromium ferrite, α phase.

The formation of α phase in the alloy at these small doses is quite surprising, yet consistent with the rationalization of negative creep as an irradiation induced reduction in the elastic strain. The formation of α phase is expected to cause an increase in the effective shear modulus[3], as well as an increase in the volume of the specimen.

B. Radiation-Induced Segregation and Irradiation Creep -- V. Sethi and R. Scholz

This section deals with experiments designed to determine the effects of radiation-induced segregation (RIS) on creep deformation in model alloys.

1. Ni - 4 % Si

In a previous progress report[2] we showed that irradiation enhances the creep-rate of pure Ni by $\sim$40% more than that of Ni - 4 % Si, when

stresses were selected such that preirradiation thermal creep-rates for the two materials were comparable. We also showed that the alloy exhibits considerable irradiation hardening, while no such hardening was observed in the pure metal.

In-situ HVEM electron irradiations of the two materials were performed at 350°C with 1 MeV electrons at calculated dose-rates $\sim 6 \times 10^{-6}$ dpa·s^{-1}. Figure 5 illustrates the loop structures in pure Nickel (Fig. 5a) and in Ni - 4 % Si (Fig. 5b). The Frank loops observed in Ni are $\sim$600Å in diameter. They unfault and glide at relatively small thermal stresses that develop during specimen cool-down. The Frank loops observed in the alloy are $\sim$200Å in diameter with a considerably higher number density. In addition, the loops shown in Fig. 5b are decorated with $Ni_3Si(\gamma')$ precipitates, as is evident from the selected area diffraction pattern. It should be mentioned that γ' reflections appear only after an incubation dose $\sim$0.15 dpa, while creep data indicates that almost all of the irradiation hardening occurs at doses considerably smaller than this (see Fig. 6). Figure 6 shows the post-irradiation creep-rate of Ni - 4 % Si alloy as a function of dose. The data were obtained over a period of one week by performing one hour long irradiations, and monitoring the thermal creep after each irradiation. Clearly, a major fraction of the hardening occurs at doses <0.01 dpa, indicating that defect clusters are decorated and stablized by RIS *of* silicon very quickly, while γ' formation at the **loops** requires that considerably larger concentrations of silicon be achieved.

2. Ni - 12.8 % Al

Torsional Creep measurements were made on wire specimens of aged (1.5 h at 615°C) Ni -12.8 % Al alloy at 350°C, at $\sim$70 MPa maximum shear stress, before, during and after irradiation with 21 MeV deuterons (dose-rate $\sim 2 \times 10^{-6}$ dpa·s^{-1}). The important observations are described below.

(a). Figure 7 illustrates the irradiation creep strain curves for pure Ni, Ni - 4 % Si and aged Ni - 12.8 % Al. The preirradiation thermal

creep-rates for the three materials were identical. Clearly, the aged Ni - 12.8 % Al exhibits very little radiation enhancement of the creep-rate.

(b). Comparison of the preirradiation and post-irradiation thermal creep data is shown in Figs. 3 and 9. The alloy does not exhibit any irradiation hardening or softening for the small doses involved in these experiments. This is understandable because irradiation to these low doses would not be expected to increase the density of obstacles to dislocation motion significantly above the initially high density in the precipitation hardened alloy.

VI. REFERENCES

1. V. Sethi and F. V. Nolfi, Jr., DAFS Quarterly Progress Report for Period Ending December 31, 1978, p. 202.

2. V. Sethi, A. P. L. Turner and F. V. Nolfi, Jr., DAFS Quarterly Progress Report for Period Ending September 30, 1978, p. 192.

3. F. Garofalo, P. R. Malenock, and G. V. Smith, Symposium on Determination of Elastic Constants (Philadelphia), American Society for Testing Materials, New York, N.Y., June 1952, p. 10.

4. V. Sethi, R. Scholz and F. V. Nolfi, Jr., DAFS Quarterly Progress Report for Period Ending June 30, 1979, p. 226.

VII. FUTURE WORK

Stress and temperature dependencies of the irradiation creep-rate in Ni and Ni - 4 % Si alloy will be determined for comparison with theory to determine the operating mechanisms of irradiation enhancement. TEM examination of the irradiated stainless steel creep specimens will also be performed to confirm the presence of ferrite.

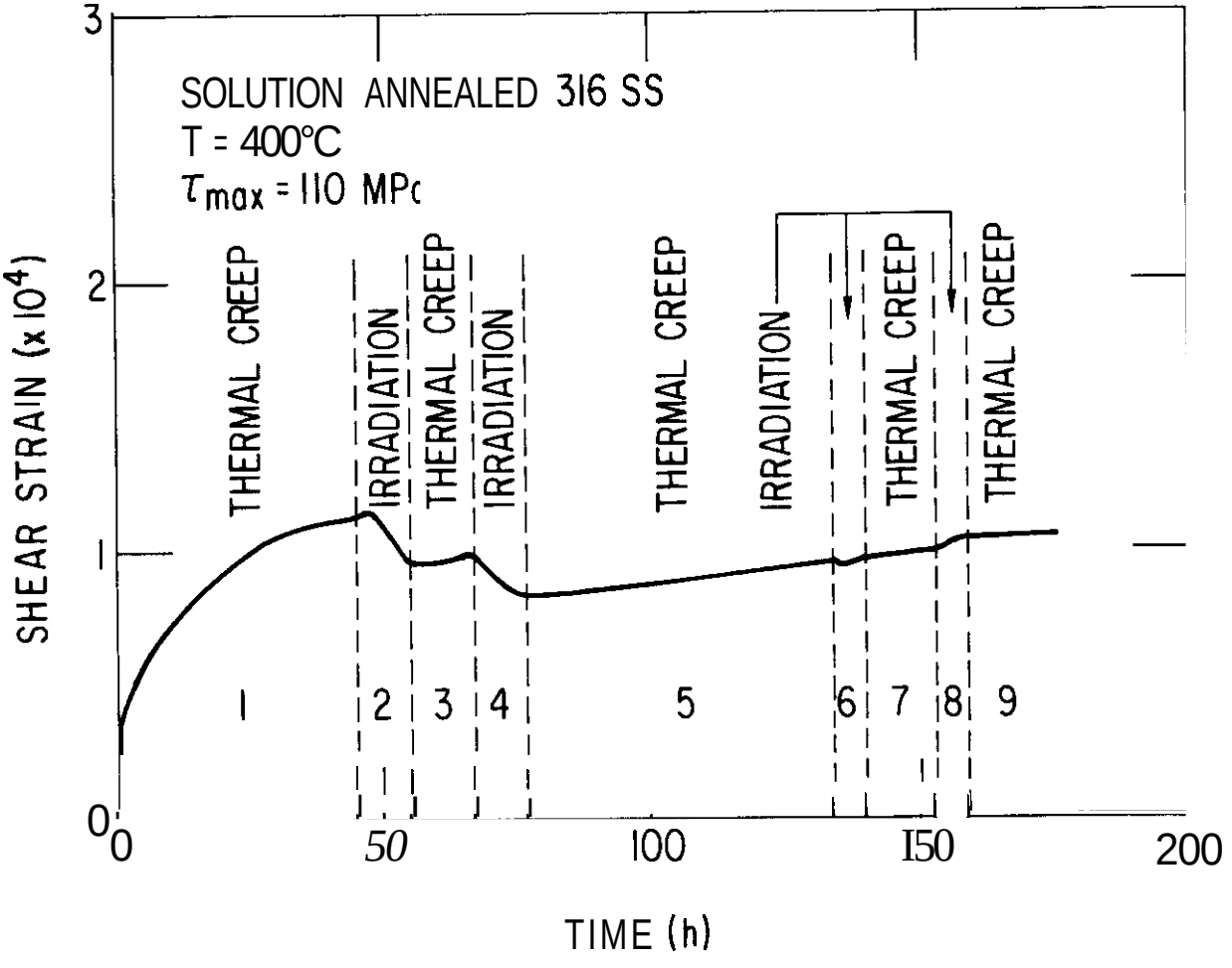

Figure 1. Creep strain curve for specimen 316 SA 15393-01.

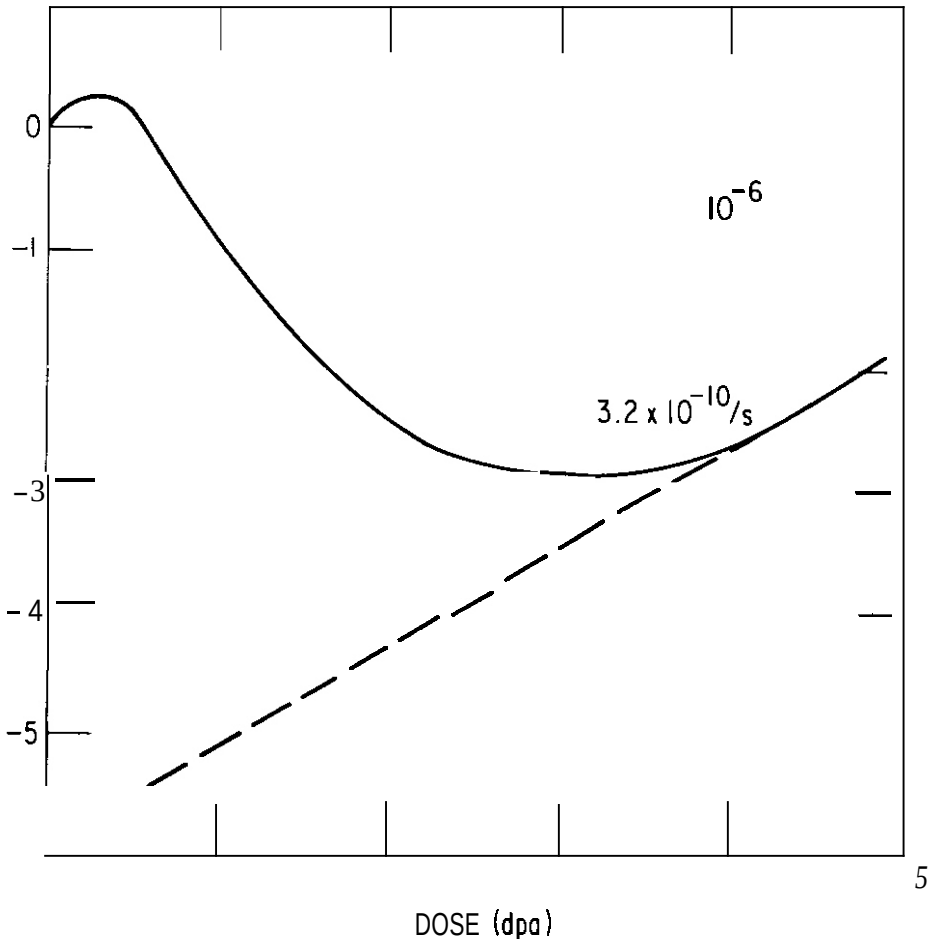

Figure 2. Creep strain curve for solution annealed and aged 316 stainless steel.

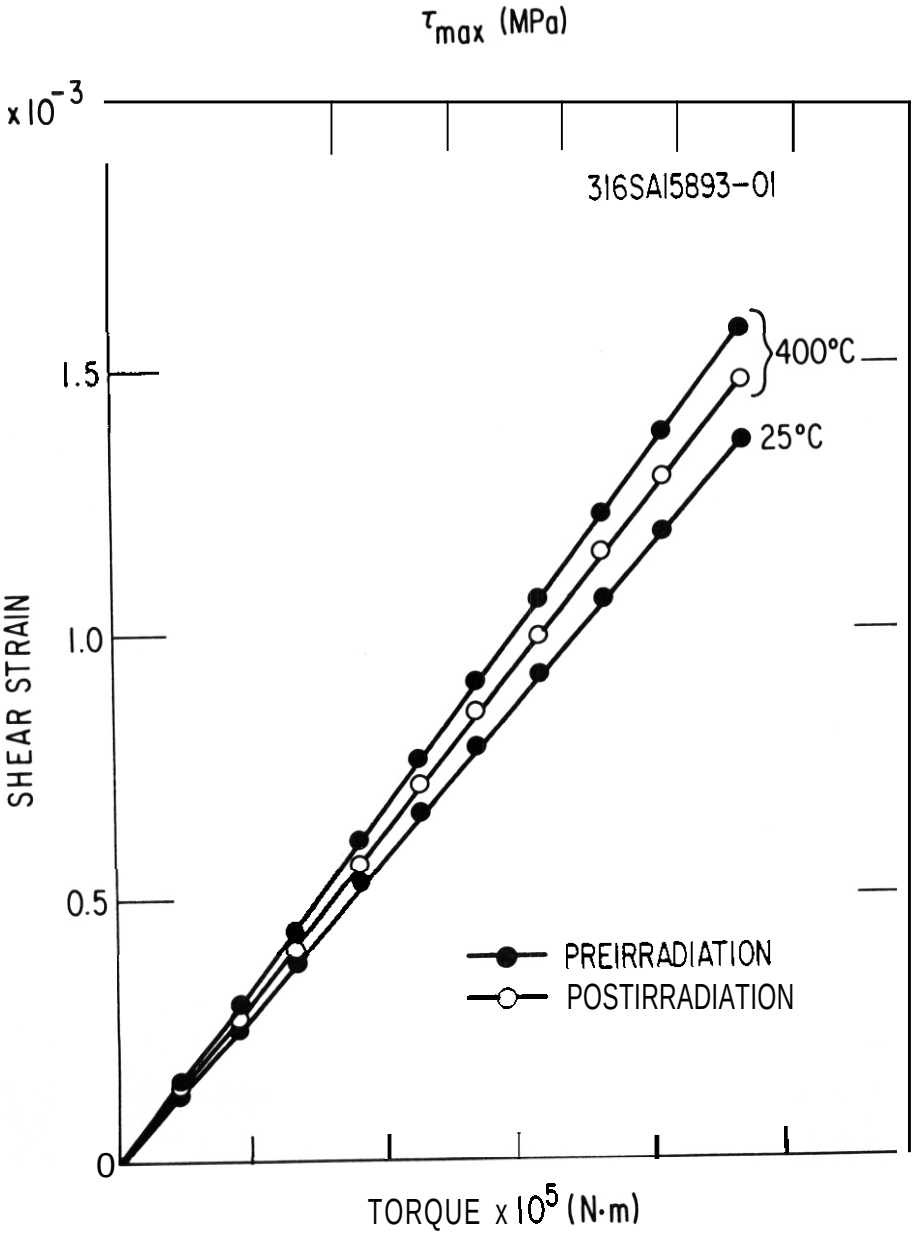

Figure 3. Comparison *of* the preirradiation and postirradiation Torsion modulus of specimen 316 SA 15893-01.

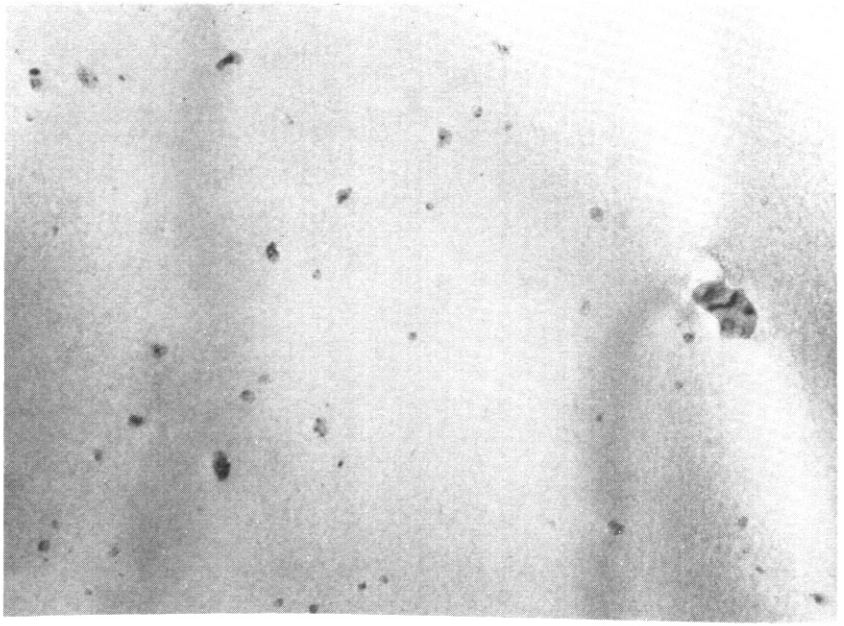

Figure 4. Microstructure of 1 MeV electron irradiated type 316 stainless steel. Irradiation conditions 400°C; 6 x 10^{-6} dpa·s^{-1}; and 0.3 dpa. Irregular shaped particles are ferrite.

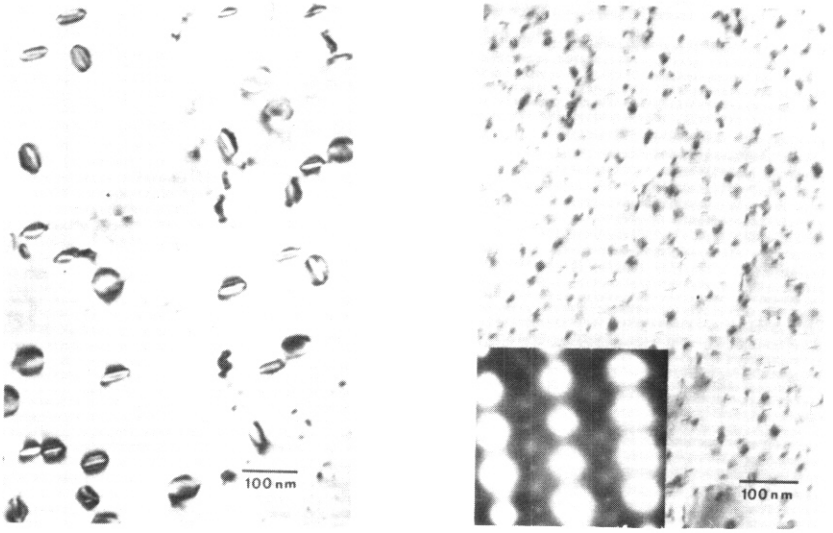

Figure 5. Microstructure of 1 MeV electron irradiated pure Ni and Ni - 4 % Si. Irradiation conditions 350°C; 6 x 10^{-6} dpa·s^{-1}; and 0.15 dpa.

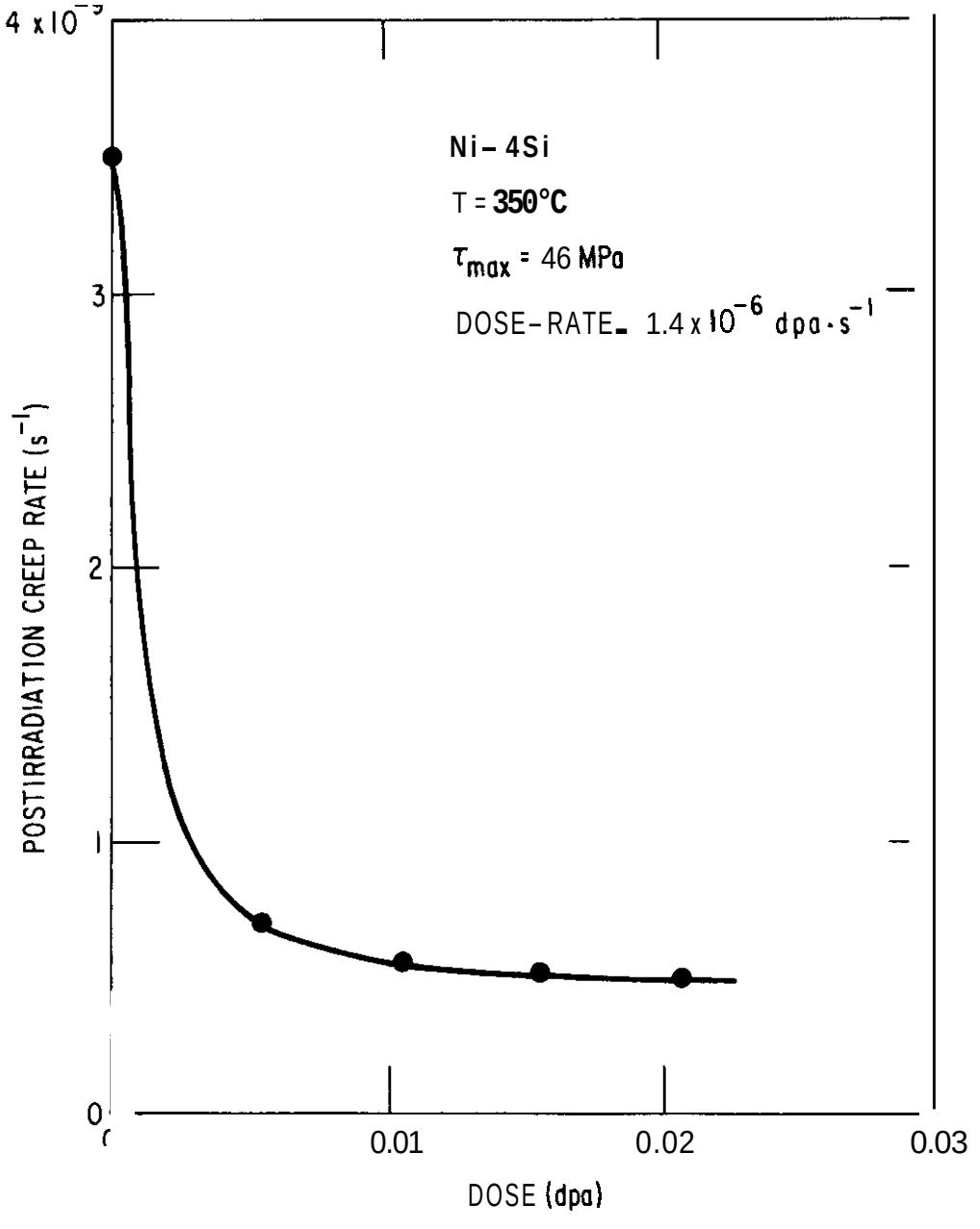

Figure 6. Postirradiation creep-rate of Ni - 4 Si as a function *of* irradiation dose.

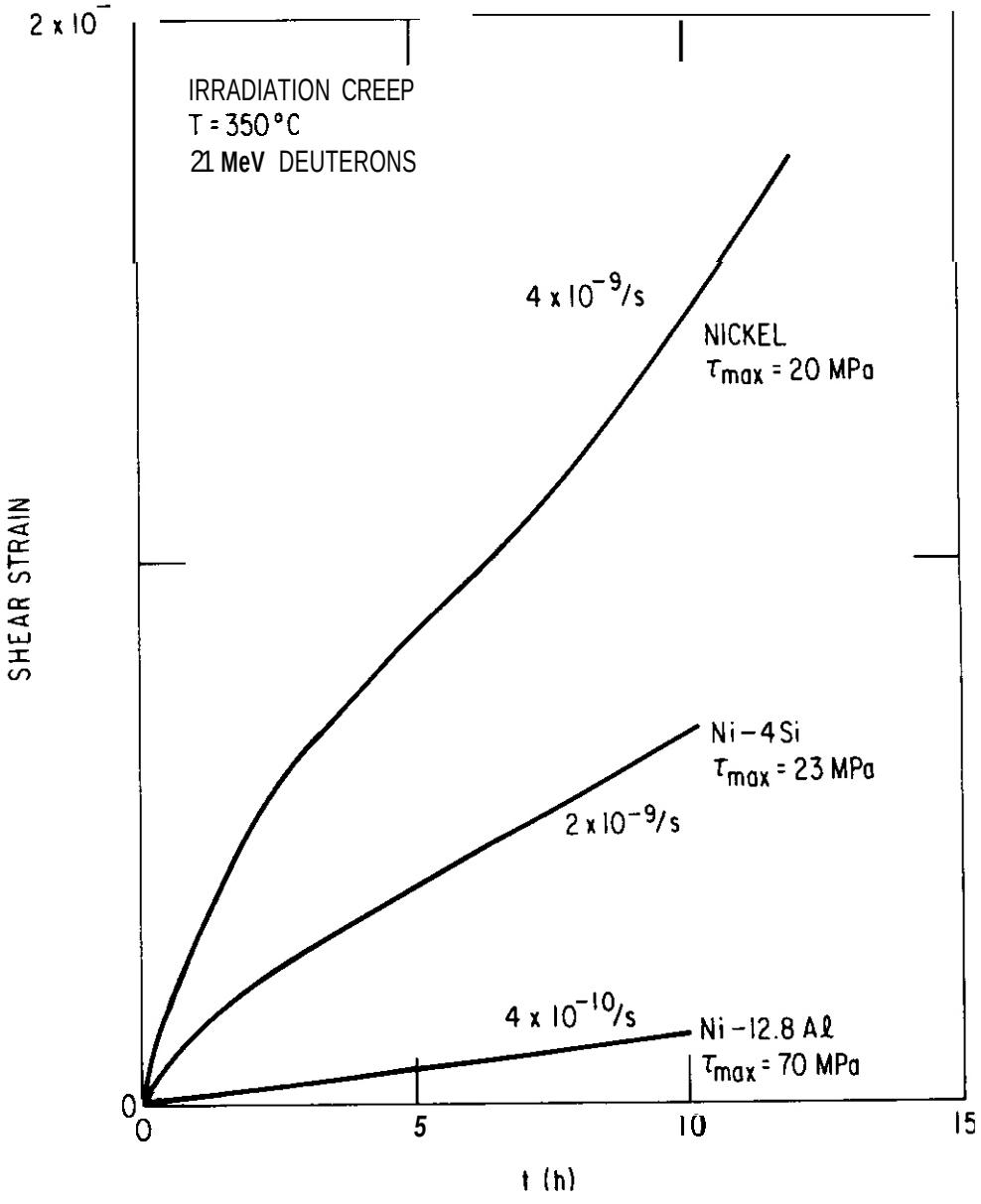

Figure 7. Comparison of irradiation creep strain curves for pure Ni, Ni - 4 Si and aged Ni - 12.8 Al alloys. Stress values were selected such that preirradiation thermal creep-rates were identical ($\sim 3 \times 10^{-10}$ s^{-1}).

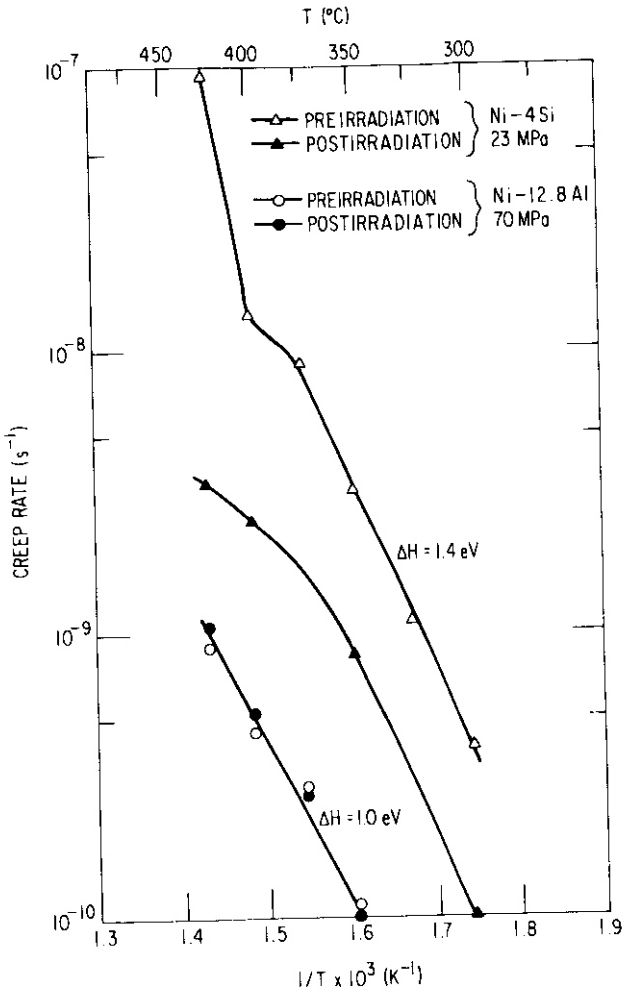

Figure 8. Temperature dependence of the thermal creep-rate for Ni - 4 Si and aged Ni - 12.8 Al alloys.

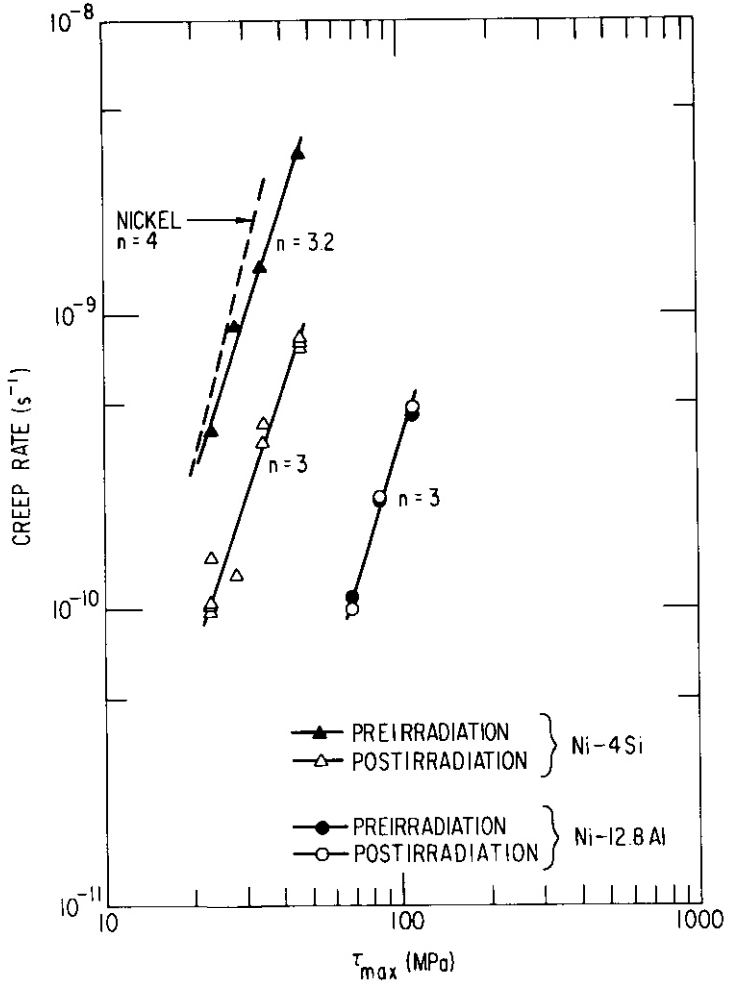

Figure 9. Comparison of the stress dependence of the thermal creep-rate for Ni, Ni - 4 Si and aged Ni - 12.8 Al alloys

I. PROGRAM

Title: Simulating the CTR Environment in the HVEM

Principal Investigators: W. A. Jesser and R. A. Johnson

Affiliation: University of Virginia

II. OBJECTIVE

The objective of this work is to experimentally investigate some of the parameters and fracture criteria in recent helium embrittlement theories.

III. RELEVANT DAFS PROGRAM TASK

Task II.C.14.2 Fundamental relations between microstructure and fracture mechanisms.

IV. SUMMARY

Experimental measurements of $a_{R'}$ the fractional area covered by dimples on the fracture surface, and $_{M}\alpha_{R}$, the fractional area cnvered by bubbles or voids in the matrix interior, were tarried *out* from micrographs of annealed unirradiated 316 stainless steel samples and neutron irradiated 304 stainless steel that were tested at 25^{a} and 600°C. No correlation was found to exist between the areal bubble density $_{M}\alpha_{R}$ and the grain boundary coverage $a_{R'}$ In addition no relationship was discovered between fracture surface dimple size and density with bubble (or void) size and density in the sample interior. An examination of a helium ion irradiated tensile specimen that exfoliated revealed that bubbles in the thin area participating in the fracture process are likely not overpressurized with helium. The fracture nature is not determined by the amount *of* lattice helium.

V. ACCOMPLISHMENTS AND STATUS

An Experimental Investigation Into Some Parameters and Fracture Criteria Used in Recent Helium Embrittlement Theories

J. I. Bennetch, J. A. Horton, and W. A. Jesser, Department of Materials Science, University of Virginia, Charlottesville, Virginia.

1. Introduction

A number of theories of helium embrittlement have come out recently in the literature, involving such parameters as a_R, the area fraction of the grain boundary occupied by helium bubbles, the initial bubble or cavity size and density versus the fracture surface dimple size and spacing, and the helium bubble gas pressure. Trinkhaus and Ullmaier (1) use a_R as the fracture criterion for their theory and in various calculations use either $a_R = 0.1$ or $\alpha_R = 0.5$ as the point at which fracture occurs. Goods and Nix (2) assume in their model that the dimple spacing on the fracture surface corresponds to the bubble spacing present before testing. Finally, Evans (3) assumes that the driving force for blistering is caused by an over population of helium in the cavities.

It is the purpose of this report to comment on each of these factors by a comparison of pertinent experimental measurements together with predicted values for each factor from these theories.

2. Experimental Details

Tensile samples of stainless steel types 304 and 316 were punched into ribbons with the central portion electropolished to a thickness transparent to 500 kV electrons. These were tested in-situ at two temperatures, 25° and 600°, inside a high voltage electron

microscope. The type 304 stainless steel samples had been previously neutron irradiated in the EBR-II reactor while the 316 stainless steel samples were either ones that were ion irradiated in-situ by 80 kV helium ions or were unirradiated annealed controls. Micrographs characterizing the bubble microstructure were taken before, during, and after the samples were strained to failure. For details of the equipment and similar tensile test conditions, one is referred to previous DAFS reports. Post-test examinations of the sample surface and interior were performed in a high resolution 100 kV Philips EM 400.

3. Experimental Results

a. Area Fraction Occupied by Bubble on Grain Boundaries

One common parameter in many theories of helium embrittlement is $a_{R'}$ the area fraction of a grain boundary occupied by helium bubbles. For comparison purposes we here introduce another parameter, ${}_{M}\alpha_{R}$, the area fraction of an arbitrary plane in the matrix occupied by helium bubbles. Since many theories assume the value of a_R must reach a critical value before fracture can occur, this parameter should be experimentally determined to enable verification of helium embrittlement mechanisms.

In order to calculate a_R for a given example, the grain boundary bubble size and areal density of bubbles on the grain boundary are needed. To compare a_R for a grain boundary to the equivalent quantity for an arbitrary plane in the matrix requires calculation of ${}_{M}\alpha_{R}$ for this matrix plane. Since, statistically, the amount of swelling $\Delta V/V$, in a volume V is equal to the fractional coverage $\Delta A/A$ of an arbitrary

plane of area A through the grain interior (5); thus we get:

$$_{M}\alpha_{R} = \frac{\Delta A}{A} = \frac{\Delta V}{V} = \text{amount of swelling.}$$

A comparison of a_R and $_{M}\alpha_{R}$ values measured from micrographs of representative helium irradiated stainless steel samples performed at this facility are shown in table I along with values obtained from measurements on micrographs published in recent articles from other authors in the literature. From this table, a number of features emerge. i) From values of $_{M}\alpha_{R}$ measured from different areas of the same sample, it is possible to obtain over an order of magnitude variation. ii) Intergranular fracture may occur when a_R as measured from TEM observations is 1% or less at elevated temperature while transgranular fracture may occur at room temperature when the value of α_R is 30%. iii) The deposited quantity of helium varied over almost 5 orders of magnitude and did not determine the nature of the fracture, i.e., transgranular, ductile fracture can occur at very high helium concentrations and intergranular fracture can occur at very low helium concentrations.

These observations do not form a large enough set of data to isolate the effect of each variable; however, they suggest that a unique, critical value of a_R is not essential to produce intergranular failure, i.e., complete helium embrittlement. Further, the quantity of helium in the lattice does not determine the nature of the fracture.

The inhomogeneous nature of the microstructure from one area of

Table I.

GRAIN BOUNDARY AND GRAIN INTERIOR BUBBLE AREA FRACTIONS

Source of Micrograph	Material	Concen. of He(appm)	Test T(C) / Irrad.T(C)	Grain Boundary Bubble Diam. (nm)	α_R (%)	Matrix Bubble Diam. (nm)	$^M\alpha_R$ (%)	Fracture Mode
Exp.#14			600°	6	2	none		T
Exp.#17			25° / 00°	3	5	70	1	T
Exp.#17			25° / 00°	0	10	270	8	T
Exp.#17			25° / 00°	0	30	10	7	T
Exp.#24			600° / 600°		1	50	2	I
Matsumoto et al(11)			--- / 700°		5	none		I
Sagués et al (6)			--- / 800°	30	≤	none		I
Goods & Nix(2)			40° / ---	15	0 8	none		I

I = inter-granular
T = trans-granular

the sample to the next has been observed by Kemm (5), and here such a variation introduces a large uncertainty into the measurement. The measurement of a_R from TEM data away from the fracture may not be representative of the a_R at the fracture surface. In order to investigate further this aspect of the problem, a comparison was made between TEM data from the sample interior and SEM data from the fracture surface and is presented in the next section.

b. Correlation of Fracture Surface Dimples with Interior Bubbles

In considering this criterion, most researchers have used bulk specimens, which they have fractured, and counted the bubbles or dimples on the fracture surface. They then would prepare and examine TEM samples from these post-failure specimens. These specimens would, by necessity, come from an area far enough from the fracture surface to enable a specimen to be prepared. The void or bubble densities from the samples would be examined from areas including grain boundaries. One might expect that the dimple spacing on the fracture surface corresponds to the bubble spacing before testing, especially in the case of intergranular fracture. The experiments of Sagues et al. (6) showed a much larger a_R at the fracture surface than at the grain boundaries in the TEM samples (a_R -50% as compared to - 3% respectively). To explain this "observation gap" Trinkhaus and Ullmaier (1) conclude that the TEM results were from an area far enough away from the fracture edge to have a lower stress and thus a lower fractional area coverage of bubbles at grain boundaries than at the fracture surface. Trinkhaus and Ullmaier term this discrepancy as

an "observation gap". Goods and Nix (2) assume in their model that the dimple spacing on the fracture surface corresponds to the bubble spacing prior to testing. They experimentally report that the fracture surface dimples are an order of magnitude closer together than the bubble spacing. They call this a "curious result and as yet unexplained".

In order to further investigate the "observation gap" phenomenon a series of SEM and TEM micrographs of samples that had been pulled to fracture in-situ in the HVEM were examined to determine correlations between bubble spacing prior to testing and dimple spacing after testing for different sample pretreatments, microstructures, and test temperatures. Samples that fractured transgranularly were included. For comparison purposes, similar measurements were conducted on micrographs from Sague's paper. The results of this investigation are summarized in table 2. A number of observations are apparent. First, looking at those samples that fractured transgranularly, one can see that the TEM-determined values of $_{M}\alpha_{R}$ for the neutron irradiated samples ranged from 0.3% to 1% and the SEM-determined values of α_R from the fracture surfaces of the same samples ranged from 8% to 15% respectively. In the same samples, void densities were two or three orders of magnitude greater than the dimple equivalent volume densities. (Converted from measured dimple areal densities). Note that the above discrepancy between data from the sample interior and that from the fracture surfaces is found at room temperature as well as at 600°C. One further notices that the dimple density and a_R values

Table 2

A COMPARISON OF INTERIOR VOID OR BUBBLES WITH FRACTURE SURFACE DIMPLES

Exp #	Pretreatment	Test T (°C)	Void or Bubble Size(nm)	Void or Bubble Density(cm^{-3})	Dimple Size(μm)	Dimple Density ($10^7 cm^{-2}$)	Dimple Equiv.vol. Density ($10^{11} cm^{-3}$)	Area Frac. (%) matrix plane $M^{\alpha}R$	Area Frac. (%) grain boundary $^{\alpha}R$	Area Frac. (%) fracture surface $^{\alpha}R$	Fracture Mode
2	unirradiated annealed	25	none		5	3	2	0	-	6	T
6	unirradiated annealed	600	none		7	2	0.9	0	-	9	T
20	neutron irrad	25	<20	1×10^{15}	7	2	0.9	0.3	-	8	T
12	neutron irrad	600	<20	1×10^{15}	8	0.3	0.5	0.3	-	3	I
5	neutron irrad	600	30	1×10^{14}	1	2	0.9	1	-	15	T
Sagués et al (6)	helium irrad.	700	30	$1\times10^{13} cm^{-2}$ on Grain Boundary	1	2	--	-	3	~50	I

obtained at the fracture surfaces of unirradiated samples are similar to those values obtained from the irradiated samples tested under similar conditions. These data show that for transgranular fracture the dimple density is independent of bubble population over a test temperature range. Evidently the dimples are determined by the plastic deformation processes rather than a pre-existing bubble population. The small cavities at the fracture surface were not discernable in the SEM micrographs and hence the dimple data is for dimples larger than about .1μm. The small cavities on the fracture surface which correspond to the pre-existing bubbles were observed in the HVEM samples to increase in diameter by a factor two, while the number density of cavities remained constant. This plastic deformation induced enlargement of bubbles has been discussed before (7) and could account for a factor 8 discrepancy between the TEM and SEM data. However, in our case the dimples are too large to be generated by the above observed plastic deformation enlargement of bubbles.

Turning now to the case of intergranular fracture, one can see from the data in table 2 that an "observation gap" exists in this case also. Again there is about an order of magnitude difference between the magnitude of $_{M}\alpha_{R}$ and the larger α_{R} at the fracture surface. Similarly the bubble area density for the neutron case is much different from the corresponding dimple densities. Once again there exists a large "observation gap" between TEM-determined α_{R} values and SEM-determined a_{R} values, from~3% to -50% for the intergranular helium

case. Finally, neither by examining the initial bubble nor final dimple size, can one see a simple correlation between the two for either transgranular or intergranular fracture.

Looking at this problem of the bubble/dimple "observation gap" from another point of view, an examination of the TEM transparent fracture surface exposed by an exfoliated helium-irradiation-produced blister cap was conducted. The purpose of this experiment was to eliminate the "observation gap" since both the fracture surface and the matrix interior could be observed from the same area. Since the University of Virginia facility has available a high resolution 100 kV Philips EM 400 with SED and STEM as well as TEM modes of operation, the identical area of sample could be viewed at the surface and in the interior.

The sample under consideration blistered in a region thin enough so that the underlying area was electron transparent at 100 kV. These thin areas are of a thickness (<100 nm) less than the helium range (282 nm at 80 kV). Blistering occurred on the side of the sample away from the helium beam. The area studied in detail came from a (in the subsequent tensile test after irradiation) crack parallel to the plane of the sample produced by an exfoliated layer which exposed the fracture surface of the bottom layer. Secondary electron-detector formed images at the top and bottom surfaces were taken as well as scanning transmission electron micrographs at the same area. Interior bubble and surface dimple population densities were noted and plotted on a histogram (figure 1). Comparison with bubbles

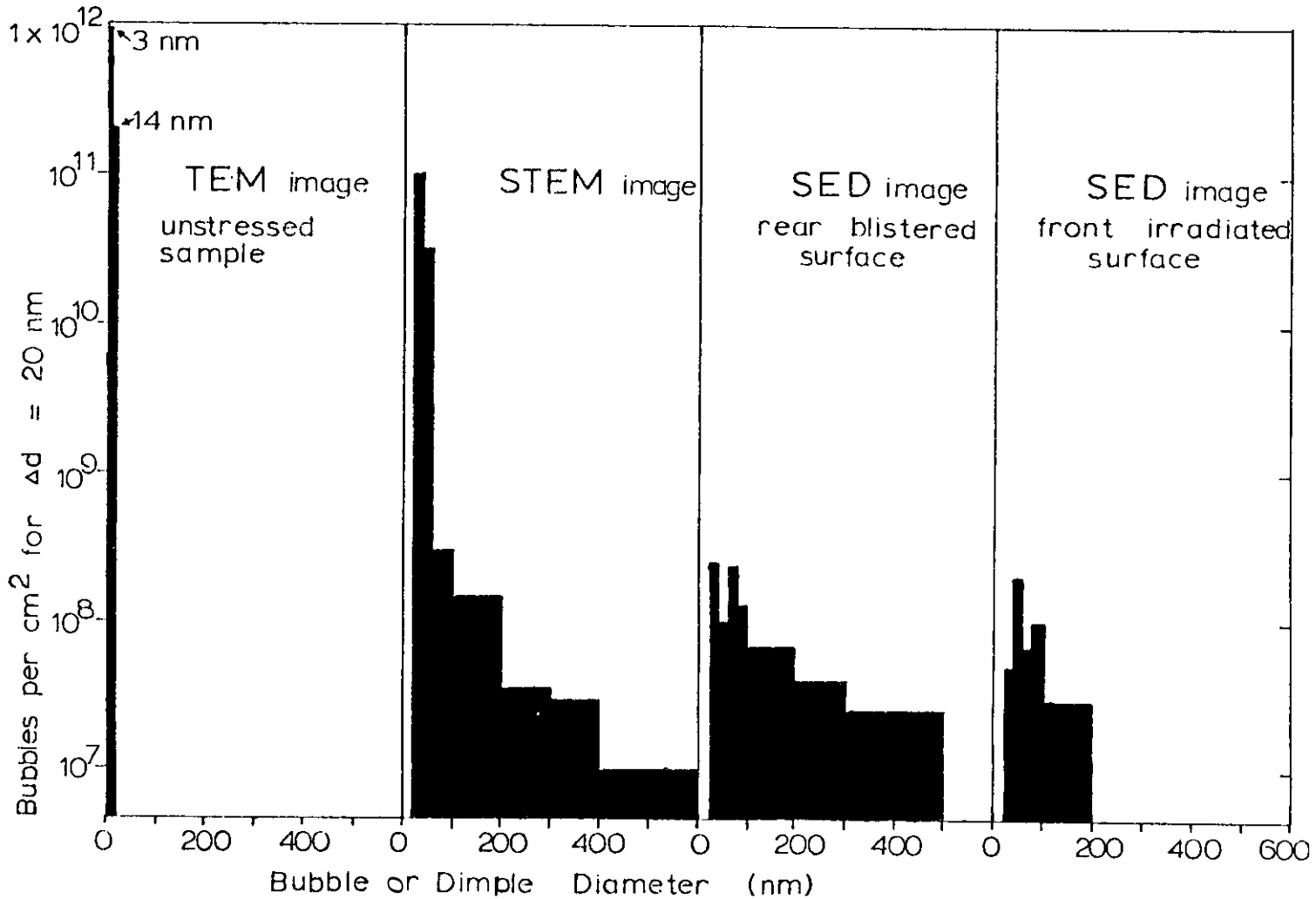

Figure 1

Histogram Showing Interior Bubble and Surface Dimple Population Densities.

formed in an unstressed sample subjected to a similar irradiation history was made on the same histogram. As one can see in the figure, there was a high density of small bubbles as revealed by TEM and STEM micrographs that are not seen on the surface. This probably means the bubbles in the interior of the blistered region were radiation induced, rather than plastic/deformation induced cavities, since the bubbles of a similar size and density were found in unstressed samples, as seen from the figure. As the bubble diameter is increased, the number of bubbles seen in the surface (SED) images approaches that seen in the transmission (STEM) image. By adding the two SED images at rear and front surfaces plus the TEM image, one can approximately reconstruct the STEM histogram as should be the case. The resolution of the STEM and SED micrographs was not good enough to resolve the smallest bubbles. One can plainly see that the rear blistered fracture surface has dimples up to ~ 0.5μm in size, two and one half times larger than any feature on the front ion-bombarded surface. Dimple sizes of ~0.5 - 1.0μm were obtained before, as was shown in table 2 previously. Thus it appears the "observation gap" is a real phenomenon, not an artifact.

c. Critical Helium Bubble Pressure at Fracture

In theories of helium embrittlement, the consideration of the internal gas pressure of a helium bubble repeatedly enters the equations. Equilibrium bubbles are usually assumed to contain a helium gas pressure which balances the surface tension such that $P = 2\gamma/r$ where P is the pressure, γ is the surface tension, and r is

the radius of the bubble. Cost and Chen (8) calculated the number of helium atoms per bubble in equilibrium for a given bubble diameter using a virial equation, furthering the calculations of Barnes (9), who used a vander Waals equation with a correction factor. Evans (3), in his gas pressure driven theory of blistering, assumed over-pressurized bubbles which enlarge until they fracture the material between them. By using Cost and Chen's results to calculate the content of helium in equilibrium bubbles and comparing that result to the amount of implanted helium available to the bubbles one can estimate the role of helium pressure in the fracture process.

In order to calculate the helium concentrations in bubbles (which of course is related to the bubble pressure), the amount of deposited helium in 316 stainless steel for a given incident helium ion energy was calculated by using the E-DEP-I code as developed by Manning and Mueller(10). A Gaussian distribution for the helium deposition was assumed. The calculated helium concentrations were then averaged over the entire specimen thickness. In addition, all the implanted helium was assumed to diffuse to the bubbles, but not to the free surfaces. Both assumptions led to a value which represents the maximum amount of helium that could be contained in the bubbles. The ratio of the number of helium atoms contained in equilibrium bubbles (by Cost and Chen) at a given diameter to the maximum number of implanted helium that could be contained in these same bubbles was calculated from micrographs from four experiments, as summarized in table 3. The first two micrographs, taken of thin areas

Table 3.

AMOUNT OF IMPLANTED HELIUM TRAPPED IN BUBBLES

Experiment #	Bubble Diam. (nm)	Bubble Density (cm^{-3})	Swelling (%)	Calculated Ratio of No. of HE Atoms that could be contained in Equilibrium Bubbles to No. of Implanted HE Atoms
13	25	2×10^{16}	10	11
17	10	5×10^{16}	4	2
19	270	1×10^{13}	10	.01
24	130	3×10^{14}	≤0	.6

in a 100 kV TEM, revealed small bubbles (average diameter of 25 nm and 10 nm, respectively) with corresponding ratios of 11 and 2 while the last two, taken in a 500 kV HVEM, showed much larger bubbles (270 nm and 130 nm, respectively) in thicker areas of specimens and much smaller ratios of 0.01 and 0.6. These calculations show that in the thin regions of a sample, there is more bubble volume than helium volume at the equilibrium pressure to fill them. The implication of this result for thin specimens is that the bubbles are void-like in their properties. Since blistering also occurred in nearby thin areas and since of course, the crack leading to failure also propagated through thin areas, this suggests that a critical helium bubble pressure may not be necessary for crack propagation and exfoliation or blistering.

4. Conclusions

a. It appears that a unique, critical area fraction, α_R, of grain boundary occupied by helium bubbles is not necessary to produce intergranular fracture or helium embrittlement.

b. No correlation was found between dimple size or areal density and bubble size or areal density.

c. It has been observed in thin specimens (<100 nm thick) that blistering due to helium irradiation may occur even when the bubbles are not filled with helium (i.e., are void-like.)

d. Helium embrittlement (intergranular fracture) is not correlated to a fixed concentration of helium.

VI. REFERENCES

1. H. Trinkhaus and H. Ullmaier, "A Model for the High-Temperature Embrittlement of Metals Containing Helium", Phil. Mag. A 39 (1979) 563.

2. S. H. Goods and W. D. Nix, "A Comparison of the Embrittling Effects of H_2O Bubbles in Ag with Those of Helium Bubbles in Ni - 6% W", Acta Met. 24 (1976) 1041.

3. J. H. Evans, "An Intergranular Fracture Mechanism of Blister Formation on Helium Irradiated Metals", J. of N. Mat. 68 (1977) 129.

4. E. E. Underwood, "Quantitative Stereology", Addison-Wesley (1970).

5. K. R. Kemm, "Inhomogeneous Clustering of Radiation Damage After Neutron Irradiation Between 200° and 400° C", S. Afr. J. Phys. 2 no. 3 (1979) 99.

6. A. A. Sagues, H. Schroeder, W. Kesternich, and H. Ullmaier, "The Influence of Helium on the High Temperature Mechanical Properties of an Austenitic Stainless Steel", J. of N. Mat. 78 (1978) 289.

7. J. I. Bennetch, J. A. Horton, and W. A. Jesser, "In-situ HVEM Tensile Tests of Helium-Irradiated 316 Stainless Steel", Damage Analysis and Fundamental Studies Quarterly Progress Report - Januarv - March 1979 (DOE/ET - 0065/5, May 1979) 236.

8. J. R. Cost and K. Y. Chen, "The Number of Gas Atoms Per Bubble of Inert Gas in a Solid", J. of N. Mat. 67 (1977) 265.

9. R. S. Barnes, "A Theory *of* Swelling and Gas Release for Reactor Mateials", J. of N. Mat., 11 (1964) 135.

10. I. Manning and G. P. Mueller, "Depth Distribution of Energy Deposition by Ion Bombardment", Comp. Phys. Comm. 7 (1964) 85.

11. K. Matsumoto, T. Kataoka, M. Terasawa, M. Shimada, S. Nakahigashi, H. Sakairi, and E. Yagi, "Embrittlement of Austenitic Stainless Steel Irradiated with *a*- Particles", J. of N. Mat. 67 (1977) 97.

VII. FUTURE WORK

It is planned to test additional samples covering a wide variety of microstructures in order to better determine the relationship between microstructure and fracture mechanisms.

I. PROGRAM

Title: Irradiation Effects Analysis (AKJ)
Principal Investigator: D. G. Doran
Affiliation: Hanford Engineering Development Laboratory

II. OBJECTIVE

The objectives of this work are 1) to determine the utility of *in-situ* HVEM deformation experiments for characterizing the effect of irradiation on mechanical behavior, and 2) to investigate the cause of reduced ductility of an Fe-0.3%Cu alloy following neutron irradiation.

111. RELEVANT DAFS PROGRAM TASK/SUBTASK

TASK II.C.14 Models of Flow and Fracture Under Irradiation

IV. SUMMARY

In an effort to better understand the nature of irradiation embrittlement of low alloy steels, *in-situ* HVEM deformation tests have been performed on pure iron and iron-0.3% copper ribbon tensile specimens in both the unirradiated and irradiated (2.5×10^{19} n/cm^2, E>1 MeV at 290°C) conditions. Microstructural response is described principally in terms of the matrix in which cracks were observed to propagate across the different specimens. Major differences between the irradiated iron-copper alloy and the other material conditions were 1) the plastic zone which developed ahead of propagating cracks was smaller, and 2) dislocations were found to develop a crenulated structure uncharacteristic of the other conditions studied. It is inferred that the crenulations result from the presence of obstacles to dislocation motion and thereby demonstrate the matrix strengthening effect of small, radiation-induced, presumably copper-rich precipitates. However, the obstacles which are most effective in retarding dislocation motion are found to be distributed on a much coarser scale than

that of the radiation-induced dislocation loops.

V. ACCOMPLISHMENTS AND STATUS

A. HVEM *In-situ* Deformation of Neutron Irradiated Fe-0.3a/o Cu

D. S. Gelles (HEDL)

1. Introduction

Embrittlement of light water reactor (LWR) pressure vessel steels due to neutron irradiation is a well-known,'') but not well-understood phenomenon. Such steels have a characteristic of undergoing a transition from ductile to brittle failure as the test temperature is reduced. Neutron irradiation results in an upward shift of the transition temperature and a reduction of the toughness at temperatures abcve the transition temperature. The problem is of interest due to the fact that ferritic steels are now being seriously considered as alternatives to austenitic steels for service in fusion reactors.(2)

The level of copper impurity in pressure vessel steels is found to have a strong influence on the magnitude of the irradiation-induced shift in the ductile-brittle transition temperature (DBTT). Hawthorne demonstrated that careful control of selected impurity elements, namely copper and phosphorus, resulted in reduced DBTT sensitivity.(3) More recently, Varsik and Byrne have attempted to correlate empirically this sensitivity with impurity content and find high sensitivity for copper above 0.1% whereas below 0.1% copper they can ascribe the effect to other impurities.(4) This insensitivity for copper levels below 0.1 percent was confirmed by work of Hawthorne et al. who compared pressure vessel steels with extra low (<0.06 percent) and low (<0.10 percent) copper contents.(5)

In studies to better understand the effect of copper on irradiation embrittlement, simple binary and ternary alloys have been employed. Smidt and Sprague compared Fe-0.3 a/oCu with pure iron, iron-base

alloys with vanadium, nickel, carbon or phosphorus, and several pressure vessel steels chosen for their different copper levels.[6] They found large increases in compressive yield strength after irradiation to 2.5 x 10^{19} n/cm^2 (E>1 MeV) at 280°C for both the copper alloy and the high copper pressure vessel weldment compared to the other materials tested. This could be correlated, in the case of the copper alloy, with rapid development of small dislocation loops (2.5 to 5.0 nm). They showed that such behavior was explainable by a heterogeneous loop nucleation model in which small clusters of copper atoms serve as nucleation sites for point defect aggregates. Brenner et al. obtained results consistent with this hypothesis using field-ion microscopy.[7] A specimen of iron-0.34 w/o Cu irradiated to 3.0 x 10^{19} n/cm^2 (E>1 MeV) was shown to contain imperfections tentatively identified as copper stabilized voids with a mean diameter of 0.6 nm and a number density of 8 x 10^{17}/cm^3. In line with the fact that brittle fracture is generally transcrystalline and that Auger spectroscopy of an embrittled pressure vessel steel reveals no copper segregation at the fracture surface,[8] it was therefore concluded that embrittlement was due to precipitation hardening of the matrix.

More recent work designed to study synergistic effects of alloying on irradiation embrittlement has been reported by Takaku et al.[9] Tensile tests were performed on a series of binary and ternary iron alloys containing copper after irradiation to a fluence of 5 x 10^{18} n/cm^2 (E>1 MeV) at 250°C and in some cases after isochronal anneals. Significant reductions in elongation were found with increasing copper content, whereas, for a constant copper level of 0.1 w/o, additions of titanium, silicon and aluminum reduced the effect. The Fe-0.3 w/o Cu alloy was found to have failed intergranularly following irradiation; failure remained intergranular after annealing at 300°C for ten hours. (Electron microprobe analysis did not reveal copper segregated on the fracture surface but such experiments cannot detect atomically thin layers.) Due to the intergranular failure observed, the authors proposed that grain boundary segregation of copper atoms is at least in part responsible for the irradiation embrittlement.

The present experiment was devised to better understand the role of copper additions on irradiation embrittlement of pressure vessel steels. It was deemed likely that copper precipitate particles were causing the embrittlement but the particles were so small that they could not be identified by transmission electron microscopy. However, increased yield strengths indicated that the particles must be affecting dislocation motion and therefore HVEM *in-situ* deformation studies might reveal the nature and effect of the particles on deformation behavior.

2. Experimental Procedure

Specimens of pure iron and Fe-0.3%Cu in the form of 50 μm (.05 mm) thick disks 3.0 mm in diameter were kindly provided by Smidt and Sprague of NRL. Five unirradiated disks and four disks irradiated to 2.5 x 10^{19} n/cm^2 (E>1 MeV) at 290°C remaining from their previous work[6] were supplied. Specimens were prepared as ribbon microtensile specimens with a gauge section up to 2 mm long, approximately 0.75 mm wide and approaching .002 mm thick. Such specimens were found to be extremely fragile and therefore a supporting ring consisting of the outer edge of the disk was retained for handling and loading purposes.

Specimens were mounted in a single tilting, heating, straining side-entry stage supplied by Gatan, Inc., Pittsburgh, Pennsylvania, Catalog #582-0000, especially designed to handle specimens 3 mm in length. This device provides a measurable strain in the specimen with readout in microns (0.001 mm) by transducer coupling to a heated straining wire and therefore the device represents a "hard" or strain-controlled tensile machine. Power input for heating the straining wire is manually controlled. After mounting was completed, supporting ring members were severed leaving only the ribbon tensile gauge section between the stage grips.

In-situ deformation experiments were performed at room temperature in a JEM-1000 high voltage electron microscope suitably adapted to accept the Gatan side entry stage geometry and operating at 1 MeV. The

beam intensity was kept low, below 1 dpa/hour, to reduce climb in the dislocation structure. During a fifteen minute examination of a particular area in the sample, climb could be detected. However, a specimen experienced further significant irradiation induced microstructural change during examination only in the unusual instance that examination times were prolonged. Microstructural information was primarily recorded on video tape using a low light level Isocon intensified camera system (Cohu Model 7304B) focused on a transmission fluorescent screen. Detailed dislocation and crack qeometries were also recorded on photographic film; in some cases, after the deformation experiment had been completed, the specimen was transferred to a double tilting stage and photographed.

3. Experimental Results
General Behavior

Specimen mounting and, in particular, severing of the specimen supporting ring member were found to be very delicate operations. Lateral movement of the grips can occur during loading thereby placing the specimen in sufficient tension to cause failure. This could be avoided by placing each specimen in slight compression during the support ring severing operation. As a result, a minor amount of plastic bending was unavoidable during specimen mounting.

As the strain was increased, the dislocation structure contained in the specimen was carefully inspected. In no specimen was dislocation motion typical of the onset of plastic yielding identified. Dislocation motion was only encountered in a localized region after crack tip formation had occurred. As a result, the onset of plastic deformation or yielding was not examined. It is possible that this response is a result of a strong tendency in these materials to form Luders bands. Alternatively, specimen non-uniformity, channel deformation, or simply bad luck prevented observation of the onset of plastic deformation. A future solution to this problem may lie in the development of fabrication techniques

which produce specimens with much smaller gage sections.

All ribbon tensile specimen conditions (the pure iron and the iron-copper alloy in both the unirradiated and the irradiated treatments) revealed the following deformation behavior. A narrow band of material tending to be oriented perpendicular to the tensile axis was thinned by plastic deformation ahead of the crack tip. As deformation proceeded, the material ahead of the crack tip appeared to shimmer as bend fringes were reoriented by dislocation motion. In many instances, individual dislocations could be resolved when suitable imaging conditions were obtained. These dislocations moved away from the crack tip on slip planes of a given orientation and then, sometime later, movement of dislocations occurred on a second, nearly orthogonal slip system. The slip planes were estimated to be inclined approximately 45° *to* the specimen foil surfaces. As strain proceeded, the crack tip was observed to propagate in a series of zigzag steps often in the direction of the operative dislocation slip system. The points marking each change in direction of the crack tip moved apart in the direction of the applied stress. Thus, the crack opening displacement was indeed due to the applied tensile stress. Several examples were encountered of apparent crack blunting by grain boundaries. On occasion, this resulted in nucleation of a second crack in the adjacent grain ahead of the propagating crack followed by failure of the linkage between the cracks, while propagation of the secondary crack continued in the adjacent grain. On no occasion was crack propagation observed to proceed along a grain boundary.

A preliminary analysis of the change in direction of a crack tip as a function of the crack tip opening displacement was performed for the case of a crack propagating in an unirradiated pure iron specimen. As shown in Figure 1, no correlation was found between the opening displacement, defined by the ratio of the distance between the points marking the last change in direction of the crack tip and the propagation length of the last crack segment, and the angle which the crack midline makes with the tensile axis. However, it can be noted that all data points lie in the range 37

to 68°C from the normal to the tensile axis. Also of note is the fact that, where two measurements were made for the same crack segment, the ratio of opening displacement versus length increased (as indicated by arrows on the figure).

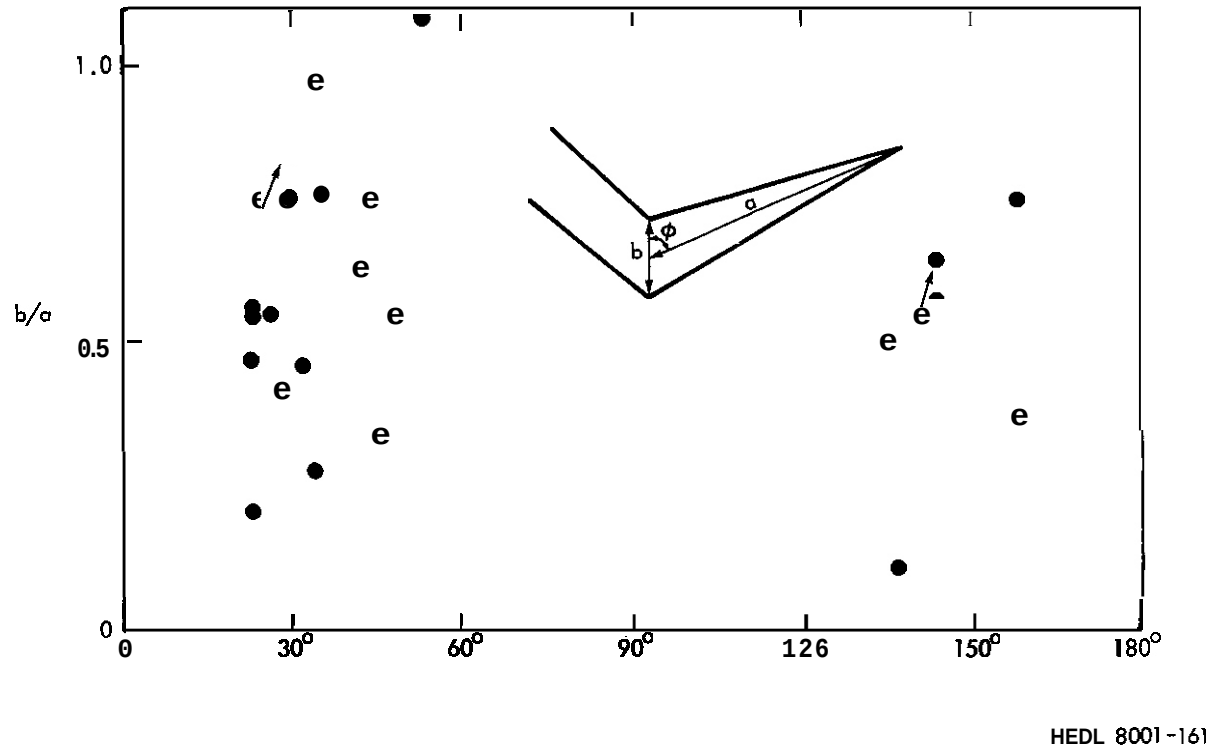

FIGURE 1. Crack Propagation Behavior in an Unirradiated Pure Iron Specimen. The crack opening displacement, b/a, is plotted as a function of the angle defining the direction of propagation ϕ.

Differences Due to Composition and Irradiation

Seven tensile specimens were successfully mounted in the straining stage and deformed while the resulting behavior was recorded on video tape. These comprised two unirradiated and one irradiated pure iron specimens, and two unirradiated and two irradiated Fe-0.3 a/o Cu specimens.

The irradiated specimens had been exposed to 2.5 x 10^{19} n/cm^2 at 290°C.

Differences in the straining behavior were detected for the different specimens tested. A correlation could be found between the size of the plastic zone ahead of a propagating crack tip and the alloy composition and irradiation history. Also, the shape of individual dislocations produced during deformation varied with alloy composition and irradiation history.

The variation in plastic zone size ahead of a propagating crack tip was found to vary with specimen condition as follows: both the width and extent of the plastic zone were notably smaller for the irradiated iron-copper alloy compared to the other three alloy conditions tested. Plastic zone widths at the crack tip and plastic zone lengths ahead of the propagating crack were determined directly from video tape playback of each tensile test. A summary is provided in Table 1. Variation was considerable in a given specimen (for example, due to crack blunting at a grain boundary) and accurate measurements were difficult to make. However, a clear indication of a trend is indicated: radiation damage in the iron-copper alloy has reduced the plastic zone size, consistent with yield strength behavior.[6] Furthermore, the magnitude of the plastic zone size reduction resulting from irradiation is estimated to be on the order of 50%.

The shape of individual dislocation segments produced during deformation varied as a function of specimen condition. The unirradiated specimens developed relatively straight dislocation segments during deformation. Examples were found where, within dislocation tangles, dislocations developed significant curvature, but these were clearly situations where dislocation pinning points were widely separated and the curvature of such dislocations was smooth.

TABLE 1

Plastic Zone Size Measurements of Propagating Cracks in Ribbon Tensile Specimens Deformed *In-Situ*

Specimen Condition	Plastic Zone					
	Width			Length		
	No. Measured	Size (nm)	Standard Dev. (nm)	No. Measured	Size (nm)	Standard Dev. (nm)
Pure iron	5	3200	800	5	9800	1500
Pure iron--irradiated	2	2800	300	3	10000	3500
Fe-0.3Cu	10	2800	500	10	12600	4700
Fe-0.3Cu--irradiated	9	2100	600	9	6200	2400

In comparison, the irradiated specimen showed somewhat different dislocation structure. Dislocation loops developed in both materials but they were generally larger and less dense in the case of the pure iron. However, whereas individual dislocation line segments were smooth in the pure iron case, they appeared crenulated for the iron-copper alloy. An example of this difference is provided in Figure 2. Figure 2a shows the dislocation structure in deformed irradiated pure iron and Figure 2b shows the dislocation structure in the irradiated Fe-0.3Cu alloy. In both cases, dislocations are inclined from foil top to bottom and arrayed on slip planes. The crenulations which appear on dislocations in the iron-copper alloy are apparently due to irradiation-induced features which impede dislocation motion. The dislocation loops in the iron-copper alloy presumably developed when dislocations bypassed obstacles by a looping rather than a cutting process. The smallest loop features are on the order of 8 nm in diameter and probably represent dislocation loops wrapped around individual obstacles, whereas larger elongated loops probably represent dislocations wrapped around more than one obstacle. The direction of dislocation motion is indicated both by the direction of curvature of individual dislocations and by surface slip plane traces which appear as faint white lines.

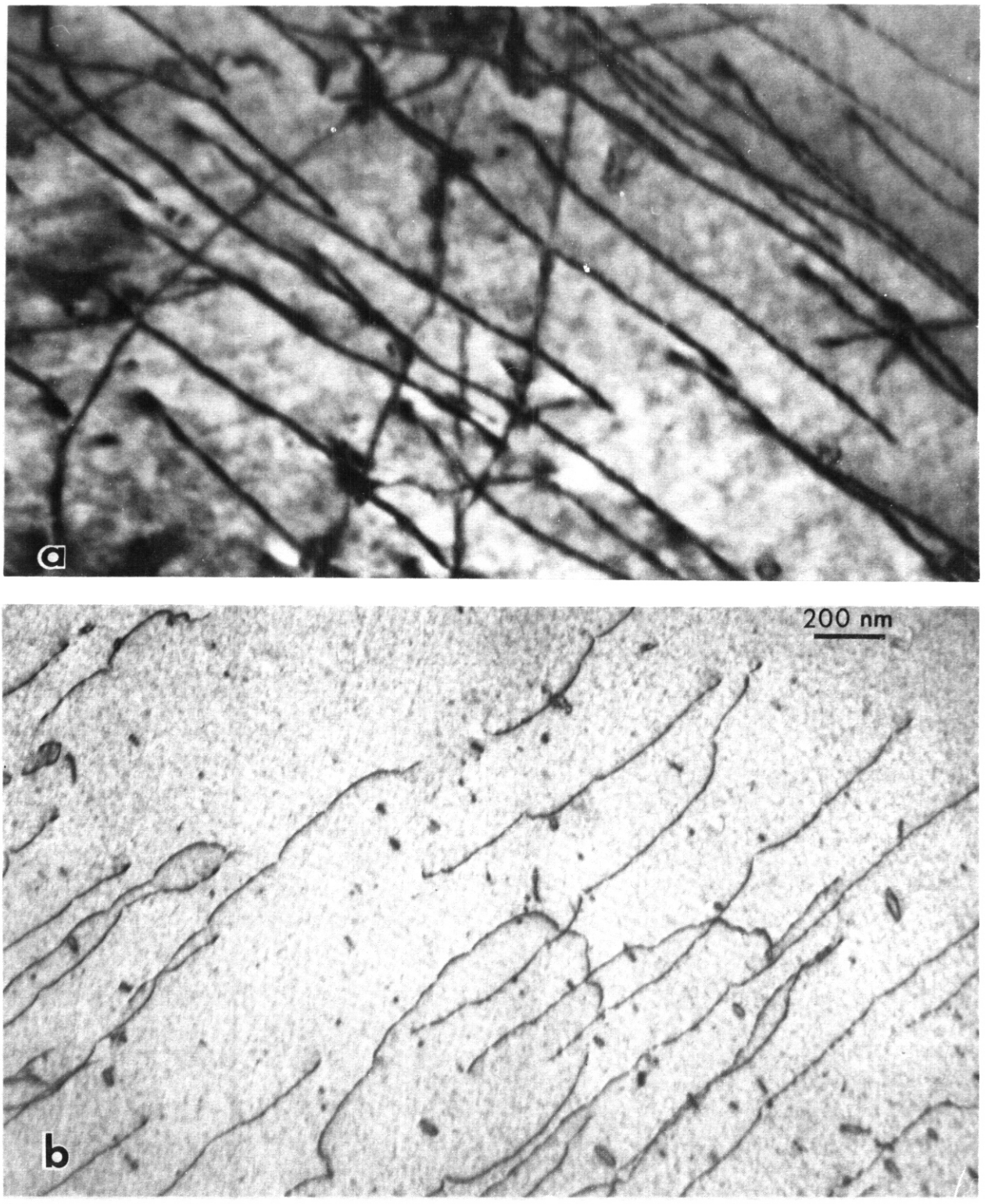

FIGURE 2. Comparison of Dislocation Structures in Irradiated Deformed Ribbon Tensile Specimens of a) Pure Iron and b) Iron-0.3 a/o Copper.

4. Discussion

The concept that copper atom clusters may form in irradiated iron-copper alloys and that such clusters may directly lead to hardening of the matrix and impede plastic deformation has been strengthened in the present study. During irradiation the iron-copper alloy was found to have developed obstacles to dislocation motion and these obstacles were effective even after significant deformation had occurred. Such was not the case with pure iron. Additionally, the extent of plastic deformation ahead of a propagating crack was less in the case of the iron-copper alloy demonstrating that the amount of local plasticity (and volume) prior to failure was reduced. (The plastic zone size should be a direct measure of the total elongation possible.[10]) These results are consistent with previous studies of embrittlement in pressure vessel steels and provide improved understanding of the nature of the embrittlement phenomenon.

However, what appears to be even more significant is the nature of the obstacles obstructing dislocation motion. Smidt and Sprague measured a density of 4×10^{15} dislocation loops/cm^3 in Fe-0.3Cu after irradiation to 2.5×10^{19} n/cm^2 and 2.5×10^{16} dislocation loops/cm^3 after 4.5×10^{20} n/cm^2 in the same material. This corresponds to a mean interparticle spacing along a line of random direction of approximately 25 nm. Examination of Figure 2b reveals that, although crenulations on the order of 25 nm can be observed, the spacing between the most effective obstacles is an order of magnitude larger. Thus, each dislocation loop produced by irradiation does not constitute a major obstacle to dislocation motion. Rather, the major obstacles have a number density three orders of magnitude smaller. They either represent the largest "dislocation loop" features, constituting 0.1% of the population, or they are some other radiation-induced feature which forms at a much lower number density, on the order of 10^{13} cm^{-3}.

5. Conclusions

In-situ deformation tests on pure iron and iron-0.3 a/o copper ribbon tensile specimens in both the unirradiated and irradiated (2.5×10^{19} n/cm^2, E>1 MeV at 290°C) conditions reveal a number of differences in microstructural development, and these are related to the alloy content and irradiation history.

1) The observed plastic zone size ahead of propagating cracks was smaller in the irradiated iron-copper alloy specimens.

2) Dislocations which moved during ***in-situ*** straining of the irradiated iron-copper alloy specimens developed a crenulated shape uncharacteristic of the other materials tested.

Therefore, it has been shown that radiation damage in iron containing copper introduces obstacles to dislocation motion which results in matrix hardening and an increased tendency for embrittlement. However, uncertainty exists concerning the nature of the obstacles, because their density is considerably less than dislocation loop densities measured in this material.

VI. REFERENCES

1. L. E. Steele, "Neutron Irradiation Embrittlement of Reactor Pressure Vessel Steels," Atomic Energy Review 7 (1969) p. 3.

2. Alloy Development for Irradiation Performance (ADIP) Quarterly Progress Report for the Period Ending September 30, 1979, DOE/ET-0058/7.

3. J. R. Hawthorne, "Demonstration of Improved Radiation Embrittlement Resistance of A533B Steel Through Control of Selected Residual Elements," Irradiation Effects on Structural Alloys for Nuclear Applications ASTM STP 484 (1971) p. 96.

4. J. D. Varsik and S. T. Byrne, "An Empirical Evaluation of the Irradiation Sensitivity of Reactor Pressure-Vessel Materials," Effects of Radiation on Structural Materials, Sprague/Kramer, eds., ASTM STP 683 (1979) P. 252.

5. J. R. Hawthorne, J. J. Koziol and S. T. Byrne, "Evaluation of Commercial Production A533-B Steel Plates and Weld Deposits with Extra-Low Copper Content for Radiation Resistance," Ibid., p. 325.

6. F. A. Smidt, Jr. and J. A. Sprague, "Property Changes Resulting from Impurity-Defect Interactions in Iron and Pressure-Vessel Steel Alloys." Effects of Radiation on Substructure and Mechanical Properties of Metal; and Alloys, ASTM STP 529 (1973) p. 78.

7. S. S. Brenner. R. Waaner and J. A. Spitznagel, "Field-Ion Microscope Detection of Ultra-Fine-Defects in Neutron-Irradiated Fe-0.34Pct Cu Alloy," Met. Trans. V9A (1978) p. 1761.

8. F. A. Smidt, Jr., D. F. Stein and A. Joski, "Auger Electron Spectroscopy Analysis of the Fracture Surfaces of Irradiated Pressure-Vessel Steels," NRL Report 7660, Naval Research Laboratory (1973).

9. H. Takaku, M. Tokiwai, H. Kuyano, Y. Nigashiguchi, M. Narui, Y. Suzuki and K. Matsuyama, "The Improvement of Irradiation-Enhanced Copper Embrittlement in Fe-Cu Alloys," J. Nucl. Mat. 80 (1979) p. 57.

10. D. S. Dugdale, "Yielding of Steel Sheets Containing Slits," J. Mech. Phys. Solid V8 (1960) p. 100.

VII. FUTURE WORK

As a scoping study, this work is completed.

VIII. PUBLICATIONS

D. S. Gelles, L. E. Thomas and R. W. Powell, "HVEM *In-Situ* Deformation of Neutron Irradiated Fe-0.3Cu," to be presented at the symposium, High Voltage Electron Microscopy: *In-Situ* Materials Science Research, to be held February 25, 1980, at Las Vegas, Nevada.

DISTRIBUTION

uc-20 (122)

uc-2oc (80)

DOE/RRT-HQ (7)
Flail Stop B-107
Washington, DC 20545

Asst Director, Materials Tech
NA Davies
JF Decker
PB Hemmig
KG Moses
RE Price
FT Scott

DOE/RL (3)
Richland, WA 99352

WA Burns
GM Chenevert
LA Pasquini

Argonne National Laboratory (4)
9700 South Cass Avenue
Argonne, IL 60439

L. R. Greenwood
A. Taylor
APL Turner
H. Wiedersich

Brookhaven National Laboratory
Associated Universities
Upton, NY 11973

Chairman, Nuclear Energy Dept

Columbia University
Plasma Physics Laboratory
New York, NY 10027

R. A. Gross

General Atomics Company (2)
P.O. Box 81608
San Diego, CA 92138

GR Hopkins
D. Stevenson

Lawrence Livermore Laboratory (2)
University of California
P.O. Cox 808
Livermore. CA 94550

MW Guinan
CM Logan

Los Alamos Scientific Laboratory (3)
University of California
P.O. Box 1663
Los Alamos, NM 87544

DJ Dudziak
CR Emigh
W. Green

Massachusetts Institute of Technology
Cambridge, MA 02139

L. Lidsky, Nuclear Engineering Dept

McDonnell-Douglas Astronautics
P.O. Box 516
St. Louis, MO 63166

D. Kummer

Mound Laboratory
P.O. Box 32
Miamisburg, OH 45342

Manager, Tech Appl and Development

National Bureau of Standards
Gaithersburg, MD 20760

CD Bowman

Naval Research Laboratory (2)
Metallurgy Division, Code 6390
Washington, DC 20375

I. Manning
JA Sprague

DISTRIBUTION (Cont'd)

North Carolina State University
Department of Nuclear Engineering
Raleigh, NC 26707

JR Beeler, Jr.

Oak Ridge National Laboratory (7)
P.O. Box X
Oak Ridge, TN 37830

Director, Thermonuclear Oiv, (Bldg 9201-2)
RJ Colchin, Bldg 9201-2
FG Perey
M. Roberts, Bldg 9204-1
JO Stiegler
C. Weisbin
FW Wiffen

Pacific Northwest Laboratory (4)
P.O. Box 999
Richland. WA 99352

JL Brimhall
T. Chikalla
AB Johnson
LC Schmid

Princeton University (2)
Plasma Physics Laboratory
Forrestal Campus
P.O. Box 451
Princeton, NJ 08540

C. Osgood
K. Wakefield

Rockwell International Energy Systems
8900 DeSoto Avenue
Canoga Park, CA 91304

D. Kramer

Sandia Laboratories (2)
Albuquerque, NM 87115

FL Vook (2)

Sandia Laboratories
Livermore, CA 94550

WD Wilson

University of Michigan
Nuclear Engineering Department
Ann Arbor,-MI 48165

T. Kammash

University of Virginia
Charlottesville. VA 22901

WA Jesser

University of Wisconsin
1500 W. Johnson Drive
Madison, WI 53706

P. Wilkes

Westinghouse R&D Center (2)
Beulah Road
Pittsburgh, PA 15234

HR Holland
JA Spitznagel

HEDL (42)

HR Brager		W/A-57	FM Mann		W/A-5	RE Schenter	W/A-5
WL Bunch/			WN McElroy		W/C-39	FA Schmittroth	W/A-5
LL Carter		W/C-47	CL Normandin		W/C-115	WF Sheely	W/C-44
BA Chin		W/A-58	RE Nygren		W/A-58	RL Simons	W/A-57
DG Doran	(10)	W/A-57	EK Opperman		W/A-58	AL Trego	W/E-15
EA Evans		W/JAO-6	NF Panayotou		W/A-53	GL Wire	W/A-58
FA Garner		W/A-57	RE Peterson		W/E-18	HH Yoshikawa	W/A-62
DS Gelles		W/A-58	RW Powe11		W/A-57	Central Files	(5) W/C-110
R. Gold		W/C-39	RJ Puigh		W/A-58	Publ Services	(2) W/C-115
HL Heinisch		W/A-57					